UQAC
Université du Québec
à Chicoutimi

Evolution of microstructure and mechanical properties during elevated-temperature thermal exposure with Si and transition elements additions in Al-Cu 224 alloys

PAR

ZIMENG WANG

Sous la direction de M. X-Grant Chen (directeur) et M. Kun Liu (codirecteur)

Mémoire présenté à l'Université du Québec à Chicoutimi en vue de l'obtention du grade de Maîtrees science appliquées (M. Sc. A.) en ingénierie

Jury:

X.-Grant Chen	Director of research	UQAC	President of Jury
Kun Liu	Codirector of research	UQAC	Internal member
Zhan Zhang	Research Professor	UQAC	Internal member
Emad Elgallad	Research Professor	UQAC	Internal member

QUÉBEC, CANADA

RÉSUMÉ

Les propriétés mécaniques à haute température et la stabilité thermique des alliages d'aluminium oulés deviennent de plus en plus importantes afin de satisfaire la demande croissante d'alliages d'aluminium dans l'industrie automobile et pour développer les matériaux pour moteurs de nouvelle génération. Les alliages Al-Cu sont largement utilisés dans les applications moteurs, en particulier dans les blocs moteurs et les culasses. Dans le présent travail, diverses teneurs en Si sont ajoutées dans des alliages de type Al-Cu 224 pour étudier l'effet du Si sur l'évolution des précipités et des propriétés mécaniques lors d'une exposition thermique à long terme. De plus, des éléments de transition (Zr, V et Mn) et un nouveau traitement thermique en 2 étapes est utilisé pour tester la possibilité d'améliorer encore les propriétés mécaniques des alliages Al-Cu 224 à haute teneur en Si.

La première partie se concentre sur l'effet du Si sur l'évolution des précipités et des propriétés mécaniques lors d'une exposition thermique de longue durée jusqu'à 1000 h à 300 °C dans les alliages Al-Cu 224. Les résultats montrent que l’ajout de Si favorise la précipitation des précipités θ’ au cours du vieillissement et augmente alors les propriétés mécaniques à la condition T7. La limite d'élasticité en compression à température ambiante augmente de 316 MPa dans l’alliage 0.1Si à 355 MPa dans l’alliage 0.8Si, tandis qu'elle augmente de 120 MPa à 139 MPa à 300 °C. Cependant, lors d'une exposition thermique à 300 °C (conditions T7A), les propriétés mécaniques diminuent avec l'augmentation du temps d'exposition en raison du grossissement des précipités, et diminuent significativement avec l'augmentation de la teneur en Si. La limite d'élasticité à température ambiante de l'alliage 0.8Si chute de 355 MPa à 108 MPa seulement après 100 h d'exposition thermique, alors qu'elle atteint 130 MPa dans l'alliage 0.1Si après 1000 h d'exposition thermique. La résistance au fluage diminue également considérablement avec l'augmentation du Si. Outre la déformation totale élevée, le taux de fluage constant de l'alliage 0,8Si est également supérieur d'un ou deux ordres de grandeur à celui de l'alliage 0.1Si. Une hypothèse est proposée pour expliquer le comportement grossissant des précipités θ’ avec des ajouts de Si, selon laquelle la ségrégation du Si à l'interface matrice α-Al/précipités θ’ pourrait accélérer le grossissement des précipités θ’. Le court espacement entre les précipités et le rapport surface/volume élevé dans les alliages à haute teneur en Si à l'état T7 jouent également un rôle important car ils raccourcissent la distance de diffusion.

Dans la deuxième partie, des éléments de transition Zr, V et Mn sont ajoutés en alliage 0,5Si. Pendant ce temps, un nouveau traitement thermique en 2 étapes est appliqué pour former des dispersoïdes α et des dispersoïdes Al_3M. Le résultat montre que le micro-alliage augmente les propriétés mécaniques dans les conditions T7A et que le traitement des trayons en 2 étapes peut encore améliorer la stabilité thermique de l'alliage avec des éléments de transition. A l’état T7, aucune amélioration évidente des propriétés mécaniques n’est observée. La séquence d'amélioration des propriétés mécaniques à haute température peut s'écrire comme suit : l'alliage avec élément de transition + traitement thermique en 2 étapes > l'alliage avec éléments de transition + traitement thermique conventionnel > l'alliage de base + traitement thermique en 2 étapes > le alliage de base + traitement thermique conventionnel. Le rôle des éléments de transition et du traitement thermique sur l’amélioration des propriétés mécaniques est expliqué par le ralentissement du grossissement des précipités θ’, et la formation de dispersoïdes apporte une contribution supplémentaire aux propriétés mécaniques à température élevée.

ABSTRACT

The high-temperature mechanical properties and thermal stability of cast aluminum alloys become more and more important nowadays to satisfy the increasing demand of aluminum alloys in automobile industry and to develop the next generation engine materials. Al-Cu alloys are widely used in engine application especially in engine blocks and cylinder heads. In the present work, various contents of Si are added in Al-Cu 224 type alloys to investigate the effect of Si on the evolution of precipitates and mechanical properties during long-term thermal exposure. In addition, transition elements (Zr, V and Mn) and a new 2-step heat-treatment are introduced to test the possibility of further improving the mechanical properties of high-Si Al-Cu 224 alloys.

The first part focuses on the effect of Si on the evolution of precipitates and mechanical properties during long-term thermal exposure up to 1000h at 300 °C in Al-Cu 224 alloys. The results show that the addition of Si promotes the precipitation of θ' precipitates during aging and then increases the mechanical properties at T7 condition. The compressive yield strength at room temperature increases from 316 MPa in 0.1Si alloy to 355 MPa in 0.8Si alloy, while it increases from 120MPa to 139 MPa at 300 °C. However, during thermal exposure at 300 °C (T7A conditions), the mechanical properties are decreasing with increasing exposure time due to the coarsening of precipitates, and significantly declining with increasing Si contents. The yield strength at room temperature of 0.8Si alloy drops from 355 MPa to 108 MPa only after 100 h of thermal exposure, while it is as high as 130 MPa in 0.1Si alloy after 1000 h of thermal exposure. The creep resistance also dramatically decreases with increasing Si. Besides the high total strain, the steady creep rate of 0.8Si alloy is also one or two orders of magnitude higher than 0.1Si alloy. A hypothesis is proposed to explain the coarsening behavior of θ' precipitates with Si additions that Si segregation at α-Al matrix/θ' precipitates interface could accelerate the coarsening of θ' precipitates. The short inter-precipitates spacing and high surface to volume ratio in high Si alloys at T7 condition also plays an important role as they shorten the diffusion distance.

In the second part, transition elements Zr, V and Mn are added in 0.5Si alloy. Meanwhile, a new 2-step heat-treatment is applied to form α-dispersoids and Al_3M dispersoids. The results show that the micro-alloying increases the mechanical properties at T7A conditions, and the 2-step teat-treatment can further improve the thermal stability of the alloy with transition elements. At T7 state, no obvious improvement of mechanical properties is observed. The sequence of high-temperature mechanical properties enhancement can be written as: the alloy with transition element + 2-step heat-treatment > the alloy with transition elements + conventional heat-treatment > the base alloy +2-step heat-treatment > the base alloy +conventional heat-treatment. The role of transition elements and heat treatment on the improvement of mechanical properties is explained as slowing the coarsening of θ' precipitates, and the formation of dispersoids provides the supplementary contribution to the elevated-temperature mechanical properties.

TABLE OF CONTENTS

LIST OF TABLES

LIST OF FIGURES

ACKNOWLEDGEMENTS

Here I would like to thank the leader in our research group Prof. X.-Grant Chen for offering me this opportunity to do my master's degree at UQAC. Particularly his great patience and understanding. The past two years were really hard for me due to my mental health issues, I could not finish this program without his support. I am also very grateful to my co-director Prof. Kun Liu who gave priceless academic guidance and always there if I needed help. I also want to thank Prof. Zhan Zhang and my colleague Zhixing Chen who helped me a lot with TEM operations, and our lab technicians Samuel Dessureault and Félix Tremblay for their support and everyone helped me in the past few years, the list is long I feel like I could never finish it.

The project is sponsored by Natural Science and Engineering Research Council of Canada (NSERC) and Rio Tinto Aluminum, I really appreciate their generosity for funding us students in scientific research.

At the end, I want to thank my parents for their support although I did not get the chance to meet them often because of the pandemic, they are always the most kind, loving people I have ever met.

CHAPTER 1 INTRODUCTION

1.1 Background

Aluminum cast alloys are widely used in automotive industry nowadays due to the high demand of light weight vehicles, which not only provide better performance but also have higher fuel efficiency and lower greenhouse gas emissions. And the need is continuously rising. Al-Cu cast alloys play an important role in aluminum cast alloys. Many different alloys are designed and applied in various fields based on the Al-Cu system. This type of aluminum cast alloys is one of the promising aluminum alloys that is widely used in automotive industry.

Nowadays, the most widely used Al-Cu cast alloys usually contain up to 5 wt% Cu and they are able to provide a high strength at room temperature. However, the development of automotive industry also requires materials that can operate at elevated temperature to pursue better engine performance, the expected operating temperature of engines is usually over 300 °C[1, 2]. Therefore, improving the elevated temperature properties of key engine parts is one of significant concerns in industrial applications for Al-Cu cast alloys.

Elements like Mg and Si are often used to increase the mechanical properties at room temperature in Al-Cu system. It is reported that in Al-Cu 224 alloys, the addition of Mg can produce fine, dense and uniformly distributed θ' precipitates[3]. And limited addition of Si in Al-Cu alloys also has a significant effect on the precipitation of θ' in the aging stages. A small portion of Si promotes the formation of dislocation helices[4, 5]. Researchers found that GP zone or θ' precipitates are likely to nucleate at the sites where edge-type dislocations exist[6]. and if a GP II zone is Si-rich, it will be more likely to nucleate a θ' precipitates[7]. Besides, Si is also linked to other effects including decreasing the interfacial energy of α-Al/θ'[7] and increasing the mobility of Cu[8]. However, current researches mostly focus on the effect of Si on the room-temperature mechanical properties, there is limited systematic study on the influence of Si on the evolution of microstructure and mechanical properties at elevated-temperature, especially during the elevated-temperature thermal exposure.

Transition elements are also reported to introduce to Al-Cu system to improve their elevated-temperature properties. It is generally achieved in two approaches: one is to stabilize the θ' precipitates which is the dominant strengthening phase in Al-Cu alloys, while the other is the formation of thermally stable dispersoids with the addition of transition elements like Zr and Sc, which could provide supplementary contribution to the elevated-temperature mechanical properties. It is reported that the addition of transition elements with low diffusion rate like V, Zr, Sc, Mn, etc. can segregate at the θ' precipitates/matrix interfaces, which can suppress the coarsening behavior of the θ' precipitates and stabilize it at high temperature [1, 9-11]. The combination of V and Zr is reported more efficient in delaying the transformation from θ" to θ' precipitates and improving the coarsening resistance of θ' than only adding Zr[12]. For Sc, the addition of it will form the W-AlScCu phase that consumes Cu solutes, resulting in strengthen deterioration, but with the addition of Zr, it can also lead to a large number of $Al_3(Sc,Zr)$ precipitates which have an excellent effect on stabilizing θ' precipitates, then increasing the creep resistance at elevated temperature[12, 13]. Beside inhibiting the coarsening process, the nano sized $L1_2$ structured precipitates like Al_3Zr and Al_3Sc are also thermal stable at elevated temperature[14]. In Al-Cu alloys, the addition of Zr or Sc can lead to a co-existence of this metastable and coherent $Al_3(Sc,Zr)$ precipitates and θ' precipitates in the matrix that furtherly increases the thermal stability[12, 15]. And with the addition of Si, for example in 3xx series, larger size equilibrium $D0_{23}$ structured $(Al,Si)_3Zr$ dispersoids, instead of $L1_2$-Al_3Zr, are found in Zr added 3xx alloys[16, 17]. It is also reported that with limited addition of Si, Mn is also very effective stabilizer for θ' precipitates in Al-Cu alloys[18, 19]. However, limited study has been performed systematically on influence of combined additions of transition elements in Al-Cu 224 alloys on the elevated-temperature properties during the thermal exposure at 300 °C.

1.2 Objective

1) To systematically investigate the effect of Si on the evolution of precipitates and mechanical properties, especially during elevated-temperature thermal exposure in Al-Cu 224 alloys.

2) To explore the possibility of improving the thermal stability of high-Si Al-Cu 224 alloy by micro-alloying of transition elements and applying modified heat-treatments.

3) To provide a strengthening mechanism for Al-Cu cast alloys and a precipitates evolution model during thermal exposure.

CHAPTER 2 LITERATURE REVIEW

2.1 Development of Al-Cu alloys

Cu is the first major alloying element that is systematically and widely used for aluminum cast alloys. The Al-Cu alloys are heat-treatable since they respond well to precipitates hardening, which gives them high strength among all casting alloys. But it is important to restrict the Si content. Also, this group of alloys presents problems during casting like hot-tearing, therefore, to ensure the quality final product, it is also vital to provide generous feeding during solidification[20].

The Al-Cu alloys were first developed driven by the demand of the aircraft industry. The first one known as duralumin was designed by a German metallurgist called Alfred Wilm, which contains 3.5 wt% Cu 0.5 wt% Mn and 0.5 wt% Mg. It was first used in rigid airship frames. And when the monocoque construction methods are introduced the material in early 1930s, it was widely used in the aircraft industry. As pioneers as the duralumin, many Al-Cu alloys were developed and became today's 2000 series wrought alloys[21].

The 2xxx series alloys are primarily used where high damage tolerance and fracture toughness are the first concern like the fuselage. For example, the wrought alloy 2024 (which contains 4.3 wt% Cu, 1.5 wt% Mg and 0.6 wt% Mn) has been widely used in aircraft fuselage manufacture of most commercial passenger aircraft since the middle of the 1930s. It has a 20% higher yield strength than duralumin. After being T3 tempered, it also shows a high tensile yield strength ratio that promotes damage tolerance, which is ideal for manufacturing the armor[22].

The Al-Cu alloys are also well known for their superior creep resistance at elevated temperatures: alloys 2618 is used for the skin of high-speed Concorde aircrafts, and alloy 2219 is used for fuel tanks in space vehicles. With the addition of various elements and the control of impurities like iron and Si, their properties can be further improved[23].

When considering performance and cost, to reduce the material density is about 3-5 times more effective than to increase the mechanical properties[24]. Lithium is one of the most effective alloying elements in reducing density in 2000 series alloys that have a high solubility in aluminum matrix. For 1% addition of lithium, the density of aluminum can drop by 3%. Nowadays, lithium-containing aluminum alloys are widely used in fuel tanks and fuselage application in aerospace. Alloys 2195(Al-Cu-Li alloy) was also once used in the external launch tank of US Space Shuttle[23].

As mentioned, the most widely used aluminum casting alloys in automotive engine manufacturing are Al-Si-Mg and Al-Si-Cu-Mg cast alloys, which have been developed decades ago. The high proportion of Si in the alloys provide superior hot-tearing resistance and fluidity, making mold feeding much easier in the casting process. As the development in automotive power system, better engine material with high strength at elevated temperature are desired. Although 356 type and 319 type have a relatively high ambient-temperature mechanical properties and by introducing transition elements to form thermal stable dispersoids can further increase their elevated-temperature mechanical properties. The alloys with high Si contents can still not be competitive in the revolution of the engine material.

Given the facts of Al-Cu and Al-Si alloys, it seems always hard to get the perfect combination of castability and mechanical properties at the same time. But when the strength is the first priority, Al-Cu alloys are always the better options. People are also trying to find a way to improve the castability and further enhance the mechanical properties as well.

As a typical Al-Cu cast alloy, B206 alloy has been applied for cylinder head and engine blocks. However, a recent study on a newly designed Al-Cu 224 alloy has aroused public's attention. It demonstrates the proper addition of Mg can improve the yield strength to 142 MPa at 300°C, which is only 93MPa for B206 alloy[3, 25]. Table 2.1 is a summary of the high temperature properties of different Al-Si or Al-Cu cast alloys. The result clearly shows that Al-Cu cast alloys are more promising with higher yield strength.

Table 2.1 Comparison of the YS at elevated temperature of various cast aluminum alloys. (Summarized based on literatures[3, 12, 25]@ZIMENG WANG)

Alloys	YS (MPa) at 300°C-315°C* with stabilizations		
	100 h	200h	1000 h
224-(0Mg)-T7	110		--
224-(0.13Mg)-T7	142		125
Al5CuMg-T6 (206)		60	--
Al5CuNiMnZr-T6		105	--
206L T6	93		77
240-T7	105*		90*
224ZrSc-T7	125		
224ZrV-T7	114		
356-T6	28*		24*
356ZrV-T6	41		--
3560.5Cu-T7	33		--

3560.5Cu0.3Mo-T7	47		--
319-T7	51		34
3190.25Mn0.3Mo-T7	60		54

Recent studies[1, 26] have confirmed a strong relationship between the segregation of solute atoms to θ’-Al_2Cu/α-Al interface and the stability of metastable θ’ precipitates. This opens numerous opportunities for precipitates strengthening alloys (like Al-Cu alloys) designation, which can further push the limits of elevated-temperature properties of the alloys and extend their thermal stability range through matrix/precipitates engineering. In this investigation in high-performance computing and data informatics, a database of the segregation energies of 34 micro-alloying elements to the θ’-Al_2Cu/α-Al interface is calculated by a first-principles approach based on density function theory (DFT) and it is demonstrated in Figure 2.1.

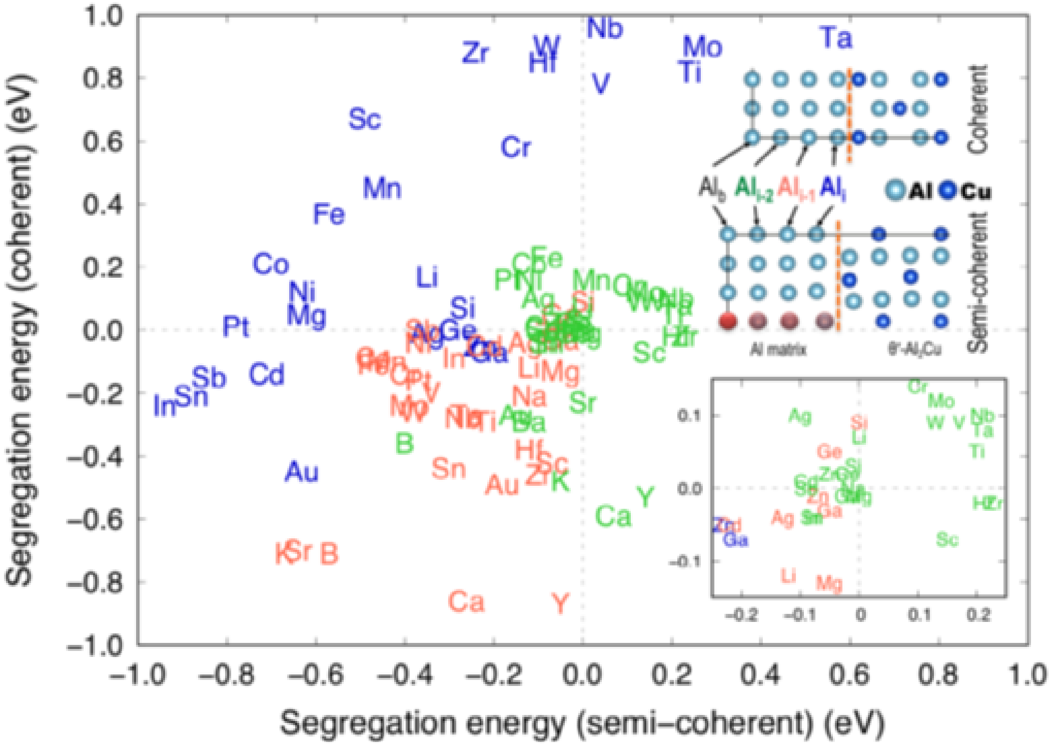

Figure 2.1 DFT segregation energies of 34 solutes at each platelet (Al*i*–2, Al*i*–1 and Al*i*) at the coherent and semi-coherent interfaces between the Al matrix and θ’. Only the lowest segregation energies at given platelets are shown[1].(@ELSEVIER)

In Figure 2.1, 34 solute elements are categorized into four quadrants by their segregation energies at the coherent and semi-coherent interface. It is suggested that elements like Mn, Zr Sc that segregate to and have positive energies of the semi-coherent interface might have greater efficiency on stabilizing the precipitates at elevated temperature. The prediction is corresponding to the literatures which experimentally provide the evidence[19, 27]. Another groups of elements like Cd, Sn and In are reposted to have a strong affinity to vacancies in Al[28]. They favorably segregate at both coherent and semi-coherent interfaces, but their mixing energies indicate a low solubility of them within sublattices. Therefore, these elements might only act as a chemical bonding barrier to suppress the coarsening of θ’ according to the literatures and might not be able to stabilize the θ’ by partitioning to the θ’. But the effect might be confined to low temperature due to their high diffusivity in Al[28-31]. Despite of the different mechanisms, these discoveries provide solid background knowledges to support the development of precipitates hardening alloys and help to elevate the high-temperature properties of these alloys.

2.2 Precipitates of Al-Cu casting alloys

The Al-Cu binary system has been well investigated in the past, which help researcher better understand the binary system for industrial metal alloys and the age hardening strength method[32]. The classis precipitation sequence of Al-Cu alloys is used in many textbooks as an example to demonstrate the process of precipitation, which shows the academic importance of it. The Al-rich corner of the Al-Cu phase diagram shown in Figure 2.2 indicates all the possible phases that can be observed in the decomposition sequence[31].

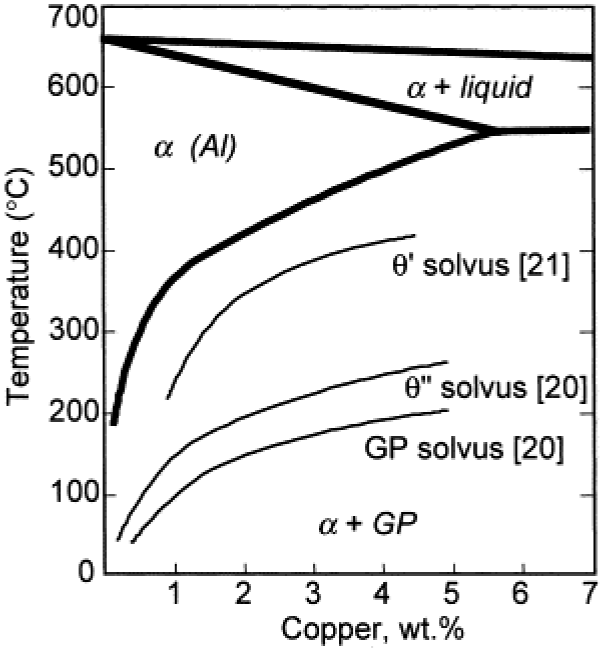

Figure 2.2 Al-rich corner of the Al–Cu phase diagram showing the metastable solvus boundaries for GP zones, θ” and θ’, together with the equilibrium solvus line for the θ phase[31]. (@ELSEVIER)

It has been proposed in many studies that the decomposition sequence of precipitates in Al-Cu binary system follows the process below[33, 34]:

Supersaturated Solid Solution (SSSS) → Guinier-Preston zones (GP zones)

→ θ” (GP II zones) → θ’ → θ

Figure 2.3 shows the Gibbs free energy of different phases-composition of Cu curves of Al-Cu alloys at low temperature, GP zone and the αmatrix have the same crystal structure therefore it shares the same curve with the αmatrix. θ” phase and θ’ phase are less stable than the equilibrium θ phase with higher Gibbs free energy. The driving force of phase transformation is the decrease of Gibbs free energy, although the driving force to precipitates of θ phase is the highest, there is a lower nucleation barrier for θ” phase and θ’ phase. Thus, they will precipitate before equilibrium θ phase.

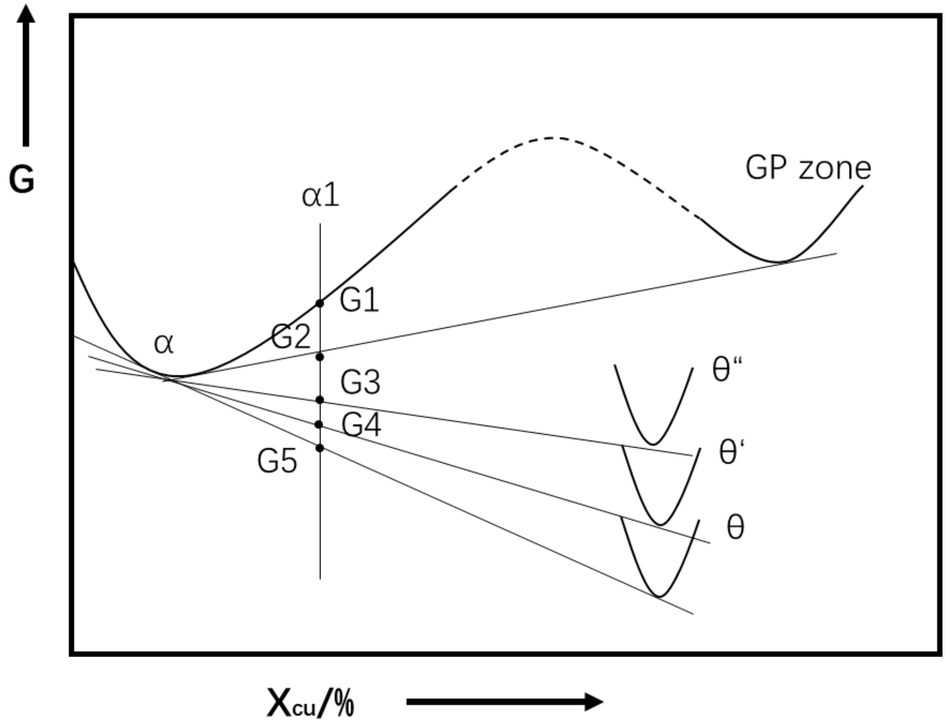

Figure 2.3 Schematic of Gibbs free energy of different phases-composition of Cu curves of Al-Cu alloys at low temperature. (@ZIMENG WANG)

The complete decomposition sequence does not occur in every circumstance, only when the aging temperature is below the GP zone solvus and with a high enough supersaturation. First the solute Cu atoms are enriched in the Al matrix when the alloy is aged below the GP zone solvus to form the Cu atom layers on {001} α planes, which are known as GP zone. The general agreement is that GP zones are usually single-atom layers of Cu on {001} α planes but multilayer GP zones have also been observed[35]. The typical size of GP zones is in the order of tens of nanometers, and there is critical diameter of GP zones between 5nm to 10 nm, after reaching which the zone size will remain constant. This stage before further transformation is called incubation period[31]. As aging proceeds, θ” phase will precipitate. It is directly transformed from solute clusters or GP zones in underaged conditions. θ” phase contain 10-40 at% Cu, therefore, different combination of Cu and Al layers can form it. The most accepted structure of θ” phase is that it has 2 layers of Cu atoms separated by 3 layers of Al atoms along {001} α planes. θ” phase exhibits plate-like shape and has coherent faces but when the plates’ thickness is too high the edge of θ” phase can become semi-coherent[36-38]. Figure 2.4 demonstrates a structure of GP zones and θ” phase (also recognized as GP2 zones). The formation of θ” phase also follows by an incubation period and then the formation of metastable θ’ phase occurs. The crystal structure of θ’ phase is body-centered tetragonal (I4/mcm, a = 0.404 nm and c = 0.580 nm). It has the nominal stoichiometry of Al_2Cu and forms as rectangular or octagonal plates on {100}Al planes and also has a particular orientation relationship with the Al matrix ($\{100\}_{Al}||\{100\}_{\theta'}$, $<001>_{Al}||<001>_{\theta'}$) Finely dispersed θ’ phase is consider as extremely shear resistant precipitate which has coherent broad faces and semi-coherent interfaces at the edges[39]. θ’ phase can directly forms heterogeneously on the defects like dislocations to reduce the misfit in two $<001>_{Al}$ directions. Recent research also finds that θ’ phase continuously nucleates on θ” phase through the rearrangement of elements. The evidence is shown in Figure 2.5. During the process, a part of θ” phase dissolve to provide extra Cu atoms since θ’ phase (Al_2Cu) contains more Cu atoms than θ” phase (Al_3Cu), and the transformation initiates randomly at several sites inside of the θ” phase[40].

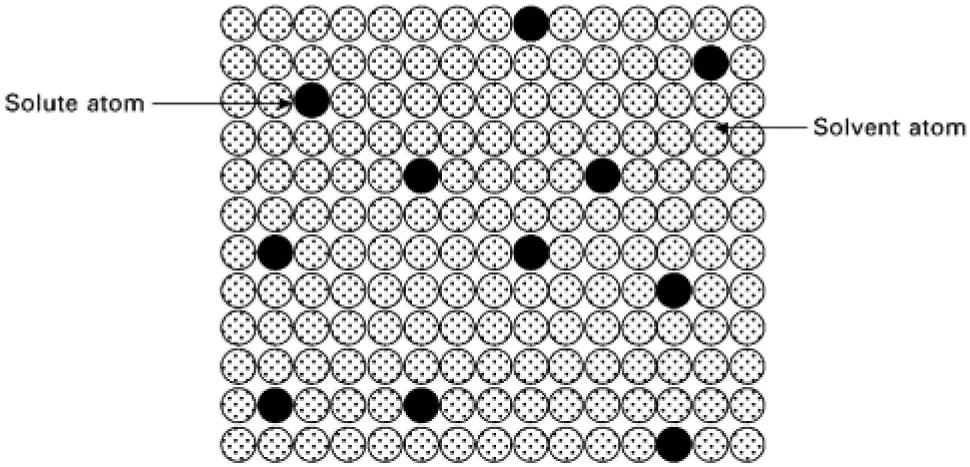

Supersaturated solid solution

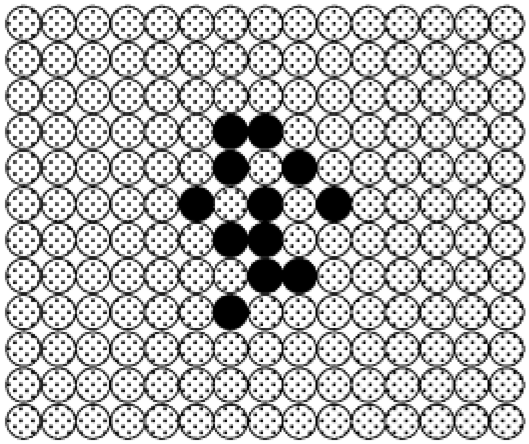

GP1 zone

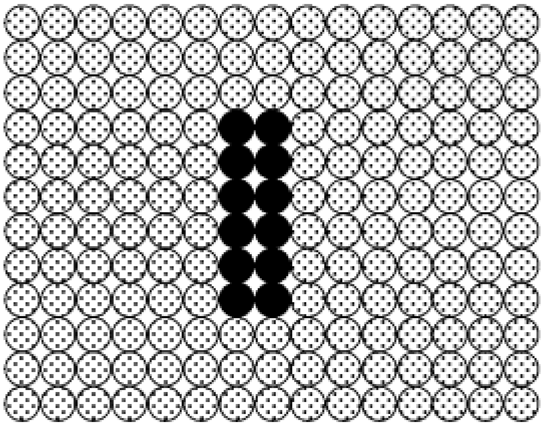

GP2 zone

Figure 2.4 Schematic showing the transformation from a supersaturated solid solution to GP1 zone to GP2 zone during ageing[41]. (@ELSEVIER)

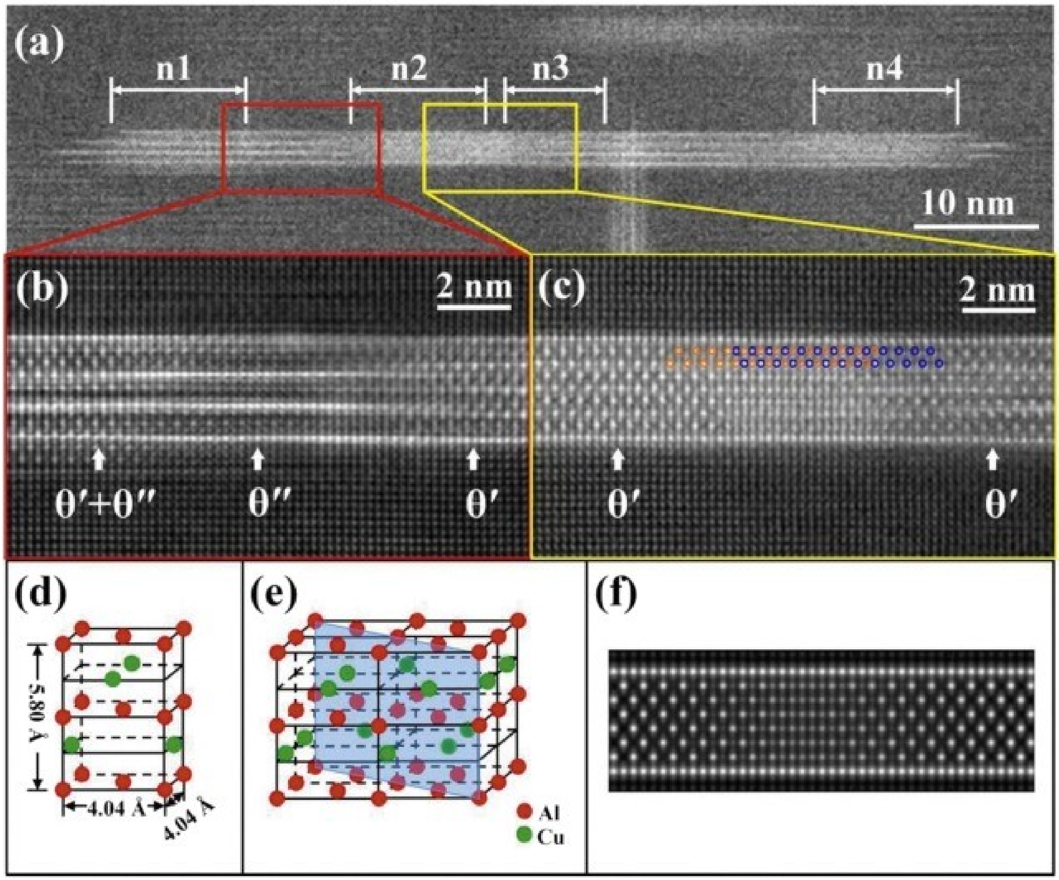

Figure 2.5 (a) HAADF image of θ” precipitate with the ongoing transformation to θ’. (b and c) Enlarged HAADF images (filtered) of the regions between n1 and n2 (in the red frame), and between n2 and n3 (in the yellow frame) respectively, schematic diagram of extending the sections n2 and n3 is overlaid on (c), orange circles represent Cu atoms in the n2 section and blue the n3 section, Al atoms are omitted. (d) Unit cell of θ’. (e and f) The atomic arrangements and simulated HAADF image for APDB of the type a/2<110> lying on {110}θ’ in θ’[40]. (@ELSEVIER)

The prolonged aging or over aging (giving adequate time or temperature) can lead to the formation of θ phase (shown in Figure 2.6), which is incoherent and thermodynamically stable with a body centered tetragonal structure (I4/mcm, a = 0.607 nm, c = 0.487 nm). It is proposed that θ’ phase first grows and coarsens and when aspect ratio reaches a critical value, the transformation to θ phase becomes thermodynamically favorable. And if a θ’ precipitate is below the “critical aspect ratio”, θ will nucleate on its semi-coherent interface, and the θ phase will be stabilized and grow at the cost of θ’. And value of the critical aspect ratio increases with temperature and the size of θ precipitates[42-44].

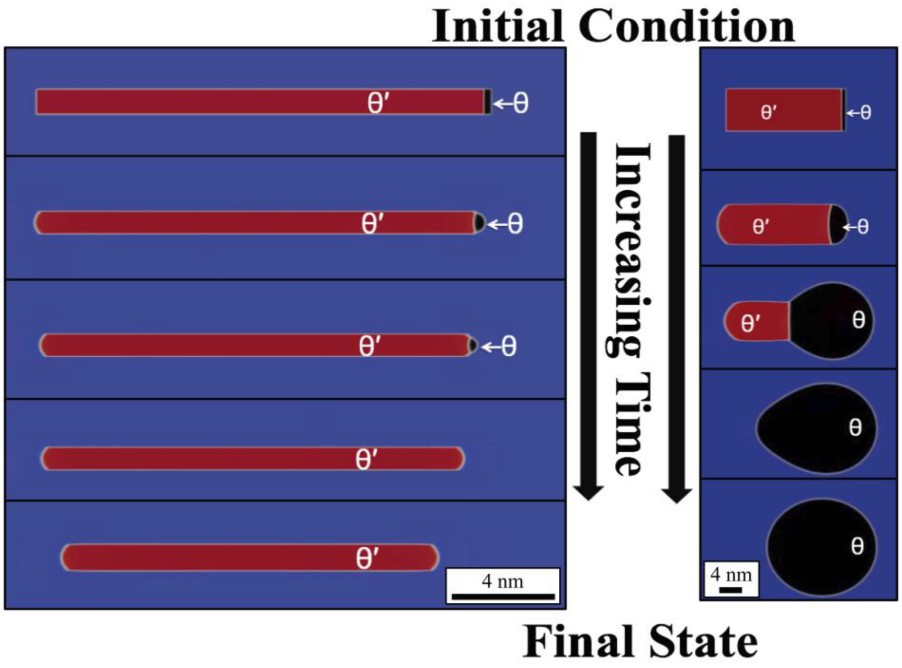

Figure 2.6 The competition between an existing θ′ particle and a θ nucleus placed on its semi-coherent interface, as predicted by phase field simulations for two sample conditions. Generally, higher aspect ratio θ′ particles are more stable against phase transformation into θ[44]. (@SSRN OPEN ACCESS)

2.3 Influence of alloying elements on the evolution of microstructure and mechanical properties

2.3.1 Si

Si, similar to Fe, is usually considered as an impurity in many Al-Cu alloys. However, it still plays an important role in this type of aging hardening alloys. Its effect can be classified into two aspects: it can modify the as-cast microstructure and affect precipitates evolution in Al-Cu alloys[45].

The Fe-intermetallics in Al-Cu alloys are well studied in many researches[46-49]. Fe in 206 alloys, usually precipitates two types of intermetallics: platelet β-Fe ($Al_7Cu_2(MnFe)$) and Chinese scripted α-Fe ($Al_{15}(FeMn)_3(CuSi)_2$) with Fe level no more than 0.3 wt%. When the Si/Fe ratio is around 1, β-Fe is the only Fe-intermetallics in the microstructure[50]. B-Fe is reported that could dramatically deteriorate the tensile properties of the alloys because it is brittle and could lead to crack initiation, propagation and make the alloys more susceptible to hot tearing[51]. Liu et al[46, 47] propose that the individual addition of Si or the combination of Si and Mn can modify the intermetallics by promoting the formation of α-Fe and suppressing the precipitation of β-Fe. Since the formation temperature of α-Fe is higher than β-Fe during the solidification process, after the formation of α-Fe, there are fewer Fe atoms available for the formation of β-Fe. Figure 2.7 shows the existing intermetallics after different addition of Si and Mn.

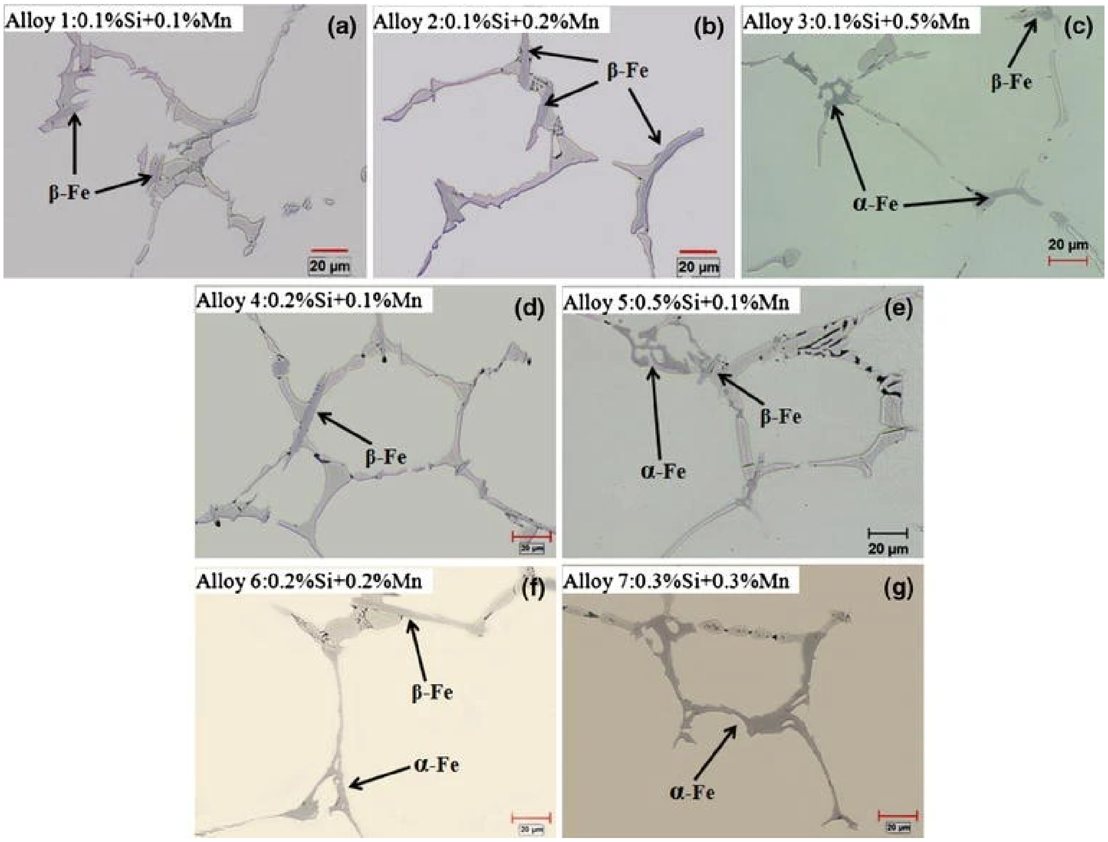

Figure 2.7 Microstructures of the experimental alloys with individual or combined additions of Mn and/or Si[46]. (@SPRINGER)

Si has been experimentally proven that has a positive effect on the precipitates' evolution in Al-Cu during the aging stage. In Al-2Cu-1Si ternary alloy[52], θ' precipitates are smaller, more densely distributed with lower aspect ratio and coarsening resistant than in Al-2Cu binary alloy when the same aging treatment is conducted. The phenomenon is explained using Khachaturyan-Hairapetyan (KH) thermoelastic theory, indicating that the elastic interaction between Si and θ' precipitates catalyze the nucleation of θ' precipitates on Si and inhibit the coarsening of it.

By first-principles calculation, Biswa et al[7], find that Cu sites are attractive to Si segregation at α-Al/θ' interfaces and Si favorably partition to Cu sublattice sites in θ' precipitates, which is in agreement with experimental results shown in Figure 2.8. In their study, GPII zones, also known as the θ" precipitates, are observed in Si-containing alloy with a three times higher number density than in Si-free alloy. And according to the discoveries: 1) at high aging temperatures, θ' precipitates, with the help of dislocations, can heterogeneously nucleate on GPII zones preceded by the dissolution of GPII zones[53-55]. 2) the addition of Si favors the formation of dislocations helices[5, 56]. Si is believed to catalyze the heterogeneous precipitation of θ" and θ' precipitates.

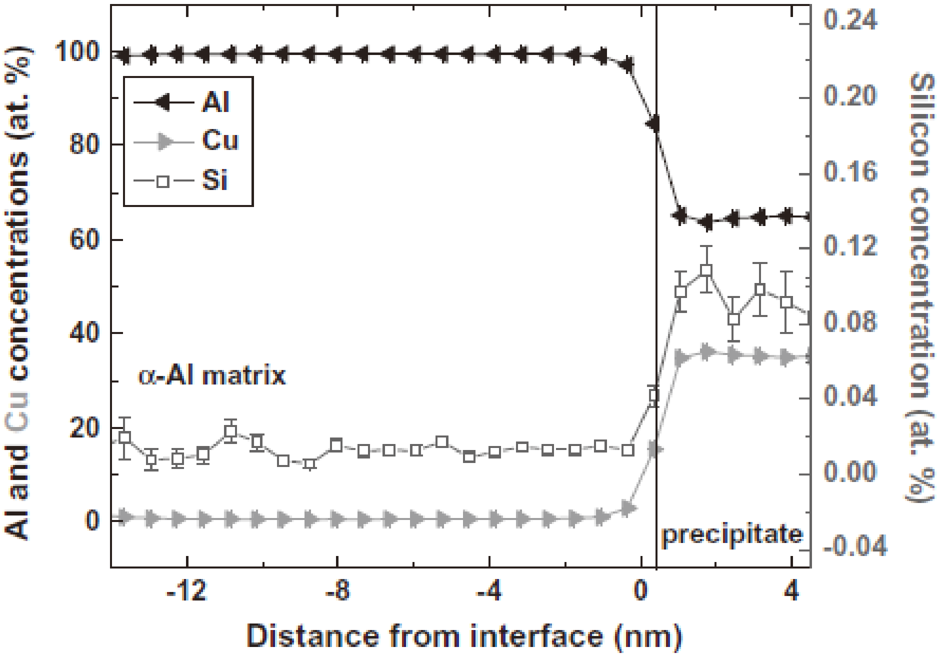

Figure 2.8 Proxigram from a sample of alloy (Al-4.0Cu-0.022Si-0.054Fe) aged at 463 K for 8 h, Green laser pulsing is used[7]. (@ELSEVIER)

Si's effect on the thermal stability of θ' precipitates during thermal exposure is vital to the Al-Cu alloys. A recent study[57] demonstrates that an intermediate addition of Si (0.05 wt%~0.10 wt%) maintains a good mechanical property of the AlCuMnZr alloys after 200 h thermal exposure at 300 °C. The thermal stability of θ’ precipitates can be linked to the as-aged microstructure. Figure 2.9 is the TEM images of three different alloys with different Si additions, which clearly indicates that Alloy D with intermediate Si has larger size θ’ precipitates and greater inter-precipitates space at as-aged conditions and a dense distribution of θ’ precipitates after thermal exposure. Figure 2.10 demonstrates the mechanism that the addition time provided by larger precipitates allows Mn and Zr to segregate at the interfaces of α-Al/θ’ precipitates to further stabilize the θ’ precipitates.

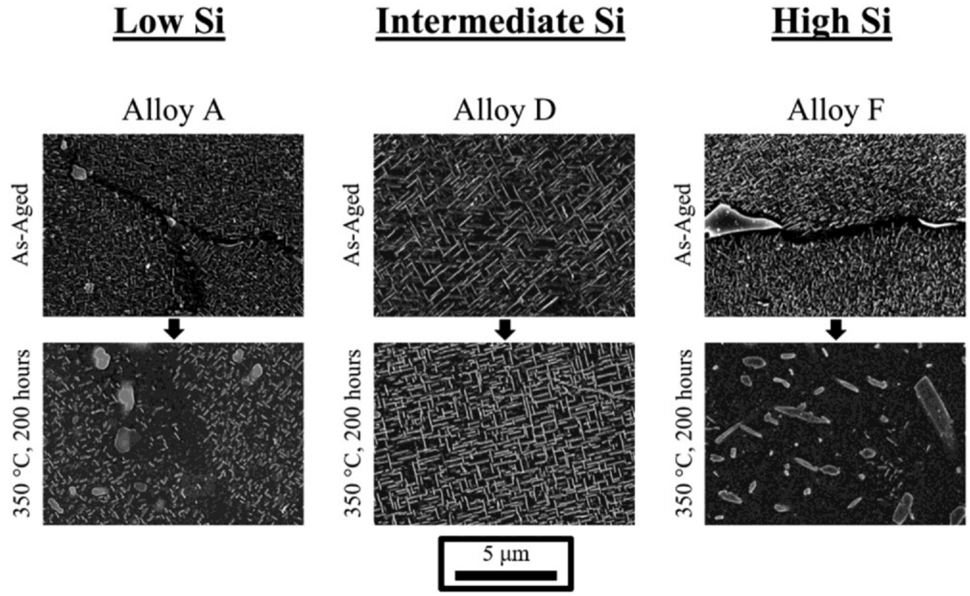

Figure 2.9 Representative microstructures of low, intermediate, and high Si alloys in this study after aging and after subsequent high temperature exposure at 350 °C for 200 h: The low Si alloy and the high Si alloy both exhibit fine θ’ precipitates in the as-aged state and θ’ to θ transformation upon extended thermal exposure. The intermediate Si alloy shows coarser θ’ particles upon aging and no obvious θ’ to θ transformation upon thermal exposure[57]. (@ELSEVIER)

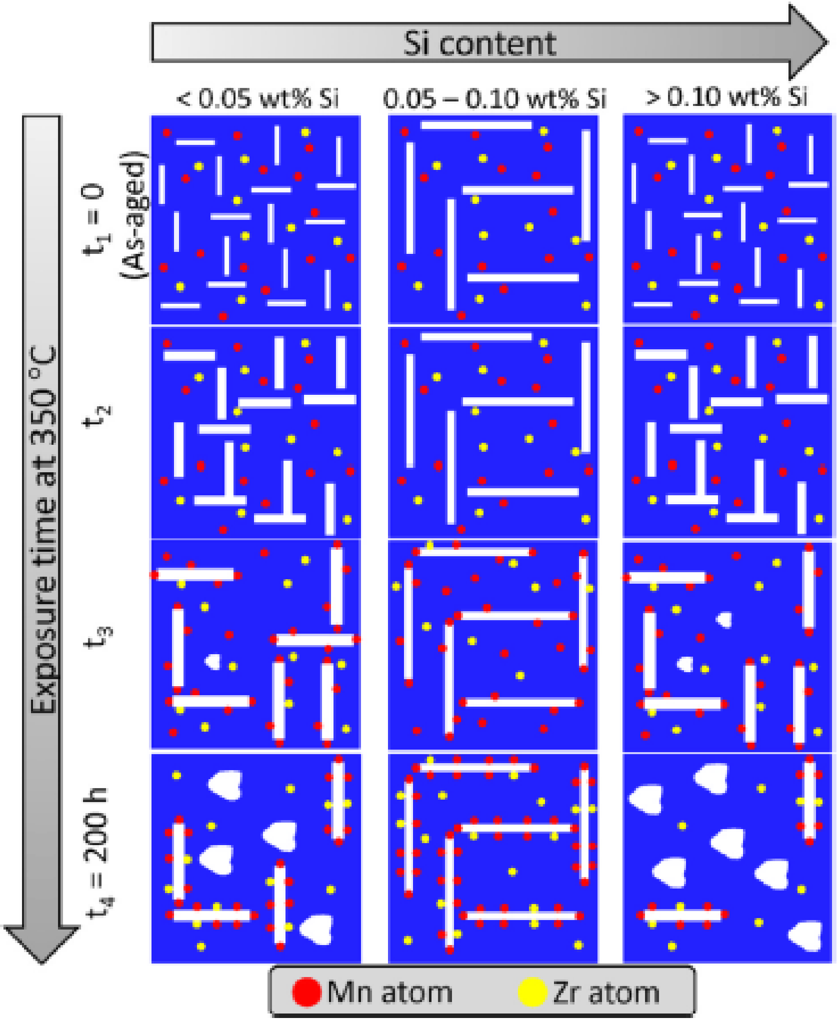

Figure 2.10 Proposed nucleation mechanisms which explain the reduced number density of precipitates observed in intermediate Si alloys relative to low and high Si alloys. Note that this figure is schematic, and the Si clusters are not drawn to scale with the vacancy structures[57]. (@ELSEVIER)

The effect of Si on precipitates evolution in Al-Cu alloys has been well investigated. But only focusing on the aging stage, studies on thermal stability during thermal exposure at elevated temperatures are carried out but the addition of Si is restrained at a low level. The mechanism of how high Si addition influences the thermal stability of the θ' precipitates and furtherly, of the Al-Cu alloys is still unknown. Thus, it is still necessary to fill this blank for the development of Al-Cu alloys in the future.

2.3.2 The role of transition elements in Al-Cu alloys

2.3.3 V

V belongs to the Group 5 elements. It has low solubility in aluminum matrix of 0.33 at% at 662.1 ℃. It is also reported as a much slower diffuser than Sc and the group 4 elements like Zr, Ti or Hf[58, 59]. The V containing aluminum alloys are usually used for structure components of automobiles due to their ability to absorb kinetic energy, this feature is primarily considered in components that might be strongly deformed in accidents[60].

The addition of V is also used in the purpose of improving elevated-temperature properties by forming the V-containing dispersoids[59, 61]. It is reported that 0.1 wt%~0.2 wt% addition of V in 7150 alloys (Al6.3Zn2.2Mg2.3Cu0.16Si) can enhance recrystallization resistance during post-deformation annealing, particularly in the presence of a great number of $Al_{21}V_2$ dispersoids that are distributed in supersaturated dendrite cells, which furtherly increases the high temperature strength. But due to the limited solubility of V, When exceeding 0.15 wt% addition, primary V-bearing intermetallic will form in as-cast condition and stay undissolved during following homogenization[62].

V is believed to be a grain refiner; it can also reduce the conductivity and increase the temperature. It is reported that the addition of 0.045% V in 5083 alloy restricts the growth of recrystallized grains and leads to a refined fibrous structure in the rolling sheet[63].

In 6063 alloy, the addition of 0.1 wt% V can accelerate the precipitation of β'and β'' phases, which have an impact on the yield strength and tensile strength after aging[64]. In a study of

6xxx series alloys with addition of Cu, V is found that can fluence on the changes in shape of the precipitates and 0.2 wt% addition of V can significantly increase the elongation rate of the alloys[65].

The reports focusing on the effect of V on the precipitation in Al-Cu alloys are still hard to find. It is reported in AA2091 alloys, the dense V-bearing dispersoids can lead to a finer distribution of S' precipitates as well as the a higher hardness level[66]. A recent study mentions that in 224 alloys, the combination of V and Zr improves the yield strength of experimental alloys superior to individually adding Zr or V by stabilizing the θ' phase. The mechanism of the effect of V has not reported but believed resemble as Zr[12, 67].

2.3.4 Mn

As mentioned, Fe is an inevitable impurity in aluminum alloys that promote the formation of various intermetallics. The eventual phases containing this element depends on the composition of alloys, cooling rate and heat-treatment methods. In Al-Cu alloys, the usual Fe-rich intermetallics includes $Al_3(FeMn)$, $Al_6(FeMn)$, $Al_m(FeMn)$, Al_7Cu_2Fe(β-Fe), $Al_{15}(FeMn)_3(SiCu)_2$ (α-Fe)[47, 68-74]. Among these intermetallics, β-Fe is the only one that does not contain Mn, which as well as $Al_3(FeMn)$ could severely deteriorate the tensile properties of Al-Cu alloys. And giving the brittle characteristic, they could lead to crack initiation and propagation, on the contrary the Chinse scripted α-Fe intermetallic is less harmful to the mechanical properties[75]. The introduction of Mn in Al-Cu alloys is to compensate the harmful effect of iron. It is reported that Mn can promote the transformation of α-Fe, and their transformation efficient depend on the Fe/Mn ratio. The Fe/Mn ratio as 1.6 for non-pressure applied casting and 1.2 for 75 MPa pressure applied casting, respectively, is reported in Al5Cu0.5Fe alloys that can fully convert the β-Fe to α-Fe intermetallic[76]. Figure 2.11 shows the transformation Fe-rich intermetallics with Mn/Fe ratio. And Figure 2.12 demonstrates the volume precent of α-Fe intermetallic with Mn addition and as well as cooling rate and Si addition, which indicates Mn and Si have a synergistic effect and are more efficient as combined[46].

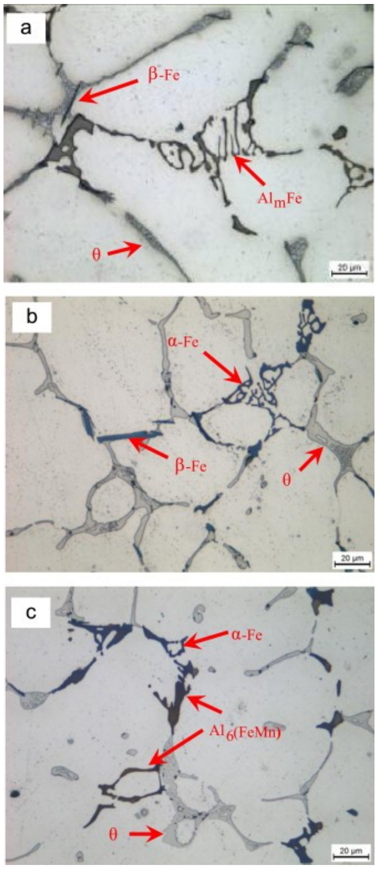

Figure 2.11 Fe-rich phases in as-cast condition without applied pressure: Mn/Fe=0; (b) Mn/Fe=1.2; (c) Mn/Fe=2[76]. (@ELSEVIER)

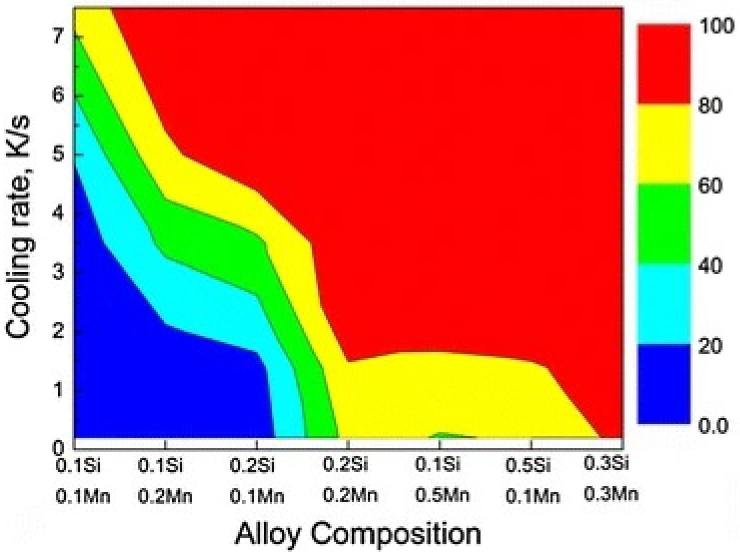

Figure 2.12 Relative volume percent of α-Fe at various cooling rates in the experimental 206 cast alloys[46]. (@SPRINGER)

Similar result is also found in 3xx alloys[77], a complete transformation from β-Fe to α-Fe can be expected with a critical Mn/Fe around 1.2, exceeding which, it might cause unwanted volume of α-Fe in the microstructure. Besides, in 3xxx alloys with small amount of Si, the micro-alloying of Mn can also promote the precipitation of α-Al(MnFe)Si dispersoids or Al_6(MnFe) dispersoids which can improve the mechanical properties in the condition of restricting the Mn addition lower than its solid solution limit[78, 79].

Mn is also reported as a stabilizer for θ' precipitates in Al-Cu alloys, which thereby, helps to improve the high temperature properties[10, 18, 19, 57]. It can segregate at both semi-coherent and coherent α-Al/ θ', but a thicker Mn-rich layer is observed at the semi-coherent interface and stabilize θ' precipitates at high temperatures via decreasing the interfacial energy and reducing the effective diffusion coefficient of solute. Moreover, the addition of Zr and Mn is able to stabilize the θ' precipitates at 350 °C, which is more effective than individually adding Mn where the θ' precipitates can only maintain stable at 250~300 °C[19].

2.3.5 Zr

Transition elements in group 4 and group 5 of the periodic table, like Zr, Ti, V Nb, Hf, Ta, as well as Sc, are favorably added in Aluminum alloys to form the L_{12} structured Al_3X precipitates for advanced high temperature application. Because the system of Al-X (X=Zr, Sc Ti…) has high melting temperature low density, low precipitate/matrix mismatch, and good thermal stability[80-82]. The metastable L_{12} Al_3Zr precipitates is reported that can main thermally stable at 425 °C even after 1600h with transforming to $D0_{23}$ structured equilibrium phase[83]. Figure 2.13 shows the L_{12} Al_3Zr precipitates after aged at 425 °C for 1600 h keep a radius of 10.9±1.9 nm.

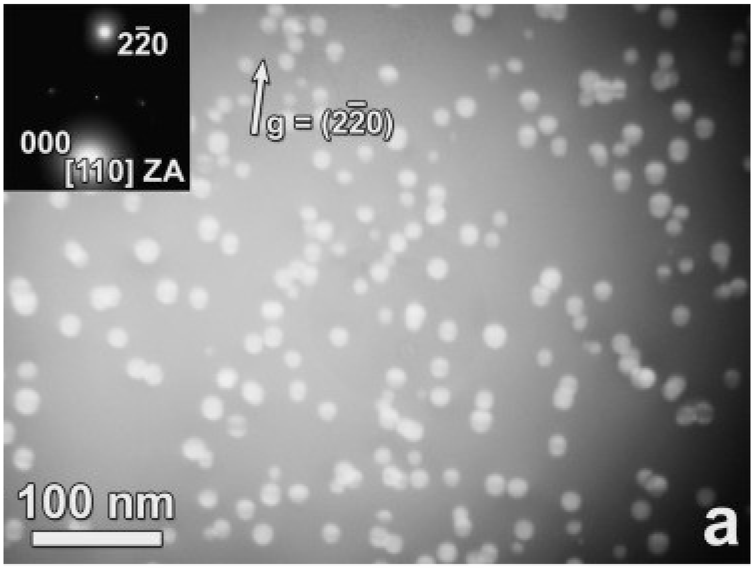

Figure 2.13 Centered superlattice dark-field TEM micrographs of dendritic precipitates in Al–0.1 Zr aged at 425 °C for 1600 h[83]. (@ELSEVIER)

In Al-Cu casting alloys, adding these transition elements like Zr can improve the thermal stability of the alloys by not only forming the coherent nano-sized precipitates but also modifying the α-Al matrix/precipitates interface, retarding the coarsening behavior of precipitates like θ’ and Q’[84-86].

It is reported that Al_3Zr particles facilitate heterogeneous nucleation of θ” and θ’ precipitates on them during aging[87]. Figure 2.14 shows the HRTEM images as evidence. The same phenomenon is also reported in other researches, and it occurs when the interfacial energy of Al_3Zr/ α-Al matrix is smaller than the interfacial energy of Al_3Zr/ θ’ while which is smaller than the α-Al matrix/θ’ interfacial energy[88, 89]. The precipitation of θ” on pre-existed Al_3Zr causes a compact morphological structure of these two phases which is also described as sandwich-like: broad faces of θ” enclosing Al_3Zr and surrounding it. The formation of such sandwich-like structure significantly reduces the coherency strain, thereby the elastic strain energy, leading to a delayed growth and transformation of θ”[90].

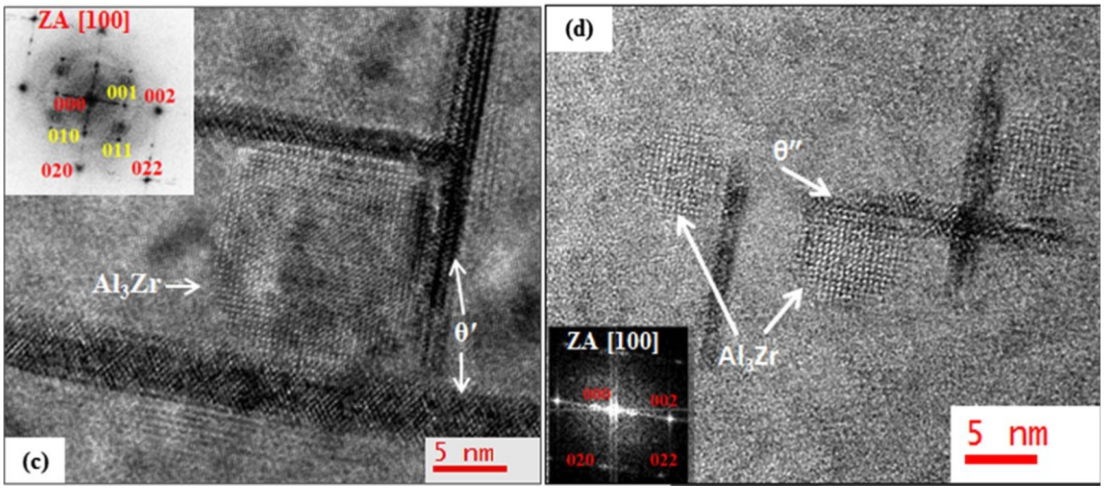

Figure 2.14 2219NbZr alloy after peak aging at 473 K (200 °C) (c) HRTEM image showing θ’ precipitate nucleating on Al_3Zr, and (d) HRTEM image showing θ” precipitates nucleating on Al_3Zr[87]. (@SPRINGER)

In terms of Al_3M precipitates, Sc is predicted that can eliminate the precipitates free zone(PFZ) even with a small amount of addition (<0.1wt%) in Al-Zr alloys[91]. In Al-Sc-Zr alloys, the analogous core-shall L_{12} precipitates can form spontaneously under proper processing with controlled chemical compositions, which usually have a Sc-rich core and 1-2nm thin Zr-rich shell[92-94], Figure 2.15 demonstrates the structure of $Al_3(Sc,Zr)$ precipitates observed by TEM. The mechanism is explained by Clouet et al[95], the introduction of Zr in Al-Sc leads to a large free-energy drop for the $Al_3(Sc,Zr)$ nucleation and the precipitates primarily absorb Sc atoms owing to the larger diffusion coefficient of Sc than Zr, which leaves the slow-diffusing Zr atoms to precipitate on the Sc-rich core as the growth continues. When Sc and Zr are introduced to Al-Cu alloys, a research reports that the combined addition of Sc and Zr shows a better creep resistance than only adding Zr in 224 alloys[12], while in Al-4Cu binary alloys, the addition of Zr and Sc significantly increases the UTS and YS during aging process[96].

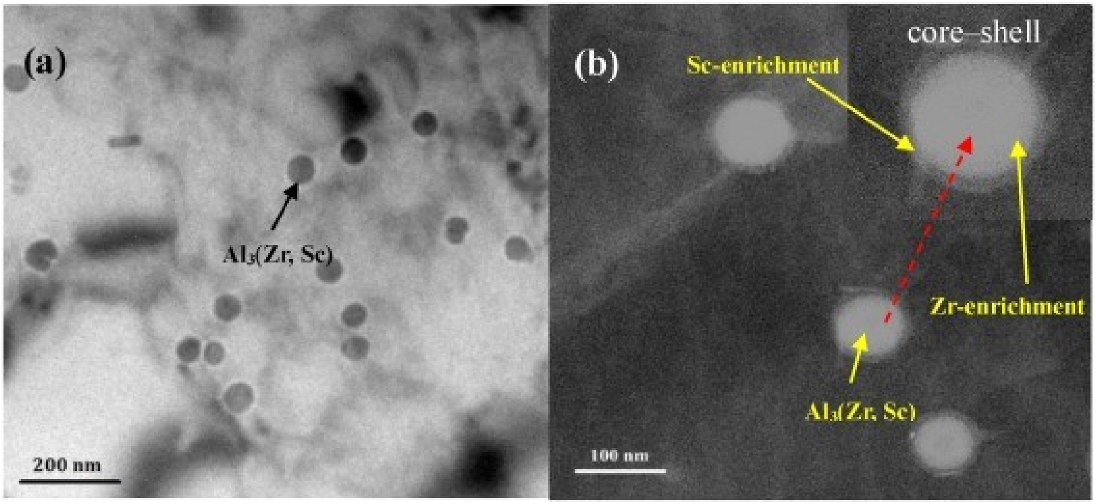

Figure 2.15 (a) Bright-field and (b) dark-field TEM micrographs of Al–Zr–Sc alloy cable specimens aged at 350 °C for 36 h[97]. (@ELSEVIER)

2.4 Nucleation, growth and coarsening of precipitates in Al-Cu alloys

The general sequence of form a two phases system form a single-phase system includes three distinct steps: 1) nucleation of the new phase; 2) growth of the nuclei particles accompanying depletion of the matrix of solute; 3) coarsening which is also called Ostwald ripening. Notably, these three steps are not separated but artificially defined for better understanding the process[98].

Classical nucleation theory (CNT) is the most commonly used theory to model nucleation. The central goal is to predict the nucleation rate. The nucleation favorably happens when the Gibbs free energy of the systems reduces. The Gibbs free energy is determined by three facts: 1) the chemical free energy, which is also the driving force for the phase transformation. 2) the interface energy and 3) the elastic strain energy. The last two show a tendency to increase the new phase's Gibbs free energy, thus, hinder the phase transformation[99]. Figure 2.11 shows a schematic of net free energy-radius of precipitated phase curve. The net free energy first increases the decrease with the radius of precipitated phased, leading to a peak at where r=r*, where r* is the critical nucleation size. Only when the radius is greater than it, the nucleus will grow, otherwise it will dissolve.

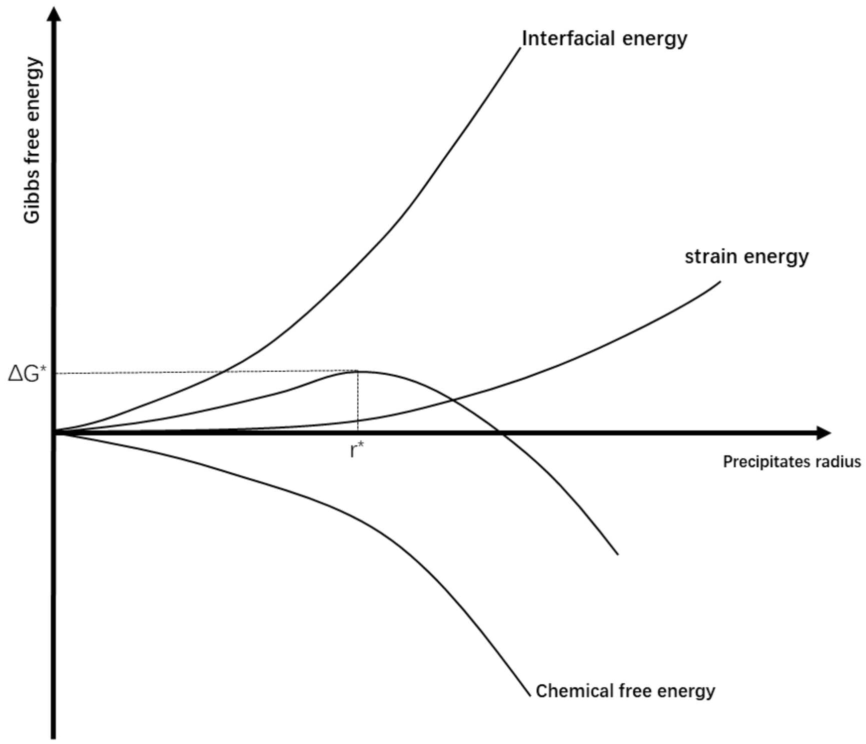

Figure 2.16 Schematic of the variation of Gibbs free energy with the precipitate radius during nucleation process. (@ZIMENG WANG)

The nucleation in precipitation process can be described as homogeneous nucleation, using the KWN nucleation model, this model is widely use for the prediction of precipitates in Al alloys[100]. The nucleation rate of precipitates can be written as[101]:

$$I = N_0 Z \beta^* \exp\left(-\frac{\Delta G^*}{k_b T}\right) \exp\left(-\frac{\tau}{t}\right) \qquad 2.1$$

where is the effective volume number density of nucleation sites in solid solution; and respectively, are the Zeldovich factor and the condensation rate of solute atoms in a cluster of critical size, respectively; is the critical net free energy of activation for formation of the critical nucleus; is the Boltzmann constant; T is the aging temperature; ; and t is aging time.

Theoretically studies on precipitates kinetics can help us systematically understand the precipitates evolution. Previous investigations[102-104] suggests that dislocations (edge type in particular) can effectively reduce the of transformation from coherent precipitates to incoherent precipitates, which means that some phases are likely to nucleate on dislocations. This prediction is consistent with experimental results of literature[105]. Also θ' is observed to directly precipitate on dislocations[6]. It is also report that when θ" transfer to θ' and θ' transfer to θ, the nucleation occurs at the interphase boundaries of a transition phases[106, 107].

For precipitates hardening alloys that serve at high temperatures, the strengthening phases must be stable at service temperature to maintain the toughness of the material. Taking Al-Cu alloys as an example, the coarsening of θ' precipitates will cause the loss in number density and increase in precipitate spacing, which lead to the reduction of mechanical properties. The details are discussed in Chapter 2.5. Moreover, the coarsening of θ' precipitates will at the end results in the transformation of θ' precipitates to equilibrium θ phase[84, 108, 109].

In the coarsening process, the size of larger precipitates increases at the cost of smaller ones dissolve, and the total volume fraction f of the precipitates stays virtually constant[84, 110]. Wagner[111] and Lifshitz and Slyozov[112] developed a theory (LSW theory) to describe the diffusion controlled coarsening process:

$$\mathrm{r}^3 - r_0^3 = k\Delta t \tag{2.2}$$

Where r is the average particle radius, r0 is the average radius at the onset of coarsening and k represents the rate constant which is also the only parameter of true physical significance in equation 2.2, and it can be calculated by[112, 113]:

$$\mathrm{k} = \frac{8c_\alpha(1 - c_\alpha)\gamma D V_m}{9RT\left(c_\beta - c_\alpha\right)^2} \tag{2.3}$$

where, is the atomic solid solubility of the relevant element in Al matrix, is the average interfacial energy of the precipitate, D is the diffusivity of the rate-controlling solute, , is the molar volume of the dispersed phase, is the ideal gas constant, and T is the absolute temperature. is the stoichiometric solubility of the element in the precipitation phase.

Wagner also considered the situation when interface reaction controls (IRC) the coarsening process, wherein the rate-limiting process is the transport of solute through the precipitate-matrix interface by an unspecified interface reaction, the equal for this condition can be written as[113]:

$$\mathrm{r}^2 - r_0^2 = k_R\Delta t \tag{2.4}$$

where k_R is a new rate constant that determined by the thermo-kinetic parameters of the system.

2.5 Strengthening models of precipitation strengthening

The precipitation strengthening has been extensively applied as the main strengthening method in heat-treatable aluminum alloys. The strength derives from the ability of precipitates to hinder the movement of dislocations, which makes it important to understand how dislocations interact with precipitates under applied stress[114, 115].

The precipitates-dislocations interactions can be classified into many categories based on the strength or the size of precipitates or if they are localized or diffuse[114]. Figure 2.17 shows the interaction between dislocation and point particles. When the dislocation moves forward and encounters the precipitates, it will bend into an arc with a radius of Rc, Γ represents the tension of dislocations which is an independent character of the dislocation, and the critical angle for the moving dislocation line to overcome the precipitates is Ψc. It is commonly believed that Ψc is related to the mechanism of dislocations-precipitations interaction. When Ψc<120°the dislocations bypass the precipitates when 120°<Ψc<180°. Fm is the maximum force that precipitates can stain and the relationship of Fm, Γ and Ψc can be written as:

$$F = 2\Gamma \cos\left(\frac{\psi_c}{2}\right) \qquad 2.5$$

Durin the interaction, a critical shear stress τc is required for dislocations to break free of the precipitates and it can be written as:

$$\tau_c = \frac{\Gamma}{bR_c} \qquad 2.6$$

Where b is the Burgers vector. And because the effective obstacle precipitates spacing L and Rc have a relationship as:

$$\sin\left(\frac{\theta_c}{2}\right) = \frac{L}{2R_c} \qquad 2.7$$

Where θc= π- Ψc, and the critical stress can be written as:

$$\tau_c = \frac{2\Gamma}{bL}\sin\left(\frac{\theta_c}{2}\right) \qquad 2.8$$

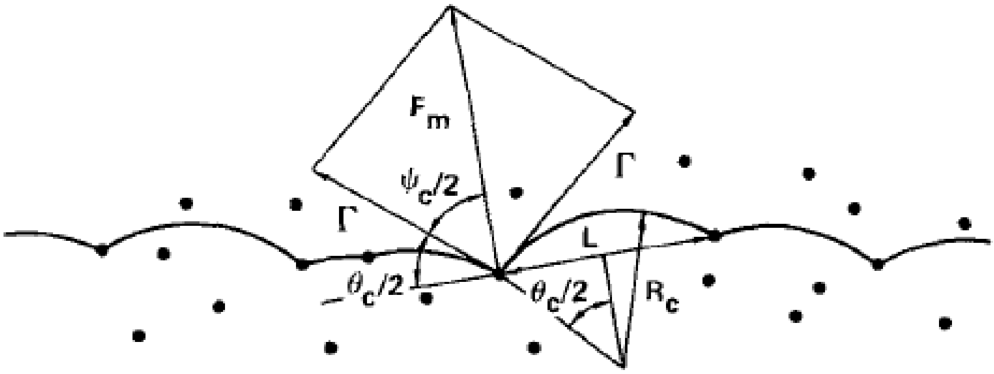

Figure 2.17 Schematic illustration of the penetration of a random array of point obstacles by a dislocation[114]. (@SPRINGER)

The mechanisms usually used to explain to explain the interaction are dislocation cutting through and dislocation bypass (Orowan) mechanisms[116]. At the beginning of aging, when the precipitates are small or not hard (deformable), they are coherent with the matrix. The dislocation can shear or cut through the precipitates, and the hinder effect will increase with the size of precipitates. And as aging proceeds, the precipitates will grow and coarse, becoming larger, or when the precipitates are harder (non-deformable), the dislocation will bypass the precipitates and leave a dislocation loop around the precipitates, and the hinder effect will decrease with precipitates size. The schematic is shown in Figure 2.18.

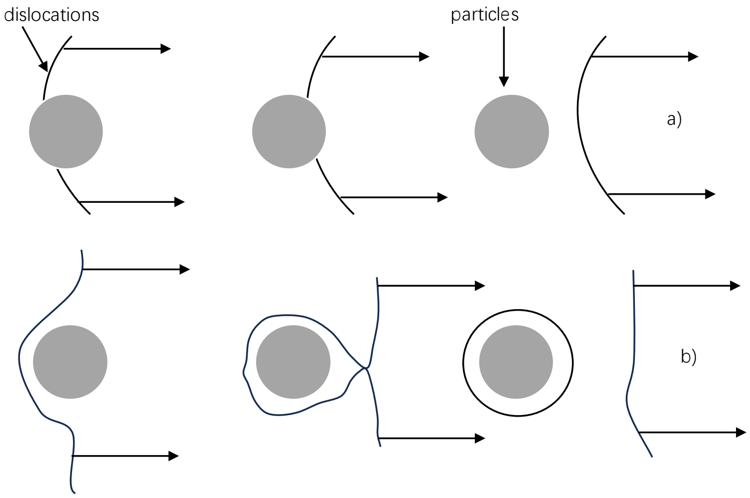

Figure 2.18 Dislocations passing a precipitate by a) shearing and b) looping (Orowan mechanism) c) Illustrates the different strength contributions to the total yield strength[115]. (@ZIMENG WANG)

In terms of the strengthening contribution, several mechanisms are developed: (1) Chemical strengthening; (2) Stacking-fault strengthening; (3) Modulus hardening; (4) Coherency strengthening; (5) Order strengthening. The last three are postulated to explain the dislocation shearing process[114].

The modulus hardening occurs when the shear moduli of the matrix and precipitates are different. The shear stress increment of it is given by[117]:

$$\Delta\tau_{cG} = 0.0055(\Delta G)^{\frac{3}{2}}\left(\frac{f}{\Gamma}\right)^{\frac{1}{2}} b(< r > b)^{-1+\frac{3m}{2}} \qquad 2.9$$

Where is the shear modulus mismatch between Al and precipitates, f is the volume fraction of precipitates m is a constant which is equal to 0.85.

The coherency strengthening is caused by elastic interaction between the strain fields of a coherent misfitting precipitate and the dislocation. The shear stress increment of it is given by[118]:

$$\Delta\tau_{cs} = \chi(\varepsilon G)^{\frac{3}{2}}\left(< r > \frac{fb}{\Gamma}\right)^{\frac{1}{2}} \tag{2.10}$$

Where is a constant varying between 2 and 3, ≈2/3δ where δ=Δa/a as the room temperature lattice parameter misfit.

The order strengthening is considered when the crystal structure of coherent precipitates is a superlattice and the matrix is a disordered solid solution. The shear stress increment of it is given by:

$$\Delta\tau_{os} = \frac{0.81\gamma_{apb}}{2b}\left(\frac{3\pi f}{8}\right)^{\frac{1}{2}} \tag{2.11}$$

Where is the antiphase boundary energy of the precipitates.

When calculating the total strength increment of dislocation shearing mechanism, the value is taken as the larger of the sum of modulus strengthening and coherency strengthening or the order strengthening as follow:

$$\Delta\sigma_{Shear} = \max\{(\mathrm{M}\cdot\Delta\tau_{os}), (\mathrm{M}\cdot\Delta\tau_{\mathrm{cG}} + \mathrm{M}\cdot\Delta\tau_{\mathrm{cs}})\} \tag{2.12}$$

Where M=3.06 is matrix orientation factor.

When dislocations bypass the precipitates, the Orowan mechanism is used to predict the shear stress increment. And when the precipitates are spherical or can be equivalent as spherical, it can be written as[92, 119]:

$$\Delta\tau_{Orowan} = \frac{0.4Gb}{\pi\lambda\sqrt{1-\upsilon}}\ln\frac{2r}{b} \tag{2.13}$$

Where ν=0.34 is the Poisson ratio of Al matrix and is the inter-precipitates spacing which is given as:

$$\lambda = \left[\left(\frac{3\pi}{4f}\right)^{\frac{1}{2}} - 1.64\right] \qquad 2.14$$

In Al-Cu alloys, the shear stress increment of θ' precipitates with true diameter d_t and thickness t_t can be calculated by[38]:

$$\Delta\tau_{\theta'} = \frac{Gb}{2\pi\sqrt{1-v}} \cdot \frac{1}{\frac{1.23 * 1.03}{\sqrt{N_v d_t}} - \frac{\pi d_t}{8} - 1.061 t_t} \cdot \ln 0.981 \frac{\sqrt{d_t t_t}}{b} \qquad 2.15$$

In practical situations, the shearable and non-shearable precipitates might exist in the matrix at the same time. The total critical resolved shear stress contributed by the shearing mechanism and Orowan mechanism is calculated by the ad hoc superposition law[120, 121]:

$$\Delta\tau^q = \Delta\tau_{shear}^q + \left[\left(\sum \Delta\tau_{orowan}^2\right)^{0.5}\right]^q \qquad 2.16$$

Where q is an exponent between 1 and 2, the value depends on the strength of the particles. It is found that when q=1.4, the prediction fits the experimental result the best for the combination of strong and weak particles, and the total strength contribution can be calculated by

$$\Delta\sigma = M \cdot \Delta\tau \qquad 2.17$$

CHAPTER 3 EXPERIMENTAL PROCEDURES

3.1 Alloys and Heat treatment

3.1.1 Alloys with various Si additions

In the first part of research, four different 224 alloys with various Si additions are designed and prepared using raw materials such as commercial pure Al (99.6%), pure Mg (99.9%), Al-50%Si, Al-50%Cu, Al-25%Mn and Al-5%Ti-1%B master alloys. Table 3.1 shows the chemical composition of each experimental alloy, which is analyzed by optical emission spectrometer.

Table 3.1 Chemical composition of 224 alloys with various Si addition (in unit of wt%)

Alloy #	Cu	Si	Fe	Mg	Mn	Ti	Al
0.1Si	4.24	**0.13**	0.17	0.11	0.32	0.098	Bal.
0.25Si	4.13	**0.26**	0.17	0.11	0.31	0.106	Bal.
0.5Si	4.24	**0.48**	0.17	0.11	0.33	0.098	Bal.
0.8Si	4.36	**0.77**	0.19	0.10	0.30	0.098	Bal.

The production of experimental alloys is followed by the same procedure: the prepared materials are first melted in a crucible heated in electric resistance furnace. The temperature is maintained at 750 °C for at least 30 mins to dissolve all elements and then Ar gas is injected for 15 mins for degassing. After degassing, the melted metal will be poured into a Y-shape permanent steel mold which is preheated at 250 ℃ by gravity casting technique. The ingot is shown in Figure 3.1.

Figure 3.1 Example of the ingot.

The schematic of heat-treatment applied to experimental alloys is shown in Figure 3.2. After casting, the alloys are solution treated with a 2-step method (495 ℃/2 h+528 ℃/10 h), followed by water quenching. After holding for 24 h, the alloys are then artificially aged at 200 ℃ for 4 hours, and then the samples are hold at different times of thermal exposure from 100 h to 1000 h at 300 ℃. The conditions are indicated by as-cast, T7, T7Ax (x represents the time of thermal exposure).

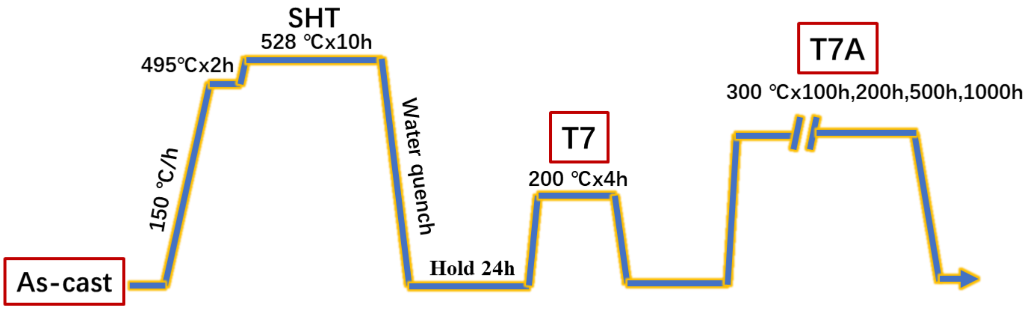

Figure 3.2 Schematic of heat-treatment for alloys with various Si addition.

3.1.2 Alloys with addition of transition elements

Zr, V, and Mn are introduced to the 0.5Si 224 alloy. The base alloy and the one with transition elements are marked as alloy O and alloy F. The chemical composition of them is shown in Table 3.2. Two different heat-treatment methods are applied to the experimental alloys in this part of the research and the parameters are shown in Table 3.3. The CHT is the same process that is applied to alloys with various Si additions, except that the solution temperature is 520 °C. This parameter is modified based on the result of energy-dispersive X-ray spectroscopy (EDS). Another heat-treatment method is designed to promote the precipitation of Al_3X precipitates and α-dispersoids, thus the alloys are first held at 300 °C for 24 h and then 425 °C for 24 h. To prevent the coarsening of α-dispersoids, the alloys are only solution treated for 2 h, then water quenched aged and annealed with the same process. The conditions are named in the same rule. Same as in chapter 3.1.1, the conditions are defined as T7(after aging) and T7Ax(after annealing).

Table 3.2 Chemical composition of designed high Si 224 alloys (in unit of wt%)

Alloys	Cu	Si	Fe	Mg	Ti	Mn	Zr	V	Al
O	4.85	0.48	0.25	0.12	0.16	**0.35**	**-**	**-**	Bal.
F	4.88	0.55	0.22	0.12	0.16	**0.70**	**0.17**	**0.25**	Bal.

Table 3.3 Heat treatment procedures for 0.5Si alloy with the addition of transition elements

Heat-treatments	Solution heat-treatment	Aging	Annealing
Conventional heat treatment (CHT)	495 ℃*2 h+528 ℃*10 h	200 ℃*4 h	300 ℃ *100 h&500 h
2-step heat treatment	300 ℃*24 h+425 ℃*24 h, +520 ℃*2 h	200 ℃*4 h	300 ℃ *100 h&500 h

3.2 Materials characterization

3.2.1 Microstructure analysis

Optical microscopy (OM), scanning electron microscopy (SEM), and transmission electron microscopy (TEM), were used to reveal the microstructures of experimental alloys. Samples for OM and SEM observation were prepared by the standard metallographic polishing procedure. Samples for TEM observation were first ground and polished to 40~60μm, then twin-jet in a solution consisting of 67% methanol and 33% nitric acid at 21voltage under -20~-30 ℃ to acquire a desirable thickness of foils. The thickness was measured using the two-beam convergent-beam diffraction pattern method.

Differential scanning calorimetry (DSC) was also utilized to investigate the microstructures of experimental alloys and to determine the solution heat treatment temperature as well as the formation of different phases in various experimental alloys. The heating rate is set at 10℃/min, and tests of each condition were repeated three times to ensure the reliability of the results.

3.2.2 Mechanical properties

The mechanical properties of experimental alloys were characterized by micro-hardness, compression yield strength tests and creep tests. Micro-hardness tests were conducted on the same samples for OM and SEM observation. Samples for compression yield strength tests were machined to φ10 mm x 15 mm cylinders, and the tests were conducted at both room temperature and 300 ℃ using the Gleeble 3800 thermomechanical testing system at the strain rate of 0.001/s. For compression creep tests, the parameters of the samples are the same as compression yield strength tests. Tests were conducted at 300 ℃ under a load of 30 MPa and the tests were generally stopped after 90 hours, or the total creep strain reached the limit before 90 h. 3 samples under each condition were tested for both compression yield strength and creep tests.

CHAPTER 4 The effect of Si on precipitates evolution and mechanical properties during the thermal exposure in Al-Cu 224 alloys

Although Si is considered as an impurity in Al-Cu casting alloys, it has great potential to improve castability[45], however, there is limited open literature on the influence of Si on the mechanical properties during the long time thermal exposure in Al-Cu cast alloys. Therefore, this chapter focuses on the effect of various Si contents on the evolution of microstructure and mechanical properties of Al-Cu alloys during thermal exposure at 300 ℃. Samples under T7 heat-treatment are marked as "T7", while samples under thermal exposing at 300 ℃ after T7 are marked as "T7A" (details shown in Chapter 3). The mechanical properties at both room-temperature and elevated-temperature are characterized by compression tests, while the creep resistance is obtained from the compression creep test at 300 ℃.

4.1 Results

4.1.1 Evolution of microstructure with Si additions

4.1.1.1 As-cast condition

The typical microstructures of experimental alloys at the as-cast condition are shown in Figure 4.1. It is generally composed of α-Al, Al_2Cu and Fe intermetallic (Fe IMCs). However, the differences in the as-cast microstructure are observed due to the Si addition that the variety and morphology of Fe intermetallic phases highly depend on the addition of Si. In low Si alloys (Figure 4.1 a)), two types of Fe IMCs phase were observed by OM: plate-like $Al_7Cu_2(Mn, Fe)$, known as β-Fe IMCs and Chinese script-like $Al_{15}(Mn, Fe)_3(Cu, Si)_2$, known as α-Fe IMCs. While in high Si alloys shown in Figure 4.1 b), only α-Fe IMCs were observed. This phenomenon indicates that the addition of Si leads to the transformation of β-Fe IMCs to α-Fe IMCs. Results were also reported in the literature[73, 122, 123] that Si can promote the formation of α-Fe IMCs and suppress the formation of β-Fe.

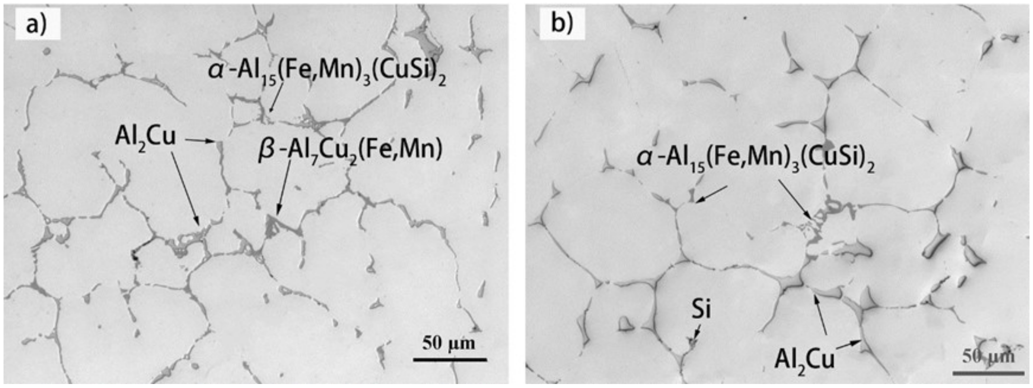

Figure 4.1 Typical as-cast microstructures of experimental alloys: a) 0.1Si alloy, b) 0.8Si alloy.

To further investigate the microstructures at the as-cast condition, DSC tests of 4 experimental alloys were conducted. Figure 4.2 shows the first derivate of heating curves of each alloy, and Table 4.1 summarizes the peaks that represent different phases. Peaks 2 and 3 corresponding to β-Fe IMCs and α-Fe IMCs, separately, directly indicate the co-existence of these two phases in 0.1Si alloy, 0.25Si alloy and 0.5Si alloy. However, the peak of β-Fe in 0.5Si alloy is very weak, and this phase was even hard to observe by OM. In 0.8Si alloy, the peak of β-Fe IMCs is completely disappeared. Peak 4 represents the Al_2Cu phase. With the increase in Si content, the peak temperature of Al_2Cu decreases from 543 ℃ (0.1Si alloy) to 530 ℃ (0.8Si alloy). Peak 5 at 519 ℃ is the peak of eutectic Si, which only appears in 0.8Si alloy, confirming the Si particles observed in the microstructure of 0.8Si by OM (Figure 4.1).

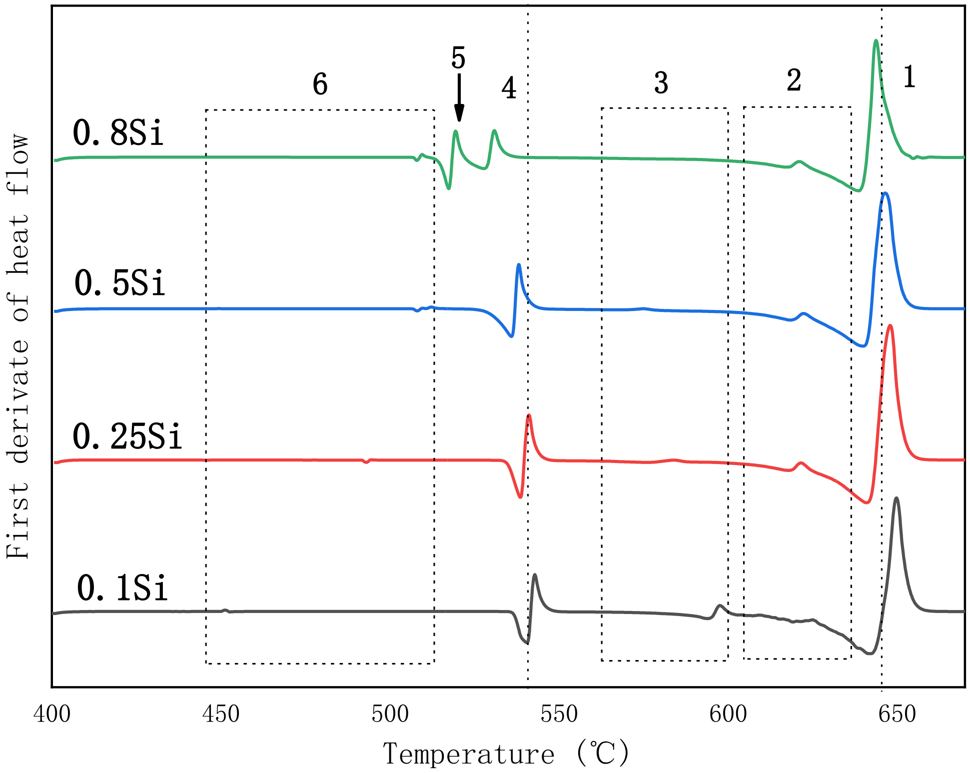

Figure 4.2 DCS first derivate of heating curves of 4 experimental alloys at as-cast condition.

Table 4.1 Peaks identification of DSC curves.

Peak	1	2	3	4	5	6
Phase	α-Al	α-Fe IMCs	β-Fe IMCs	Al_2Cu	Eutectic Si	Al_2CuMg[51]

4.1.1.2 T7 condition

Figure 4.3 shows the typical microstructures of the experimental alloys at T7 condition. After 10 h solution heat-treatment (SHT) at 528 °C, Al_2Cu is well dissolved into the matrix, while the Chinese script α Fe-IMCs and platelet β Fe-IMCs have remained as the dominant phases. In 0.1Si alloy (Figure 4.3 a)), two types of Fe-IMCs are both found. It is reported that during solution heat-treatment, α Fe-IMCs will become unstable and progressively transform into β Fe-IMCs[51]. However, with high Si contents, α-Fe tends to be stabilized and shows resistance to the transformation. Table 4.2 shows the area fraction of Fe-IMCs of each alloy at T7 condition, which indicates that the Fe-IMCs in each alloy are at a similar level.

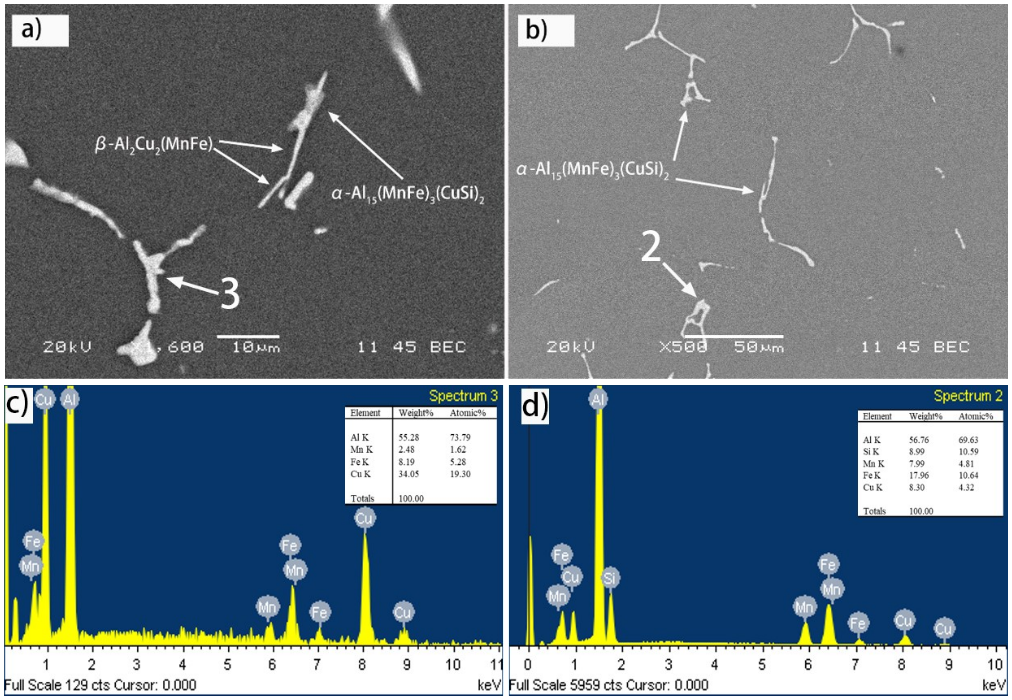

Spectrum 3

Element	Weight%	Atomic%
Al K	55.28	73.79
Mn K	2.48	1.62
Fe K	8.19	5.28
Cu K	34.05	19.30
Totals	100.00	

Spectrum 2

Element	Weight%	Atomic%
Al K	56.76	69.63
Si K	8.99	10.59
Mn K	7.99	4.81
Fe K	17.96	10.64
Cu K	8.30	4.32
Totals	100.00	

Figure 4.3 SEM backscatter electron images with EDS analysis results: a), c) 0.1Si alloy, b) d) 0.8Si.

Table 4.2 Area fraction of Fe-IMCs after T7 condition.

Alloy	0.1Si	0.25Si	0.5Si	0.8Si
Fe-IMCs area fraction/%	1.31±0.35	1.38±0.39	1.52±0.49	1.47±0.49

To reveal the microstructure changes caused by various Si contents, especially on the precipitates, detailed TEM observations were performed on different experimental alloys under T7 condition. Figure 4.4 shows the bright-field (BF) TEM images of experimental alloys at T7 condition. The co-existence of fine and homogenously distributed θ” precipitates and θ’ precipitates was observed in each alloy, but the presence of θ’ precipitates is dominant. The TEM results under T7 condition of experimental alloys demonstrate that the addition of Si promotes the precipitation of θ’ precipitates. The comparison of experimental alloys shows an obvious difference, as higher Si alloys have a greater number density of θ’ precipitates.

Table 4.3 shows the TEM quantification results of precipitates under T7 condition. It can be found that the number density and volume fraction of θ’ has been significantly increased with Si. In 0.8Si alloy, the number density of θ’ is even twofold compared with 0.1Si alloy. In contrast, the true diameter of θ’ precipitates only increases from 86.4 nm in 0.1Si alloy to 88.0 nm in 0.25Si alloy and then drops to 68.0 nm in 0.8Si alloy. The reduction of size has a negative effect on its contribution to yield strength[38] and it results in a milder growth of yield strength from 0.25Si to 0.8Si. Mitlin et al.[52] found that in the Al-2Cu-1Si alloy, Si clusters can act as nucleation of θ’ precipitates, because the strain energy of θ’ precipitates is considerably low if they nucleate on pre-existing Si clusters. In a recent study on Al-Cu-Mn-Zr alloys, Patrick et al.[57] proposed that the nucleation of θ’ precipitates on Si clusters is the reason for the decreased size and increased number density, because Si reduces the α-Al/θ’ precipitates interfacial energy and thermal dynamically stabilizes the formation of θ’ precipitates, therefore the critical nucleus size of θ’ precipitates[1, 124]. In the current TEM results, θ” precipitates only have a very small volume fraction and low number density compared with θ’ precipitates. Their size is quite similar in different experimental alloys. It might be suppressed by the transformation to θ’ precipitates since θ’ precipitates can also nucleate on θ” precipitates as aging proceeds. Notably, no literature mentions Si could significantly affect the size of θ”. Aniruddha et al.[7] reported that Si-rich θ” precipitates are more likely to nucleate θ’ precipitates, so we expected a decrease of number density with Si. But an interesting phenomenon we observed is that the number density of θ” first increases with Si and then has an upswing from 0.5Si alloy to 0.8Si alloy. A possible reason is that the solution treatment temperature (528 °C) is considered high for 0.8Si alloy, which might cause more quenched-in vacancies in 0.8Si alloy. Literature has reported that quenched-in vacancies play an important role in the solid solution decomposition and the creation of dislocation loops[125, 126], which can act as nucleation sites for θ” precipitates[19]. Thus, the quenched-in vacancies can lead to an increase of number density of θ” precipitates in 0.8Si alloy.

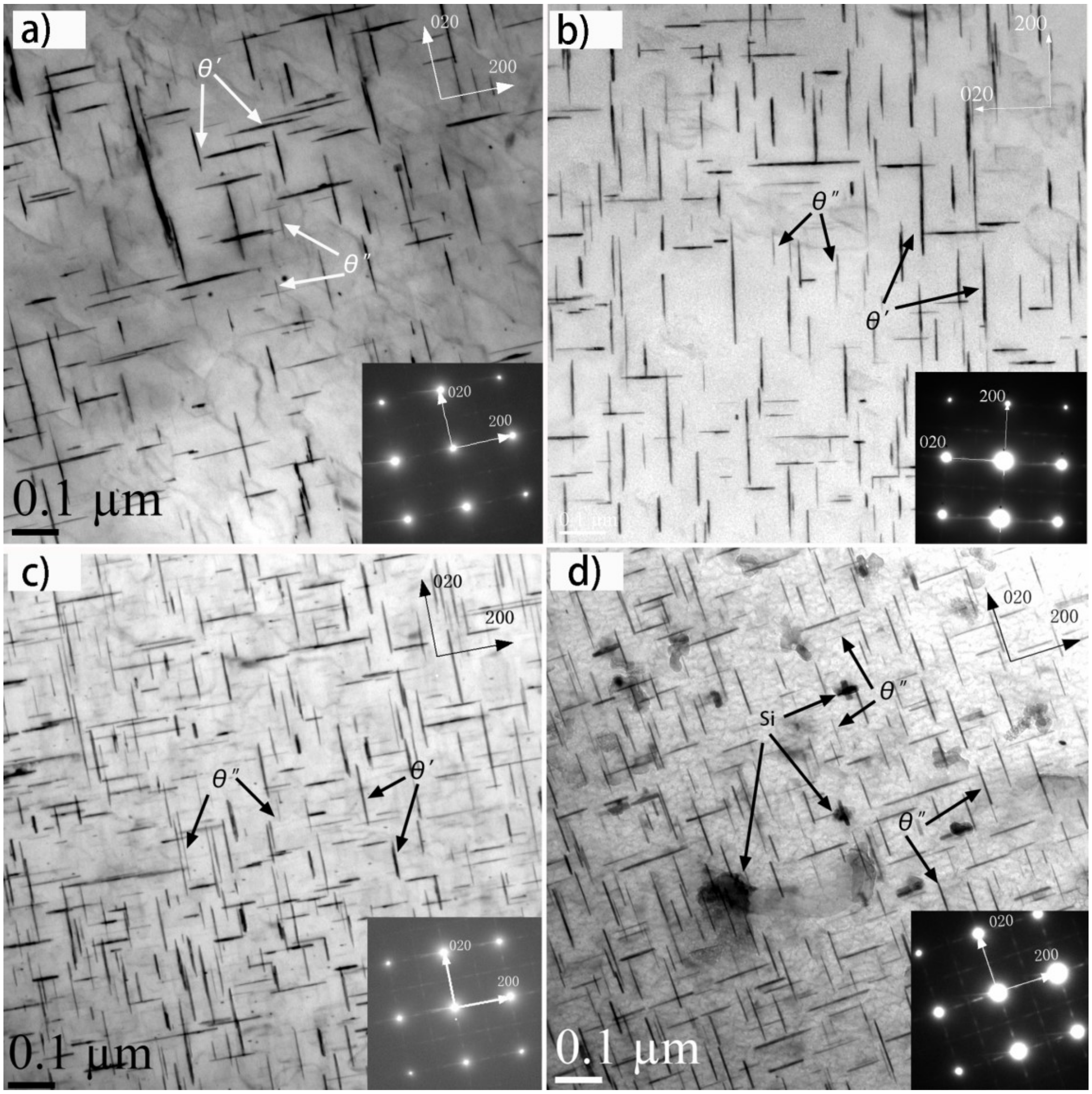

Figure 4.4 BF-TEM images and corresponding SAEDPs of experimental alloys at T7 condition: a) 0.1Si alloy, b) 0.25Si alloy, c) 0.5Si alloy, d) 0.8Si alloy.

Table 4.3 Quantification result of θ’ and θ” precipitates at T7 condition.

Conditions		dt/nm	tt/nm	Nv/μm^{-3}	f/%	Δτ/MPa	σp/MPa
0.1Si	θ”	30.2	3.2	571	0.11	12.8	228.0
	θ’	86.4	4.9	1236	3.47	73.4	
0.25Si	θ”	26.4	3.0	524	0.09	9.7	272.4
	θ’	88.0	5.6	1416	4.66	88.5	
0.5Si	θ”	34.2	3.3	210	0.06	9.5	285.1
	θ’	76.4	6.3	1948	5.88	92.7	
0.8Si	θ”	34.0	3.0	424	0.13	12.7	294.2
	θ’	68.0	6.2	2473	5.87	95.3	

(dt=true diameter, tt=thickness, Nv=number density, f=volume fraction, Δτ=critical resolved shear stress (CRSS), σp=yield strength contribution by precipitates strengthening)

4.1.1.3 T7A conditions

Figure 4.5 shows the BF-TEM images of three experimental alloys after different thermal exposure times. The quantification results of θ’ precipitates are also given in Table 4.4. There are no θ” precipitates observed in the microstructures of any alloy at any T7A condition.

In 0.1Si alloy, θ’ precipitates retained the plate-like shape with an obvious reduction of number density (Figure 4.5) during 1000 h thermal exposure. There are still some finer θ’ precipitates that can be observed (0.1Si T7A1000. The quantitative results show the increase in size and reduction of volume fraction and number density of θ’ precipitates. The equilibrium θ phase is not typical to find in 0.1Si alloy as the volume fraction of θ’ precipitates does not change much with thermal exposure time. The evolution of θ’ precipitates is principally growth and coarsening.

In 0.5Si and 0.8Si alloys, the trend of θ’ precipitates evolution is similar to 0.1Si alloy during exposure. Nevertheless, these two alloys exhibit a significant change in size, volume fraction, and number density of θ’ precipitates. Si particles were found in 0.8Si alloy along with coarsened and large θ’ precipitates which are marked as Si-rich precipitates. And it seems that the Si segregation is the key reason for the coarsening of θ’ precipitates. The identification of Si-rich precipitates is based on Si’s rapid diffusivity and ability to partition in θ’ precipitates. Patrick et al.[57] observed an approximately 5 times greater Si content within precipitates in a 0.24 wt% Si content Al-Cu alloy than low Si alloys (lower than 0.1wt% Si). Thus, it is not difficult to believe that in the same alloy, θ’ precipitates that are closer to Si segregations are most likely to be Si-rich, leading to their higher coarsening rate. The true diameter of θ’ precipitates in 0.8Si alloy even reduces from 148.1nm at T7A500 condition to 116.6nm at T7A1000 condition due to the dramatic reduction of number density, mostly because the transformation to θ phase occurs at a critical aspect ratio on large θ’ precipitates[127]. The equilibrium θ phase commonly exists in these two alloys, indicating that the transformation of θ’ precipitates also plays an important role in the microstructure evolution.

When compared TEM images vertically, Figure 4.5 also demonstrates the microstructure evolution with increasing Si at the same T7A conditions. High Si alloys have less finer but more coarsened θ’ precipitates. The dramatic increase in size and reduction of the number density of θ’ precipitates leads to a drop of CRSS with Si. Figure 4.6 shows the distribution of the thickness of θ’ precipitates at T7A100 condition. Θ’ precipitates that have a thickness between 5~10nm take up the largest proportion in each alloy. In 0.1Si alloy, the average thickness is also in this area and nearly 60% of θ’ precipitates have a thickness similar to the average thickness. As Si content increases, the average thickness of θ’ increases due to the creasing proportion of thick precipitates. The distribution tends to deviate from the normal distribution, which means more θ’ precipitates in high Si alloys are either finer or coarser than the average thickness. This could be linked to the non-uniform distribution of Si, as Si-rich θ’ precipitates might coarsen faster than non-Si-rich θ’ precipitates.

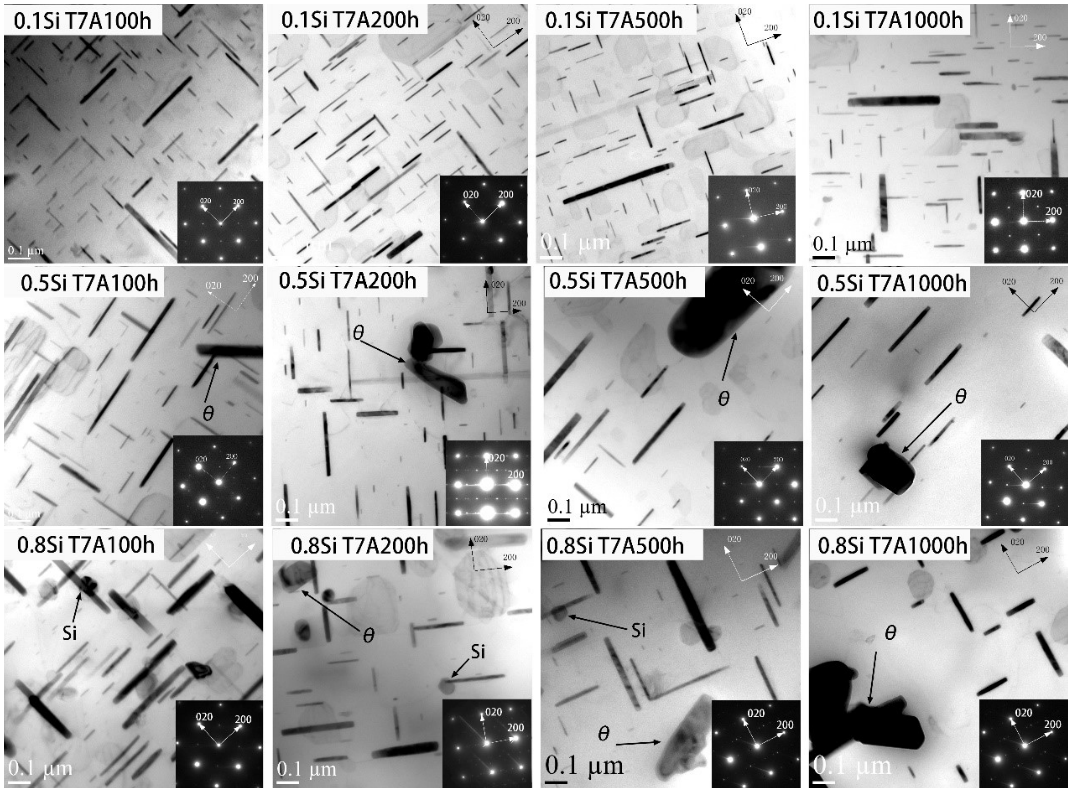

Figure 4.5 BF-TEM images and corresponding SAEDPs of experimental alloys at different T7A conditions.

Table 4.4 Quantification result of θ’ precipitates at T7A conditions.

Conditions		dt/nm	Thickness/nm	Nv/μm-3	f/%	Δτ/MPa	σp/MPa
T7A100h	0.1Si	85.8	7.3	498	2.14	41.9	128.3
	0.5Si	104.7	10.3	239	2.67	33.7	103.1
	0.8Si	111.5	14.8	104	2.93	22.6	69.3
T7A200h	0.1Si	88.1	7.8	458	1.76	41.2	126.2
	0.5Si	109.5	12.5	184	2.03	26.6	81.5
	0.8Si	123.7	16.2	75	2.38	20.6	63.0
T7A500h	0.1Si	98.6	8.4	396	1.75	36.4	111.4
	0.5Si	116.7	12.9	98	1.45	22.3	68.1
	0.8Si	148.1	17.8	51	1.54	19.3	59.1
T7A1000h	0.1Si	103.1	12.8	209	1.48	31.6	96.8
	0.5Si	134.8	15.8	58	1.37	18.9	57.9

0.8Si	116.6	22.9	48	1.19	15.9	48.7

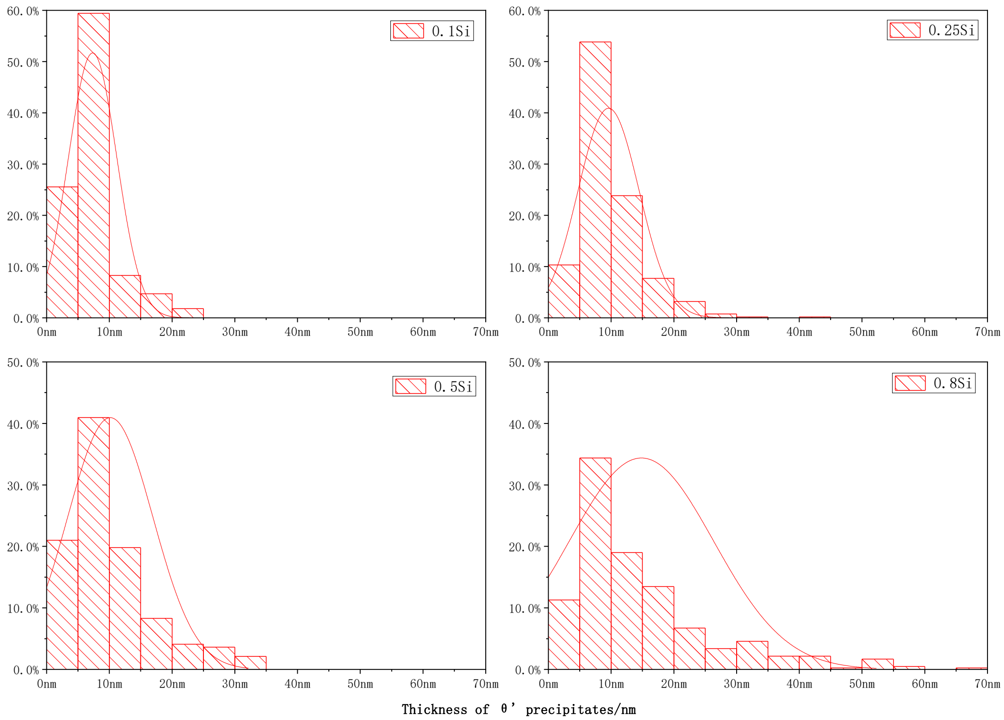

Figure 4.6 Distribution of the thickness of θ' precipitates at T7A100 condition.

4.1.2 Evolution of mechanical properties with Si

4.1.2.1 As-cast condition

Figure 4.7 shows the microhardness of experimental alloys at as-cast condition. As Si content increases, the microhardness increases. A quantitative analysis of Al_2Cu area fraction was performed based of OM images by IMAGEJ software. The results in Table 4.5 demonstrates that with increased Si content, the area fraction of Al_2Cu has a trend of increasing because Si can promote the solubility of Cu in Al[52]. This is in agreement with reference[45]. The decrease of Al_2Cu means a higher Cu concentration in the matrix, the transformation of Fe

IMCs also released certain Cu atoms into the matrix[128]. These two phenomena can be used to explain the growth of microhardness with Si, as the mechanical properties of experimental alloys at as-cast condition are mainly contributed by solution solid strengthening.

Table 4.5 Al_2Cu area fraction of 4 experimental alloys at as-cast condition.

Alloys	0.1Si	0.25Si	0.5Si	0.8Si
Area fraction of Al_2Cu/%	3.1±0.6	2.5±0.4	2.2±0.3	2.1±0.4

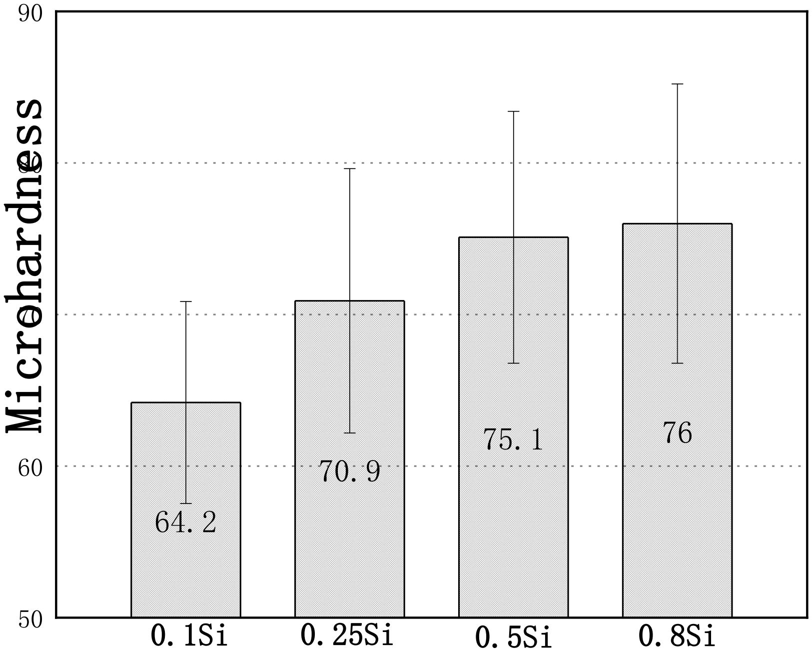

Figure 4.7 Microhardness of experimental alloys at as-cast condition.

4.1.2.2 T7 &T7A conditions

For T7 conditions, the compression yield strength of experimental alloys at both room temperature and 300 °C is shown in Figure 4.8. Noticeably, the alloying of Si increases the compression yield strength at both room temperature and 300 °C. At room temperature, the increase of yield strength is from 316 MPa in 0.1Si alloy to 355 MPa in 0.8Si alloy, while at 300 °C, it increases from 120 MPa in 0.1Si alloy to 139 MPa in 0.8Si alloy. Despite the improvement in general, it is indisputable that the increase of YS of alloys at lower Si contents (0.1Si and 0.25Si) is significant with less increase in Si content than from 0.25Si to 0.8Si, whereas the YS almost remains at the same level. Besides, with increasing testing temperature, each alloy suffers a thermal softening. The YS at 300 °C is ~40% of the YS at room temperature for 4 experimental alloys.

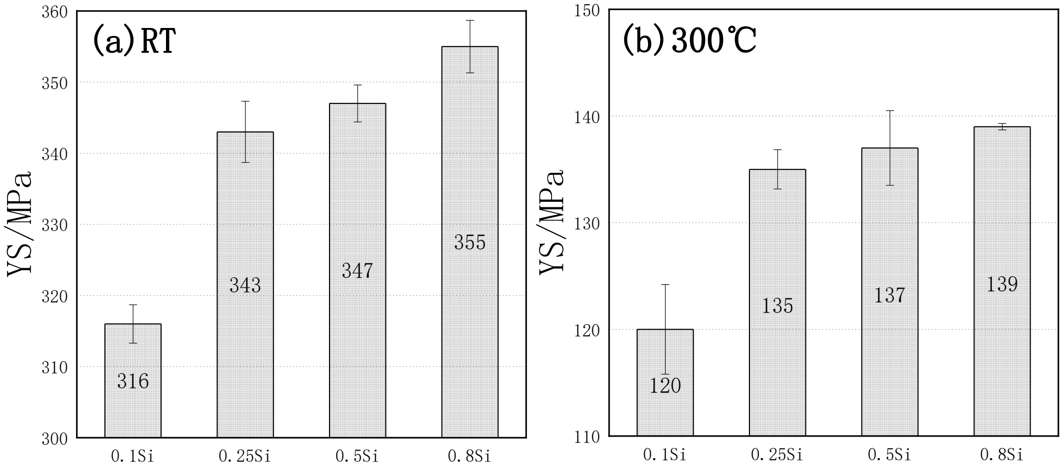

Figure 4.8 Compression yield strength of experimental alloys at T7 condition: a) at RT, b) at 300 °C.

Long-term thermal stability is very critical to the high-temperature resistance of Al alloys. After different times (up to 1000 h) of thermal exposure at 300 °C, the compression yield strength tests of experimental alloys are conducted and the results are shown in Figure 4.9, which indicates a reversed relationship between yield strength and Si contents to that at T7 condition that yield strength decreases with Si contents. Moreover, yield strength also drops with increasing thermal exposure time for all experimental alloys. However, the decreasing pattern varies with Si contents, which becomes much more severe in high Si alloys. Taking the exposure time of 100 h as an example, comparing Figure 4.8 a) and Figure 4.9 a), it can be observed that 0.1Si alloy loses 46% (from 316 MPa to 170 MPa) of yield strength at room temperature. This number is much higher in 0.8Si alloy, in which the loss of yield strength at room temperature is 70% (from 355 MPa to 107 MPa). Through this, a great challenge can be expected for the mechanical property enhancement in high Si alloys. As the time of thermal exposure elapses, the yield strength of each alloy further decreases. For 0.5Si and 0.8Si alloys, the yield strength first drops significantly, but after 200 h thermal exposure, the trend of decreasing becomes less obvious. And the yield strength at 300 °C of these two alloys tends to stabilize after 500 h thermal exposure. 0.1Si and 0.25Si alloys have a relatively mild loss of yield strength during thermal exposure, and no platform can be observed in yield strength curves.

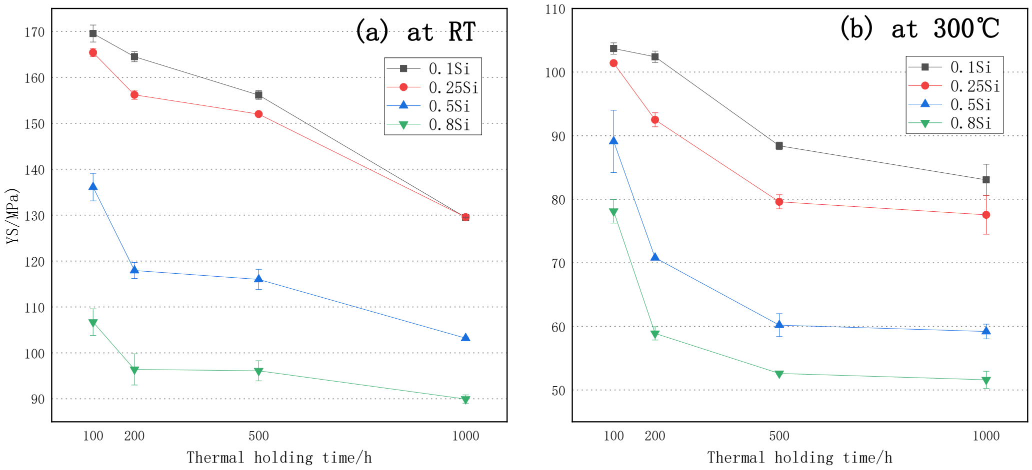

Figure 4.9 Compression yield strength of experimental alloys at T7A conditions.

4.1.3 Evolution of creep behavior with Si

The elevated-temperature properties of experimental alloys at different T7A conditions are also characterized by compression creep tests at 300 °C under 30 MPa for 90 h. The typical creep curves are shown in Figure 4.10. The steady creep rates are calculated and given in figure 4.11, which is used to characterize the creep resistance of alloys combined with the total creep strain.

Among three experimental alloys, 0.1Si alloy has the best creep resistance. The creep strain of 0.1Si alloy increases rapidly in the first few hours, and then slightly increases with time, which is the symbol of turning into the quais-steady stage. The steady creep rate and total strain of it increase with increasing thermal exposure time. 0.1SiT7A500 reaches the highest steady creep and total strain (1.6×10^{-8}/s and 0.27 separately), but the values are still much lower compared with 0.5Si and 0.8Si alloys at the same condition.

0.5Si shows a similar tendency to 0.1Si but with much higher total strains and steady creep rates and the creep strain increases faster with time. This could be explained by the lack of strengthening θ' precipitates acting as dislocation movement barriers in 0.5Si alloy. The microstructures are presented in Figure 4.5. In Figure 4.11, it is obvious to observe that the steady creep rate of 0.5Si increases faster with the thermal exposure time of test samples; this is related to the faster coarsening of θ' precipitates observed in 0.5Si compared with 0.1Si.

Unlike 0.1Si and 0.5Si alloys, the creep test results of 0.8Si alloy display an antithetic pattern. The total strain decreases with the thermal holding time of the samples, and the creep curves are divided into two stages. For T7A100 condition, it has a much higher total strain and creep rate at the first stage, for the other two conditions, the creep rate and total strain are higher in the second stage. The creep rates of each condition in the first stage are very different, however, in the second stage, there is only a slight decrease with Si as shown in Figure 4.11.

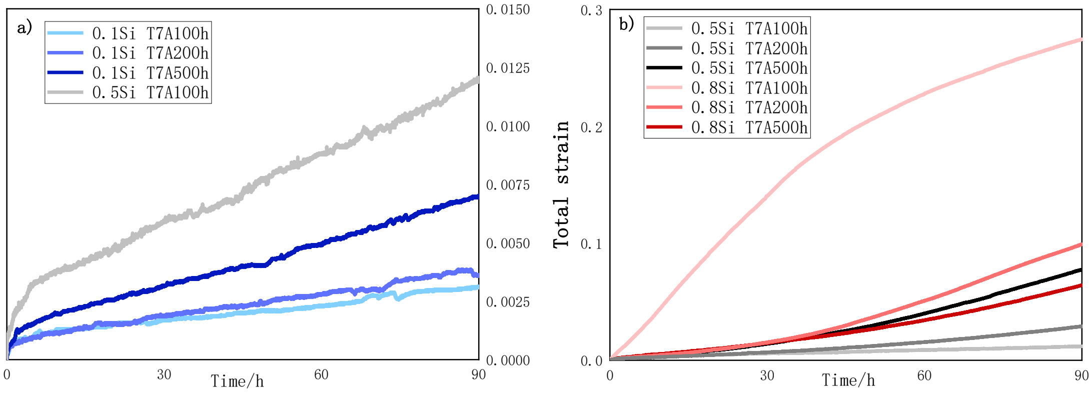

Figure 4.10 Typical creep curves of experimental alloys.

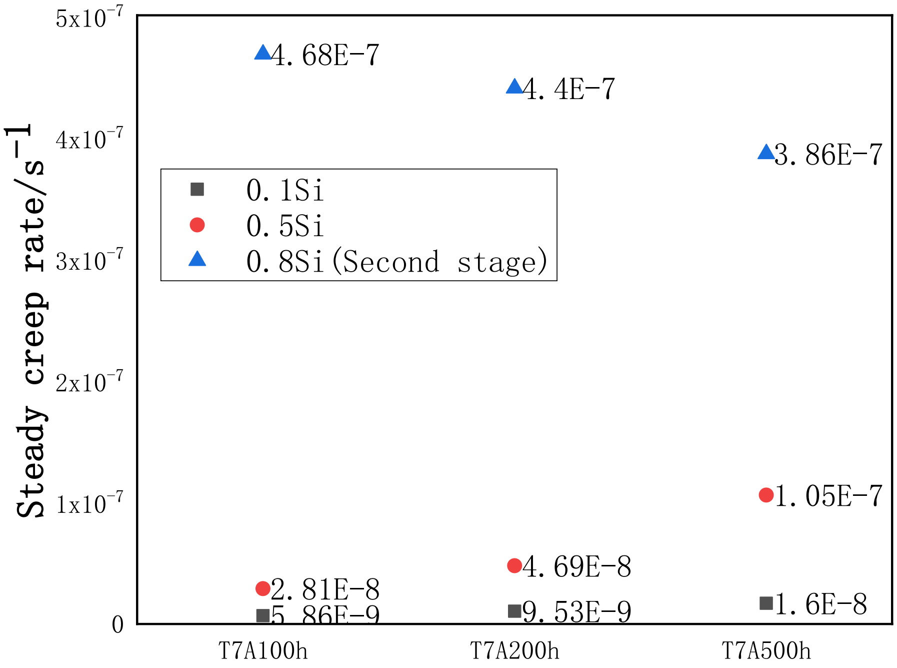

Figure 4.11 Calculated steady creep rates of experimental alloys.

To further investigate the creep behavior, TEM images of 0.1Si and 0.8Si T7A100 crept samples are taken to reveal the typical microstructure after creep tests. Figure 4.12 shows that after creep tests, the plate-like θ’ in 0.1Si alloy still retains the same morphology and fine size. No obvious dislocations or grain boundary sliding are observed. In 0.8Si alloy, different microstructures are observed in different grain boundaries. Figure 4.13 a) shows a significantly low number density of θ’ precipitates with a tilted angle with their habit plane, indicating they are losing the semi-coherent interface with α-Al. Small size α-dispersoids are observed and confirmed by TEM EDS, unlike blocky or rod-like morphology[129], the α-dispersoids in 0.8SiT7A100 crept samples are in small round shape, which means it is formed during creep tests, since they are not observed at 0.8Si T7A100 condition (Figure 4.5). This phenomenon can explain why the creep curves are divided into 2 stages. Because the newly formed α-dispersoids are more thermal stable at 300 °C than θ’ precipitates, and can effectively act as the dislocation movement barriers, resulting in a slower steady creepy rate. Another typical structure is shown in Fig 4.13 b) with relatively dense θ’ precipitates. The interaction between dislocations and precipitates was not observed like in Fig 4.13 a). Also, Si particles, which still exist at 0.8Si T7A200 condition, are not found at the 0.8Si T7A 100 h crept condition. This means the creep test accelerates Si atoms to partition to θ’ precipitates; this process can cause more Si-rich precipitates, which will further accelerate the coarsening of θ’ precipitates leading to poor creep resistance.

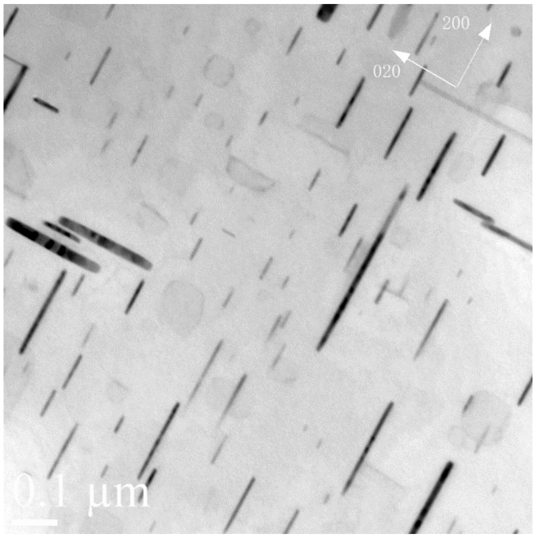

Figure 4.12 . BF-TEM image of 0.1Si T7A100 after 90 h creep test under 30 MPa at 300 °C.

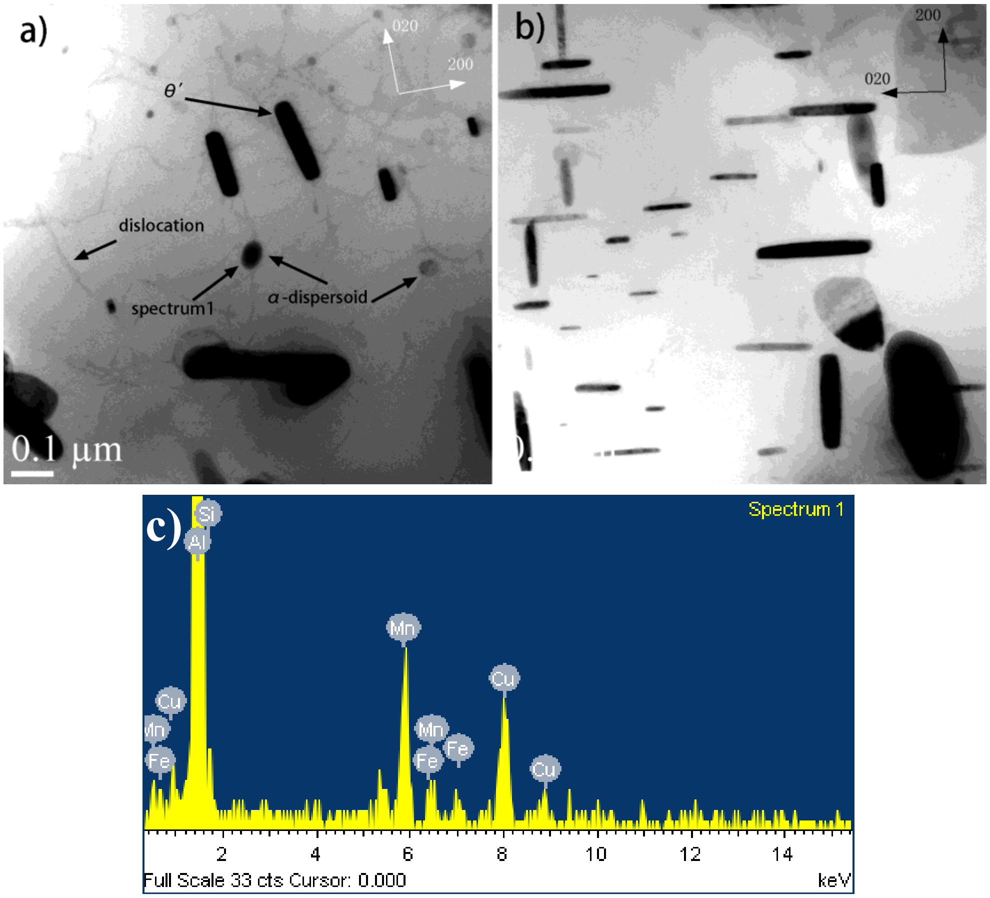

Figure 4.13 a), b) BF-TEM images of 0.8Si T7A100 after 90 h creep test under 30 MPa at 300 °C, and c) EDS analysis result.

4.2 Discussion

4.2.1.1 Formation and coarsening behavior of precipitates with Si additions

The coarsening behavior of θ' precipitates is an important part of microstructure evolution during thermal exposure. The thermal stability of experimental alloys is directly and largely reflected by it, as θ' precipitates is the main strengthening precipitates. The coarsened θ' precipitates, as the result, will weaken the strengthening effect, compared with fine precipitates. The thermodynamically driven coarsening of θ’ precipitates can be modeled by following equation [19, 130]:

$$\bar{r}^n - \bar{r}_0^n = k(t - t_0) \tag{1}$$

Where is the mean radius of θ’ precipitates at the time t; is mean radius of θ’ precipitates at starting time, which is corresponding to the T7 condition in this study; t is the thermal exposure time; t_0 is the starting time, which is the T7 condition; k is described as a coarsening rate constant to evaluate the coarsening rate of θ' precipitates; and n is the temporal exponent, which is determined by coarsening mechanism. When coarsening is controlled by volume diffusion, θ’ precipitates follow the $t^{1/3}$ law (n=3)[19, 131, 132]; and when interfacing kinetic takes control, it tends to obey the $t^{1/2}$ law[133, 134].

$t^{1/2}$ law and $t^{1/3}$ law are examined separately in this study revealing that experimental data shows good linear fitting results under both laws with high value of the coefficient of determination R^2. The statistical results are shown in Fig 4.14 (for the sake of simplicity, only the results of the $t^{1/3}$ law are presented), and Table 4.6 summarizes the values of k for different experimental alloys. Clearly, the increase of Si content increases the k value for θ’ precipitates. In 0.5Si and 0.8Si alloys, the data points are divided into 2 stages, indicating a significant drop of coarsening rate after 200h thermal exposure. By taking the derivative of with respect to t in equation (1) when n=3, we can get:

$$\frac{\partial \bar{r}}{\partial t} = \frac{k}{3(k \cdot t + r_0^3)^{\frac{2}{3}}} \tag{2}$$

Which simply shows the coarsening rate will decrease as increases, therefore as thermal exposure proceeds.

Due to the difficulty of measuring important parameters, it is hard to modify the LSW equation by calculating the interfacial energy or diffusion coefficient of solute to further investigate the coarsening mechanism. However, the faster coarsening rate with higher Si contents does not match with the reduction of interfacial energy caused by Si based on $t^{1/2}$ law. So, here we try to make an explanation according to $t^{1/3}$ law. But note that the actual situation could be more complex.

At T7 condition, the dense θ' precipitates are observed in high Si alloys. The short inter-precipitates spacing and small precipitates size (of higher surface to volume ratio) that cause the high number density of θ' precipitates are believed to increase the coarsening rate, as they lead to a decreased diffusion distance between precipitates. Patrick et al. [57] also reported that larger precipitates and greater inter-precipitates spacing can provide additional time for the segregation of Mn and Zr as stabilizers. This is consistent with the experimental 0.1Si alloy.

For T7A conditions, high Si alloys have larger size θ' precipitates and greater inter-precipitates spacing but still with larger coarsening rate constant k. Here, a hypothesis is proposed that there are two types of θ' precipitates in high Si alloys: Si-rich θ' precipitates and non-Si-rich θ' precipitates caused by the nonuniform distribution of Si. Si-rich θ' precipitates generally coarsen faster than non-Si-rich θ' precipitates when other parameters are the same. And when Si segregates next to a θ' precipitate, the precipitate will coarsen faster than others without Si segregation. This theory is put forward on the basis of few facts: 1) Si has a high diffusion coefficient in Al matrix; 2) Si particles are always observed in 0.8Si alloy along with large-size precipitates; 3) Si can be partition to Cu sublattices in the precipitates, leading to high Si concentration in θ' precipitates; 4) with larger-size θ' precipitates and greater inter-precipitates spacing, high Si alloys still have higher coarsening rates. The schematic of the proposed mechanism is shown in Figure 4.15.

Table 4.6 Coarsening rate constant k of different experimental alloys.

Alloys		k/(nm^3/h)	R^2
0.1Si	0~1000 h	13.8	95.0
0.5Si	0~200 h	73.0	98.9
	200~1000 h	21.5	93.8
0.8Si	0~200 h	167.0	93.5
	200~1000 h	31.3	99.5

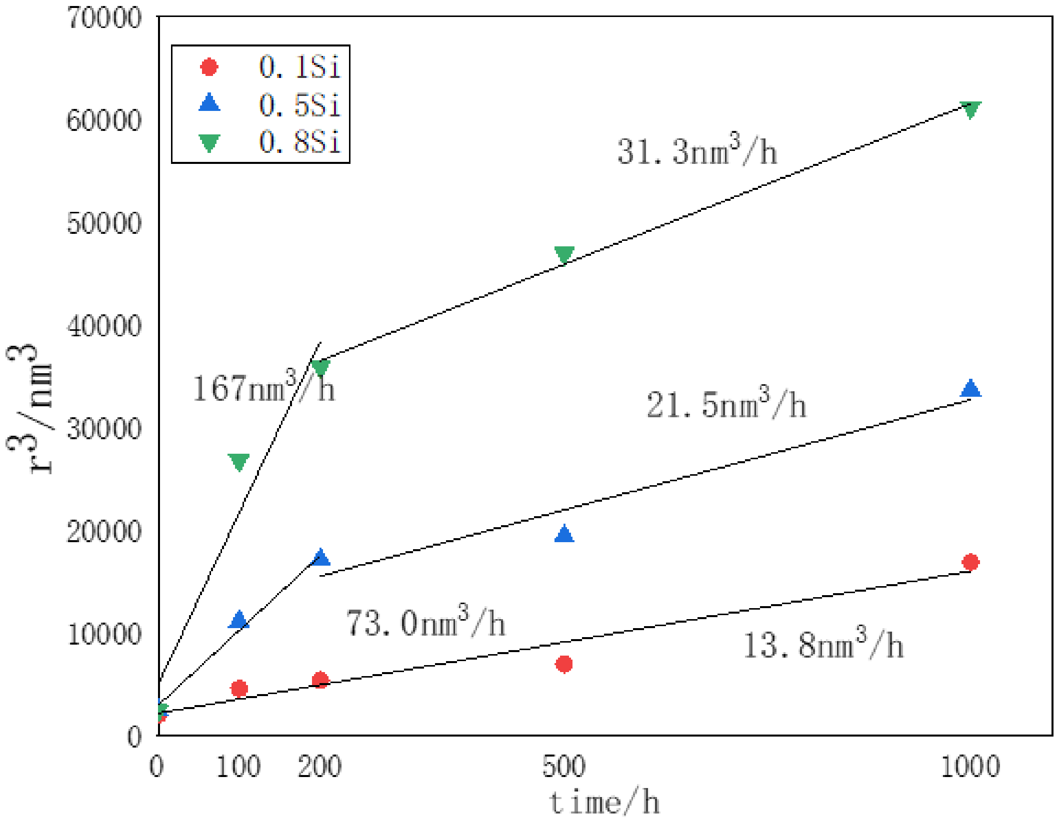

Figure 4.14 The statistical results on the coarsening evolution of θ’ precipitates (0 h stands for T7 condition).

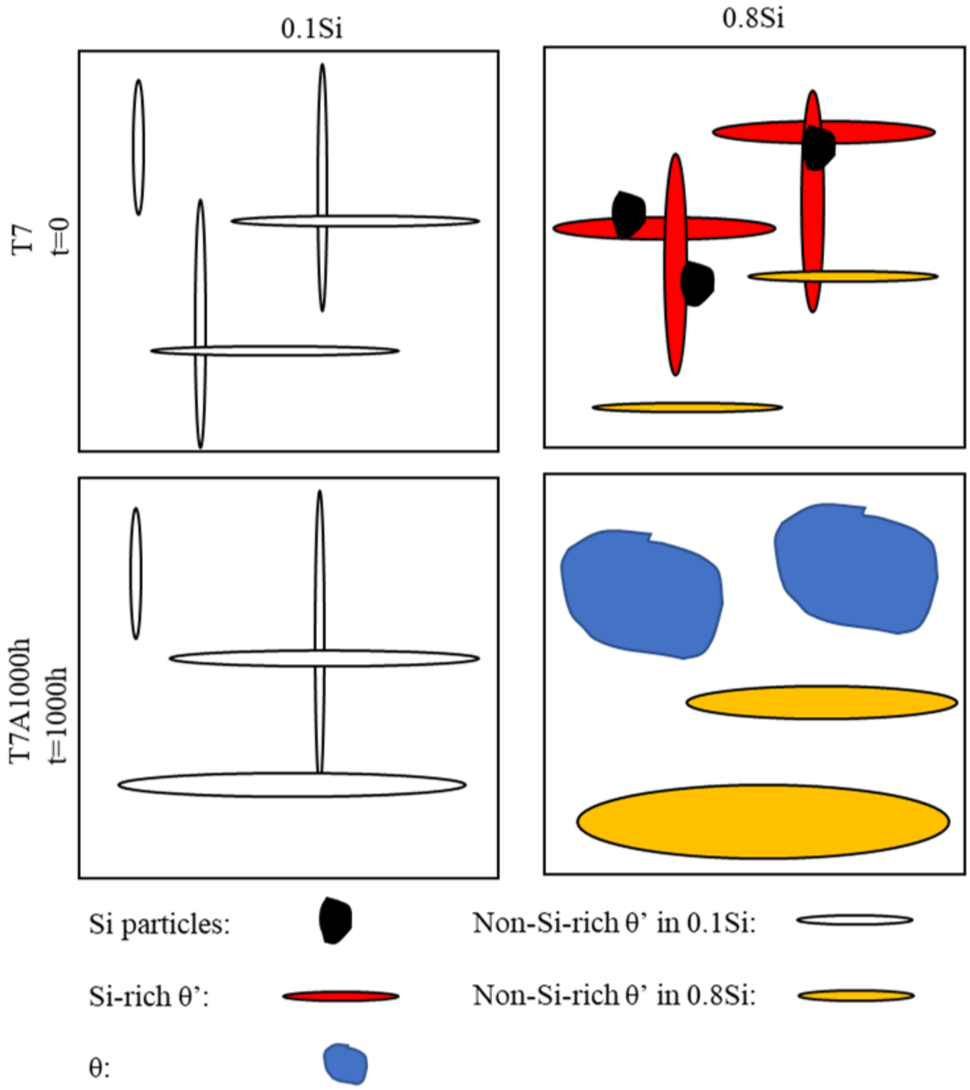

Figure 4.15 Schematic of proposed coarsening mechanism.

4.2.1.2 Strengthening mechanism

This part demonstrates the yield strength changes of experimental alloys with Si and thermal exposure contributed by different strengthening mechanisms. Generally, yield strength of polycrystalline alloys is linked to the grain boundary and the critical resolved shear stress of the grain[135]. It should be indicated that the experimental alloys do not display an evolution of deformation. Therefore, the yield strength can be approximately written as[135-137]:

$$\sigma_y = \sigma_0 + \sigma_{gb} + \sigma_{ss} + \sigma_p \tag{3}$$

Where σ_0 is the yield strength of aluminum matrix, which is around 34 MPa for pure aluminum 99.99%, σ_{gb} is the contribution of grain boundary strengthening, σ_{ss} is the contribution of solid solution strengthening and σ_p is the contribution of precipitates strengthening.

Precipitation strengthening is the main strengthening method in Al-Cu cast alloys, which is related to the size, type, number density, and volume fraction of precipitates. A strength model was implemented based on the parameters of strengthening precipitates.

On the basis of the coherence with α-Al matrix and its shearability, θ" is reported to contribute to the critical resolved shear stress(CRSS,) mainly through coherency strengthening and interfacial strengthening[138]. A recent study found that in 224 alloys, the interfacial strengthening effect of θ" precipitates is negligible compared to coherency strengthening[3]. The effective equation used to describe the coherency strengthening contribution of this shearable, plate-like precipitates is expressed by[138]:

$$\Delta\tau_{\theta''} = 4.1 \cdot G \left|\varepsilon^{\frac{3}{2}}\right| \cdot \left[\frac{f d_t}{2b}\right]^{\frac{1}{2}} \tag{4}$$

Where G is the shear modulus of α-Al matrix = 25.4 GPa, ε is the lattice strain = 0.006, b is the Burgers vector =0.284 nm, f is the volume fraction of precipitates, d_t is the true diameter of precipitates[38, 139].

For semi-coherent and non-shearable θ' precipitates, the contribution to CRSS can be explained by the Orowan looping mechanism[87] and the corresponding effective equation is given by[38]:

$$\Delta\tau_{\theta'} = \frac{Gb}{2\pi\sqrt{1-v}} \cdot \frac{1}{\frac{1.23 * 1.03}{\sqrt{N_v d_t}} - \frac{\pi d_t}{8} - 1.061 t_t} \cdot \ln\frac{\sqrt{d_t t_t}}{b} \tag{5}$$

Where v is the Poison ratio = 0.33 for face-centered cubic metals[38], Nv is the number density of precipitates, and other parameters are mentioned above.

To develop an overall CRSS contribution of these two types of precipitates, an equation is given by[121]:

$$\Delta\tau^{q} = (\Delta\tau_{\theta'})^{q} + (\Delta\tau_{\theta''})^{q} \tag{6}$$

Where is the combined CRSS contribution of θ” and θ’ precipitates, q is an exponent between 1 to 2. The value of q is determined by the strengths of obstacles. Here we used q=2 as both dislocations and precipitates have equal strengths with aging proceeding[140].

With the CRSS contribution, the yield strength increment due to precipitates can be obtained by[3]:

$$\sigma_p = M \cdot \Delta\tau \tag{7}$$

Where M is the Taylor factor =3.06[141].

The strength induced by solid solution strengthening can be described as[142]:

$$\sigma_{ss} = \sum_i k_i c_i \; (i = Cu) \tag{8}$$

Where c_i is the concentration of i solute (at%) and k_i is the scaling factor of i solute (k_{Cu}= 13.8 MPa/at%)[143]. Only the contribution of the main solute element Cu is calculated.

The concentration of Cu atoms in the matrix is considered as its solubility at 300 °C. The value is calculated by Thermal-Calc software.

The strength contributed by grain boundary strengthening is demonstrated by Hall-Patch relationship[144]:

$$\sigma_{gb} = k^{HP} d^{-\frac{1}{2}} \tag{9}$$

Where k^{HP}=0.042 MPa/m$^{-1/2}$[137] is the Hall-Patch constant and d is the average grain boundary of the alloys.

Based on the measured precipitates parameters, grain size and Cu concentration, the overall yield strength is calculated as predicted yield strength and presented with experimental results in Figure 4.16. It can be found that the calculated yield strength is very close to the experimental ones and follows the same tendence, confirming the feasibility of applied strengthening mechanisms for Al-Cu 224 alloys. The minor difference between them could be from the errors generated during the measurement of precipitates parameters. Based on the calculation, precipitates strengthening accounts for the largest proportion of the estimated yield strength. The values and experimental yield strength are highlighted in the figure.

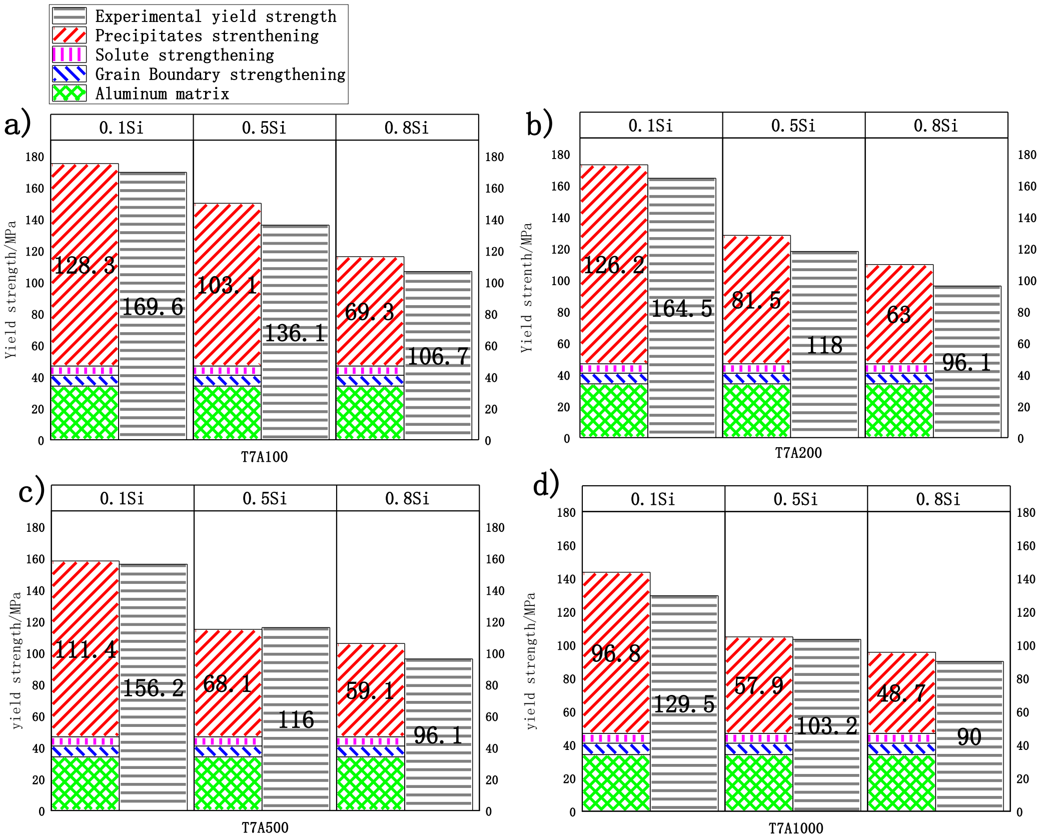

Figure 4.16 Calculated yield strength in comparison with experimental data: (a) T7A100, (b) T7A200, (c) T7A500 and (d) T7A1000.

4.3 Summary

In the present work, four different Al-Cu 224 type alloys with various Si additions are prepared to study the effect of Si on the evolution of microstructure and mechanical properties during the thermal exposure at 300 °C, the following conclusions are made based on the results:

1). High Si content Al-Cu 224 alloys have smaller θ’ precipitates size and smaller inter-precipitates spacing in T7 microstructure and display higher coarsening rates of θ’ precipitates during thermal exposure. A hypothesis is proposed to explain the coarsening behavior in this study that Si-rich θ’ precipitates might coarsen faster.

2). The addition of Si leads to a dramatic reduction of thermal stability and mechanical properties after thermal exposure at 300 °C (T7A conditions) with a significant drop of the number density and coarsening of θ’ precipitates.

3). Si has a dramatic negative effect on the creep resistance of experimental alloys. 0.8Si alloy exhibits the worst creep resistance among the alloys studied. However, Si particles are decomposed and small size α-dispersoids are formed during creep tests in 0.8Si alloy, slightly reducing the creep process.

CHAPTER 5 Influence of transition elements on the microstructure and properties during thermal exposure in high-Si 224 alloy

In this part, transition elements Zr, V, and Mn are added in high-Si 224 alloy to examine the possibility of enhancing its mechanical properties. In addition, a new 2-step heat-treatment is also applied.

Two alloys, one base alloy (alloy O) and one with the addition of transition elements (alloy F) are tested. The conventional T7 heat treatment (CHT) and a 2-steps heat-treatment are applied to the experimental alloys. The chemical compositions of two alloys as well as the heat treatment procedures are listed in the section 3.1.2 (Tables 3.2 and 3.3). To align with the former work in Chapter 4, samples after the 2-step heat treatment are also marked as “T7”. It follows the same annealing process at 300 °C up to 500 h, samples after annealing are marked as “T7A”. OM and TEM are used to reveal the microstructure, while compression yield strength tests are conducted to characterize the mechanical properties.

5.1 Evolution of microstructure

The typical microstructures of two alloys after two different heat treatments at T7 condition are demonstrated in Figure 5.1. It is composed of α-Al, primary Al_2Cu and α-Fe IMCs. Only a very small amount of Al_2Cu phase is observed in alloys subjected to CHT, which is mostly dissolved in the matrix, while a higher amount of Al_2Cu phase exists after 2-step heat treatment. This is because the CHT includes 10 h solution heat-treatment, but it is only 2 h solution treatment in 2-step heat treatment. Research has proved that 2 h of solution heat treatment was not enough to well dissolve Al_2Cu[51], which means in this case, 2-step heat treatment does not provide as much Cu atom concentration in the matrix as CHT. That leads to a lower number density of θ' precipitates, eventually lower yield strength at T7 condition.

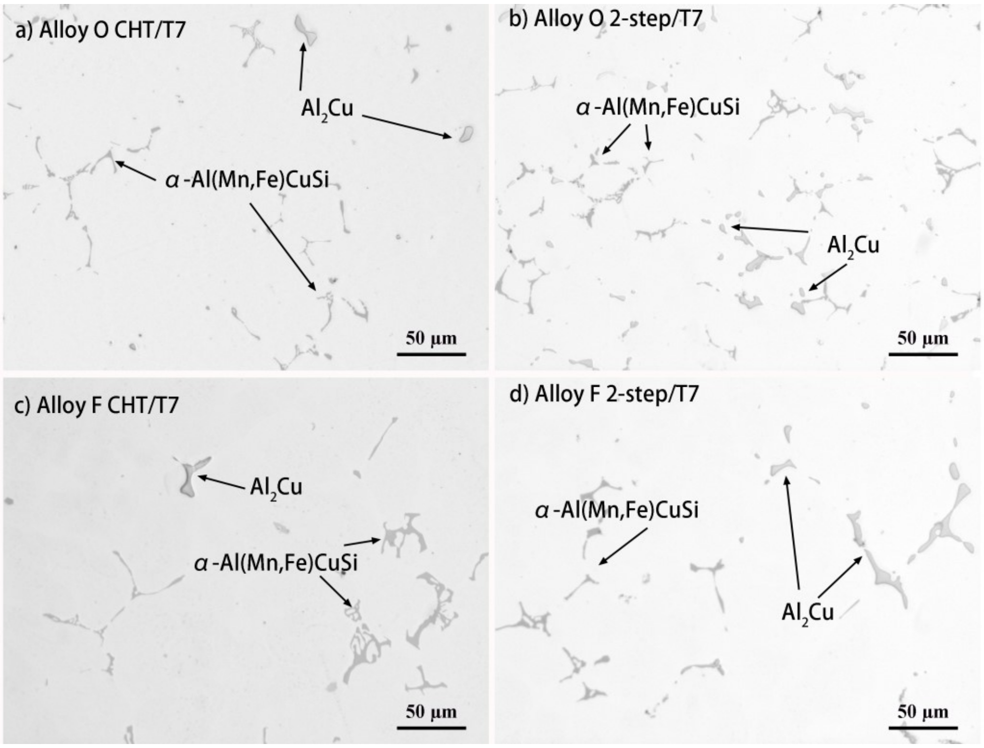

Figure 5.1 Typical microstructures of experimental alloys at T7 condition: a) Alloy O CHT/T7; b) Alloy O 2-step/T7; c) Alloy F CHT/T7; d) Alloy F 2-step/T7.

TEM is used to study the evolution of microstructures during heat treatments. Figure 5.2 shows the BF-TEM images of the experimental alloys after CHT at T7 and T7A100 conditions. As the base alloy, the microstructure of alloy O is the same as 0.5Si alloy in Chapter 4, which includes θ" and θ' precipitates at T7 condition and θ' precipitates and equilibrium θ at T7A100 condition. For alloy F, the addition of Zr and Mn also leads to the formation of α-dispersoids and Al_3Zr dispersoids. However, neither of these dispersoids distributes uniformly and they are not observed in the same area, therefore, each condition has two typical microstructures. Figure 5.2 b, c) shows the microstructure of alloy F after CHT at T7 condition. Comparing two different images, it is clear to see in the area where Al_3Zr dispersoids co-exist with θ” and θ’ precipitates, the length of θ” and θ’ precipitates is obviously shorter than where α-dispersoids exist. It is reported that Al_3Zr can facilitate the precipitation of θ” precipitates. The sandwich-like compact structure of Al_3Zr dispersoids and θ’ precipitates is observed, which aligns with literatures[12]. But near α-dispersoids, there is clearly a space between α-dispersoids and θ” or θ’ precipitates. Because α-dispersoids are formed before the precipitates during the heat treatment, and it consumes Cu atoms which are also the essential components of θ” or θ’ precipitates. The pre-existence of them restrains the precipitation of θ” precipitates. At T7A100 condition, θ’ precipitates in θ’ precipitates/Al_3Zr dispersoids co-existing area still maintain a fine size (shown in Figure 5.1 f)). For the θ’ precipitates in θ’ precipitates/α-dispersoids co-existing area, the reduction of number density is obvious, large size θ’ precipitates have transformed to equilibrium θ, but still some fine sized θ’ precipitates are observed.

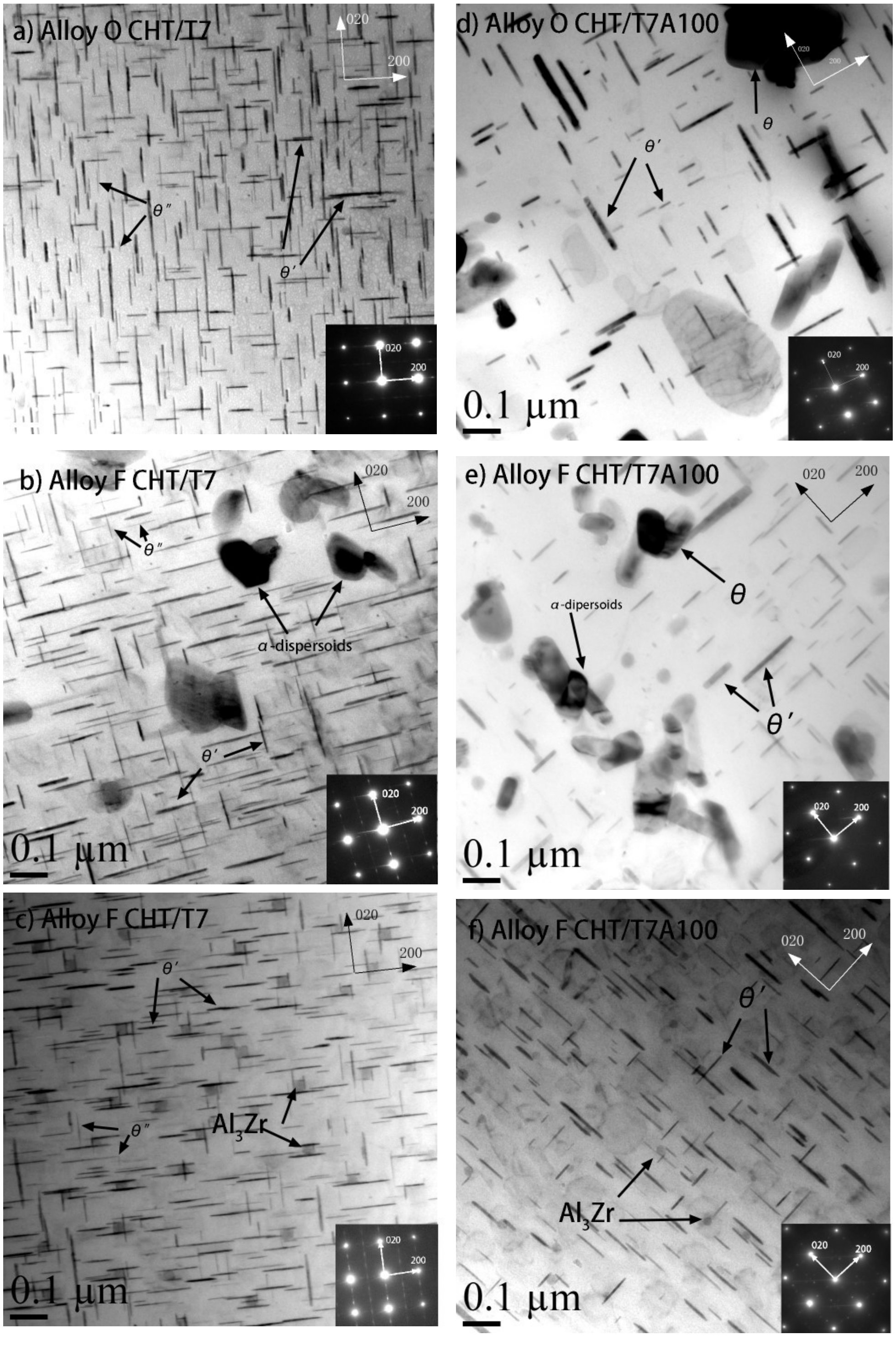

Figure 5.2 BF-TEM images and SAEDPs of experimental alloys at T7 and T7A conditions: a) Alloy O CHT/T7; b,c) Alloy F CHT/T7; d) Alloy O CHT/T7A100; e,f) Alloy F CHT/T7A100.

Figure 5.3 shows the BF-TEM images of alloy O after 2-step heat treatment at T7 and T7A100&500 conditions. 2-step heat treatment introduces more α-dispersoids in the structure and has less solution heat-treatment time. These two factors are unconducive to the θ” and θ’ precipitation and will further decrease the yield strength from the contribution of precipitation strengthening, which can explain why the yield strength of alloy O is low after 2-step heat treatment.

Figure 5.4 shows the BF-TEM images of alloy F after 2-step heat treatment at T7 and T7A100&500. More α-dispersoids are found in alloy F due to the higher content of Mn. The distribution of α-dispersoids is chain-like or random, but not uniform, making α-dispersoids/θ” and θ’ precipitates co-existing areas and α-dispersoids free area. Similar to CHT, the precipitation of Al_3Zr dispersoids occurs in α-dispersoids free areas, but their diameter is much finer than after CHT, because the solution heat-treatment time is too short for the dispersoids to coarsen. Figure 5.5 a) shows the Al_3Zr dispersoids/θ” and θ’ precipitates co-existing area at T7A100 condition under higher magnification to better reveal the microstructure. The sandwich-like compact structure is not observed, but the Al_3Zr dispersoids are denser than after CHT. During thermal exposure at 300 °C, the coarsening of θ’ precipitates is unavoidable, the evolution of the microstructure is demonstrated in Figure 5.4 b) and c). The microstructure varies significantly from area to area. 3 different zones are marked in Figure 5.4 c). In zone A, Al_3Zr dispersoids are not observed and many equilibrium θ precipitates are observed at an angle of 45 degrees with the θ’ precipitates. In Zone B, Al_3Zr dispersoids are observed with θ’ precipitates but without θ phases. A detailed TEM image of zone B is shown in Figure 5.5 b), comparing to T7 condition, Al_3Zr dispersoids show no tendency of coarsening during the thermal exposure at 300 °C up to 500 h. In zone C, only few small size θ’ precipitates are observed, and the dominant phase is α-dispersoids. Apparently, θ’ precipitates with presence of Al$_3$Zr dispersoids in zone B have better coarsening resistance than those without it in zone A.

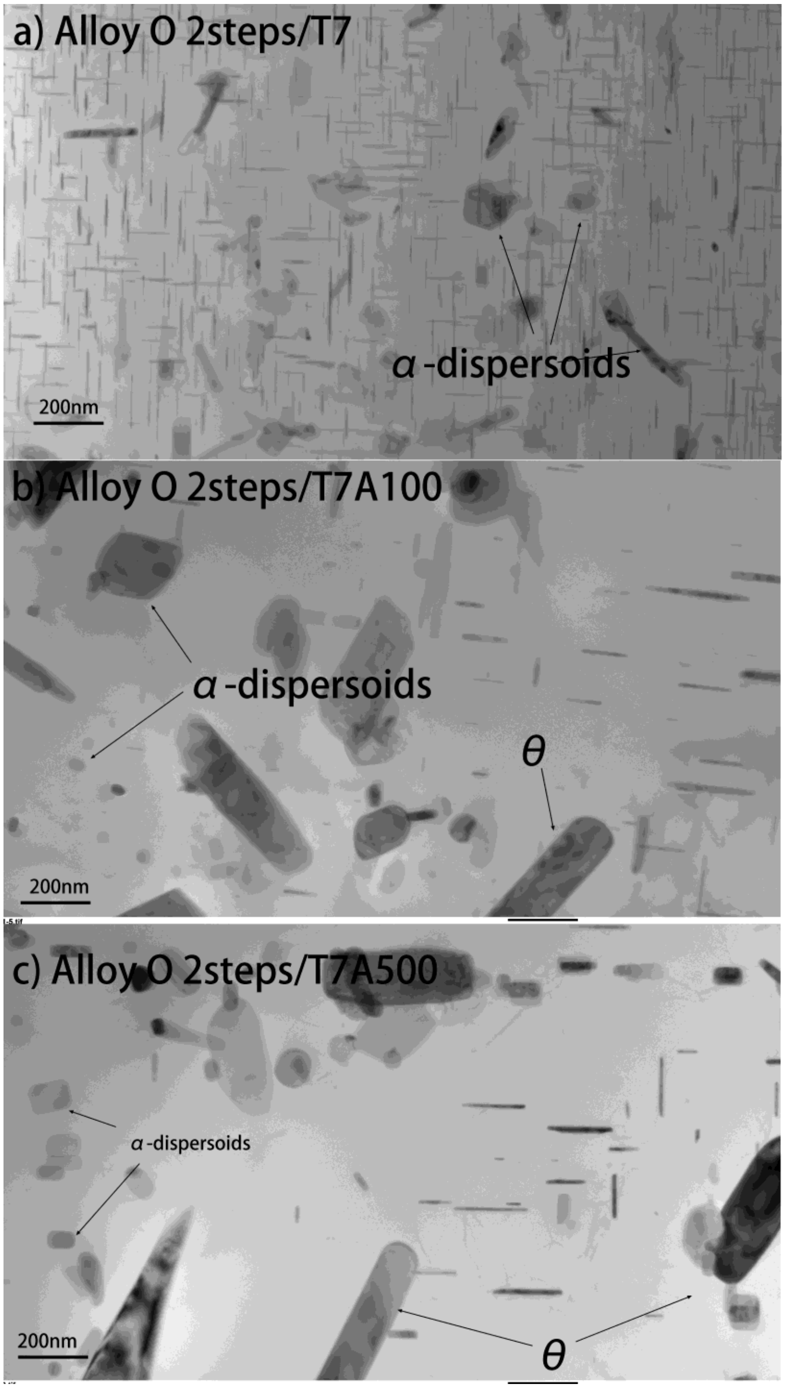

Figure 5.3 BF-TEM images of alloy O after 2-step heat treatment: a) at T7 condition; b) at T7A100 condition; c) at T7A500 condition.

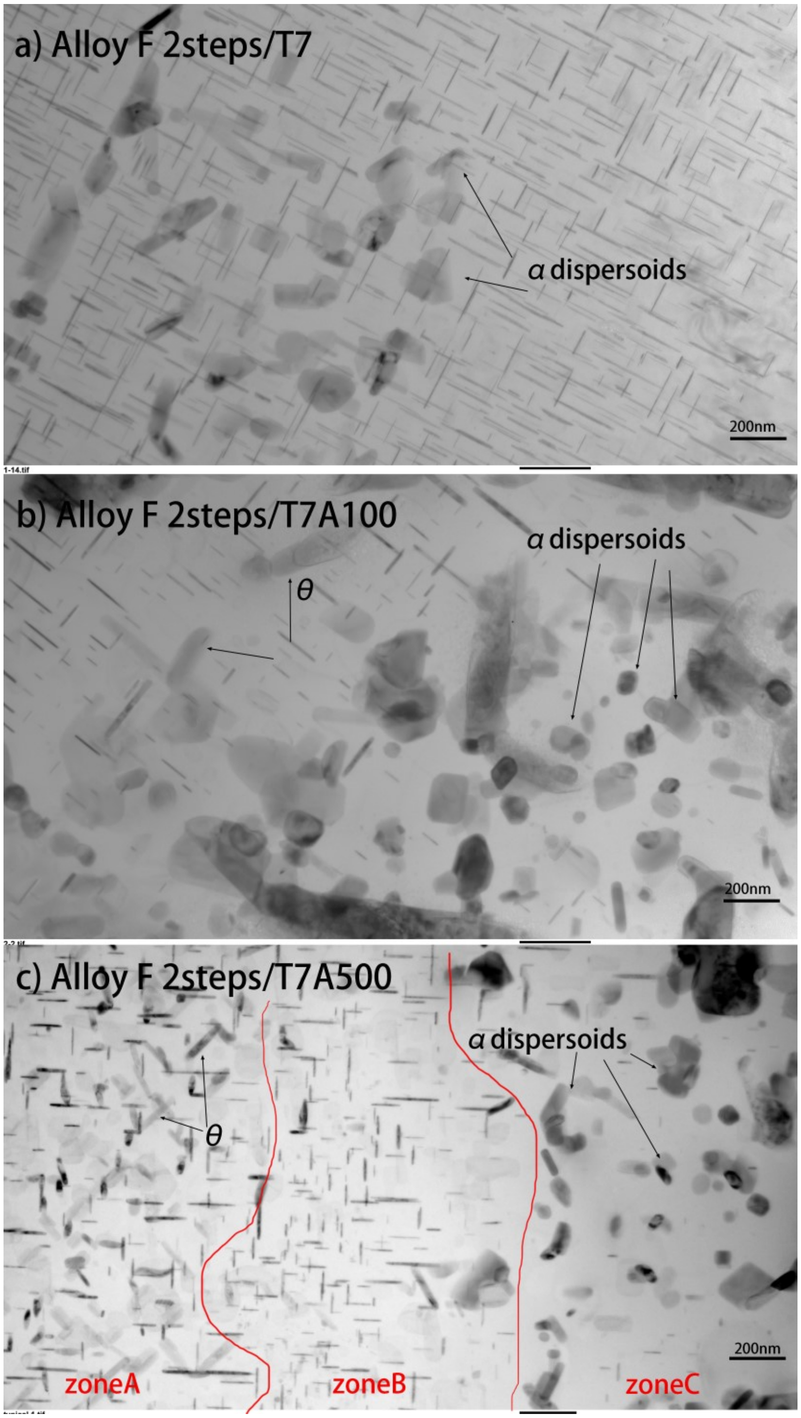

Figure 5.4 BF-TEM images of alloy F after 2-step heat-treatment: a) at T7 condition; b) at T7A100 condition; c) at T7A500 condition.

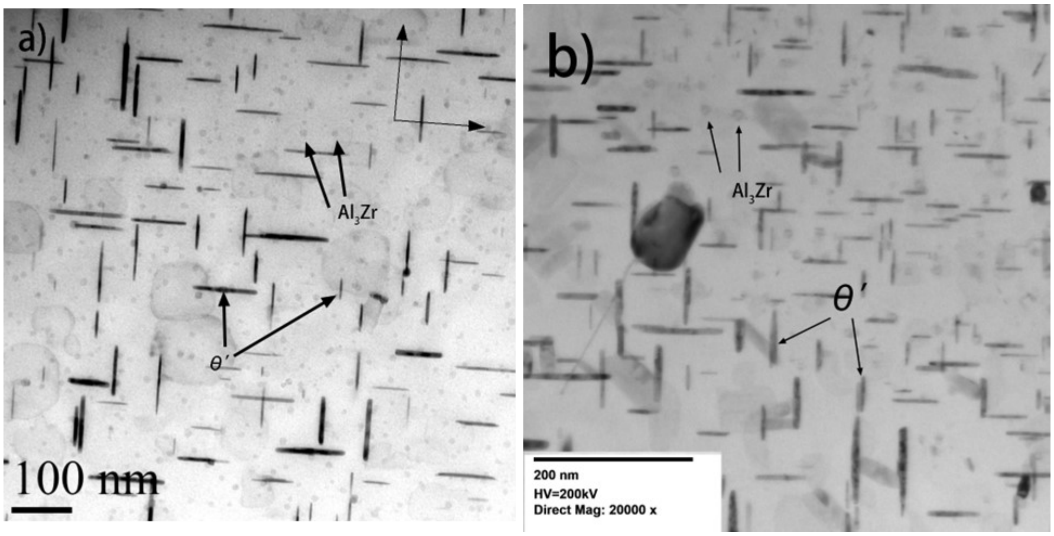

Figure 5.5 BF-TEM image of Al_3Zr/θ’ precipitates co-existing area in alloy F after 2-step heat treatment: a) at T7A100 condition; b) at T7A500 condition (zone B in figure 5.4 c))

5.2 Evolution of mechanical properties

The compression yield strengths are measured to characterize the mechanical properties of two experimental alloys. The test results are shown in Table 5.1. Under conventional heat treatment, alloy F shows a better yield strength (around 20 MPa higher than allot O) at T7A100&500 conditions, while at T7 condition, the yield strength of both alloys is similar. The same phenomenon is also observed under 2-step heat treatment. For the base alloy O, the 2-step heat treatment does not positively affect the mechanical properties. This is expected because of the insufficient solution treatment time. For alloy F, using 2-step heat-treatment does not increase the yield strength at T7 condition, but the improvements for T7A100&500 conditions are obvious.

Considering that the materials are designed to serve at elevated-temperatures, here we use the compression yield strength at T7A conditions at 300 ºC to represent their elevated-temperature properties. The order is: Alloy F+2-step heat treatment > Alloy F+CHT > Alloy O+CHT > Alloy O+2-step heat treatment.

Table 5.1 Compressive yield strength of two experimental alloy.

	Condition	**T7**		**T7A100**		**T7A500**	
	Temperature	**RT**	**300 °C**	**RT**	**300 °C**	**RT**	**300 °C**
CHT	**O**	**365.4±7.5**	**136.6±3.3**	**109.4±3.0**	**63.9±1.2**	**95.6±7.8**	**52.2±1.2**
	F	**366.6±9.6**	**146.2±1.4**	**137.6±2.2**	**81.0±1.7**	**122.2±0.3**	**75.9±2.5**
2-step heat treatment	**O**	**290.5±19.4**	**138.2±4.4**	**122.8±2.3**	**68.3±1.3**	**89.2±1.6**	**50.6±1.8**
	F	**313.4±13.9**	**134.6±5.5**	**151.7±11.3**	**81.2±1.4**	**135.1±6.8**	**76.7±2.4**

5.3 Summary

Transition elements, Zr, V and Mn are added in the 0.5Si alloy and a new 2-step heat treatment is applied to test the possibility for enhancing mechanical properties in high-Si (0.5 wt%) 224 alloys. In this part of work, it can be concluded:

1) The main benefit of the addition of transition elements is to increases the mechanical properties of 0.5Si alloy at T7A conditions (after thermal exposure for 100 h and 500 h). However, there no significant improvement at T7 condition. The newly designed 2-step heat treatment does not improve the mechanical properties of the base alloy, but it improves the in the alloy with Zr, V and Mn addition.

2) The addition of transition elements promotes the formation of α-dispersoids and Al_3Zr dispersoids. The 2-step heat treatment further promotes the precipitation of these two types of dispersoids, but their distribution is non-uniform, leading to the different local microstructures at T7A conditions.

CHAPTER 6 CONCLUSIONS

224 Al-Cu alloys with various Si content from 0.1 wt% to 0.8 wt% are well investigated in this study and the results are presented in Chapter 4. Transition element Zr, V and Mn are added in 0.5Si alloy and a 2-step heat-treatment is applied to enhance the high-temperature properties of high Si alloys, the results are presented in Chapter 5. From that we can get some conclusions:

1. Despite the positive effect on mechanical properties at T7 condition, the addition of Si significantly reduces the thermal stability and high-temperature properties of Al-Cu 224 alloys at T7A conditions.

2. A hypothesis regarding Si-rich θ' precipitates that might coarsen faster is proposed to explain the high coarsening rate of θ' precipitates in high Si alloys. The T7 microstructure of smaller θ' precipitates size and smaller inter-precipitates spacing in high Si content Al-Cu 224 alloys also plays an important role in the coarsening behavior in terms of that it results in shorter diffusion distance during thermal exposure.

3. Si also dramatically affects the creep behavior of Al-Cu 224 alloys. The creep resistance of Al-Cu 224 alloys becomes very poor after adding Si. But in 0.8Si alloy, Si particles are decomposed and small size α-dispersoids are formed during creep tests, slightly increasing the creep resistance.

4. The addition of transition elements Zr, V and high-level Mn and 2-step heat-treatment effectively improve yield strength of 0.5Si 224 alloys at T7A conditions by promoting α-dispersoids and Al_3M dispersoids which are both thermal stable at 300°C.

CHAPTER 7 RECOMMENDATIONS

1. In the present work, the effect of Si on 224 alloys is well investigated. It is proposed that Si can accelerate the coarsening of θ' precipitates during thermal exposure. High resolution TEM or atom probe tomography is suggested to provide detailed evidence of Si segregation at interface of α-Al matrix and θ' precipitates.

2. In the present work, we only tested one alloying method and one new treat treatment method with the addition of transition elements. The enhancement of mechanical properties in high-Si 224 alloy is not systematically studied, especially the contribution from thermally stable dispersoids. Therefore, quantifying the precipitates and dispersoids strength contribution as well as conducting creep tests and thermal mechanic fatigue are wishful to better characterize the elevated-temperature properties.

3. Different combination of transition elements and optimized the 2-step heat treatment are accordingly suggested to obtain the uniform distribution of dispersoids and to acquire better mechanical properties at elevated temperatures.

REFERENCES

1. Shin, D., Shyam, A., Lee, S., Yamamoto, Y., and Haynes, J.A., *Solute segregation at the Al/θ'-Al2Cu interface in Al-Cu alloys.* Acta Materialia, 2017. **141**: p. 327-340.

2. Javidani, M. and Larouche, D., *Application of cast Al–Si alloys in internal combustion engine components.* International Materials Reviews, 2014. **59**(3): p. 132-158.

3. Rakhmonov, J., Liu, K., Pan, L., Breton, F., and Chen, X.G., *Enhanced mechanical properties of high-temperature-resistant Al–Cu cast alloy by microalloying with Mg.* Journal of Alloys and Compounds, 2020. **827:** 154305.

4. Kent, D., Schaffer, G.B., and Drennan, J., *Age hardening of a sintered Al–Cu–Mg–Si–(Sn) alloy.* Materials Science and Engineering: A, 2005. **405**(1): p. 65-73.

5. Hutchinson, C.R. and Ringer, S.P., *Precipitation processes in Al-Cu-Mg alloys microalloyed with Si.* Metallurgical and Materials Transactions A, 2000. **31**(11): p. 2721-2733.

6. Hornbogen, E., *Hundred years of precipitation hardening.* Journal of Light Metals, 2001. **1**(2): p. 127-132.

7. Biswas, A., Siegel, D.J., Wolverton, C., and Seidman, D.N., *Precipitates in Al–Cu alloys revisited: Atom-probe tomographic experiments and first-principles calculations of compositional evolution and interfacial segregation.* Acta Materialia, 2011. **59**(15): p. 6187-6204.

8. Zhang, D., Peng, J., and Liu, T., *The fast diffusion paths of copper atoms in Al–Cu–Si alloys.* Materials Science and Engineering: A, 2006. **425**(1): p. 78-82.

9. Gao, Y.H., Yang, C., Zhang, J.Y., Cao, L.F., Liu, G., Sun, J., and Ma, E., *Stabilizing nanoprecipitates in Al-Cu alloys for creep resistance at 300°C.* Materials Research Letters, 2018. **7**(1): p. 18-25.

10. Shyam, A., Plotkowski, A., Bahl, S., Sisco, K., Allard, L.F., Yang, Y., Haynes, J.A., and Dehoff, R.R., *An additively manufactured AlCuMnZr alloy microstructure and tensile mechanical properties.* Materialia, 2020. **12**: 100758.

11. Samuel, E., Nabawy, A.M., Samuel, A.M., Doty, H.W., Songmene, V., and Samuel, F.H., *Effect of Zr and Ti Addition and Aging Treatment on the Microstructure and Tensile Properties of Al-2%Cu-Based Alloys.* Materials (Basel), 2022. **15**(13): 4511.

12. Li, D., Liu, K., Rakhmonov, J., and Chen, X.G., *Enhanced thermal stability of precipitates and elevated-temperature properties via microalloying with transition metals (Zr, V and Sc) in Al–Cu 224 cast alloys.* Materials Science and Engineering: A, 2021. **827**: 142090.

13. Jia, M., Zheng, Z., and Luo, X., *Influence of AlCuSc Ternary Phase on the Microstructure and Properties of 1469 Alloy.* Materials Science Forum, 2014. **794-796**: p. 1057-1062.

14. Fuller, C.B. and Seidman, D.N., *Temporal evolution of the nanostructure of Al(Sc,Zr) alloys: Part II-coarsening of Al3(Sc1−xZrx) precipitates.* Acta Materialia, 2005. **53**(20): p. 5415-5428.

15. Agrawal, P., Gupta, S., Thapliyal, S., Shukla, S., Haridas, R.S., and Mishra, R.S., *Additively manufactured novel Al-Cu-Sc-Zr alloy: Microstructure and mechanical properties.* Additive Manufacturing, 2021. **37**: 101623.

16. Gao, T., Ceguerra, A., Breen, A., Liu, X., Wu, Y., and Ringer, S., *Precipitation behaviors of cubic and tetragonal Zr–rich phase in Al–(Si–)Zr alloys.* Journal of Alloys and Compounds, 2016. **674**: p. 125-130.

17. Rahimian, M., Amirkhanlou, S., Blake, P., and Ji, S., *Nanoscale Zr-containing precipitates; a solution for significant improvement of high-temperature strength in Al-Si-Cu-Mg alloys.* Materials Science and Engineering A, 2018. **721**: p. 328-338.

18. Poplawsky, J.D., Milligan, B.K., Allard, L.F., Shin, D., Shower, P., Chisholm, M.F., and Shyam, A., *The synergistic role of Mn and Zr/Ti in producing θ'/L12 co-precipitates in Al-Cu alloys.* Acta Materialia, 2020. **194**: p. 577-586.

19. Shyam, A., Roy, S., Shin, D., Poplawsky, J.D., Allard, L.F., Yamamoto, Y., Morris, J.R., Mazumder, B., Idrobo, J.C., Rodriguez, A., Watkins, T.R., and Haynes, J.A., *Elevated temperature microstructural stability in cast AlCuMnZr alloys through solute segregation.* Materials Science and Engineering: A, 2019. **765**.

20. Polmear, I.J., *4 - Cast aluminium alloys*, in *Light Alloys (Fourth Edition)*, I.J. Polmear, Editor. 2005, Butterworth-Heinemann: Oxford. p. 205-235.

21. Runge, J.M., *A Brief History of Aluminum and Its Alloys*, in *The Metallurgy of Anodizing Aluminum: Connecting Science to Practice*, J.M. Runge, Editor. 2018, Springer International Publishing: Cham. p. 1-63.

22. Altenpohl, D., Kaufman, J.G., and Das, K. *Aluminum : technology, applications, and environment : a profile of modern metal : aluminum from within*. 1998.

23. Polmear, I.J. *Aluminium Alloys - A Century of Age Hardening*. 2004.

24. Campbell, F.C., *Chapter 2 - Aluminum*, in *Manufacturing Technology for Aerospace Structural Materials*, F.C. Campbell, Editor. 2006, Elsevier Science: Oxford. p. 15-92.

25. Rakhmonov, J., Liu, K., and Chen, G.X., *Effects of Compositional Variation on the Thermal Stability of $$\theta$$'-Al2Cu Precipitates and Elevated-Temperature Strengths in Al-Cu 206 Alloys.* Journal of Materials Engineering and Performance, 2020. **29**(11): p. 7221-7230.

26. Shin, D., Lee, S., Shyam, A., and Haynes, J.A., *Petascale supercomputing to accelerate the design of high-temperature alloys.* Sci Technol Adv Mater, 2017. **18**(1): p. 828-838.

27. Knipling, K., Dunand, D., and Seidman, D., *Criteria for developing castable, creep-resistant aluminum-based alloys – A review.* Zeitschrift für Metallkunde, 2006. **97**: p. 246-265.

28. Wolverton, C., *Solute–vacancy binding in aluminum.* Acta Materialia, 2007. **55**(17): p. 5867-5872.

29. Sankaran, R. and Laird, C., *Effect of trace additions Cd, In and Sn on the interfacial structure and kinetics of growth of θ' plates in Al Cu alloy.* Materials Science and Engineering, 1974. **14**(3): p. 271-279.

30. Ringer, S.P., Hono, K., and Sakurai, T., *The effect of trace additions of sn on precipitation in Al-Cu alloys: An atom probe field ion microscopy study.* Metallurgical and Materials Transactions A, 1995. **26**(9): p. 2207-2217.

31. Ringer, S.P. and Hono, K., *Microstructural Evolution and Age Hardening in Aluminium Alloys: Atom Probe Field-Ion Microscopy and Transmission Electron Microscopy Studies.* Materials Characterization, 2000. **44**(1): p. 101-131.

32. Kroupa, A., Zobač, O., and Richter, K.W., *The thermodynamic reassessment of the binary Al–Cu system.* Journal of Materials Science, 2021. **56**(4): p. 3430-3443.

33. Kelly, A. and Nicholson, R., *Progress in Materials Science.* Pergamon Press, 1963. **10**(149): p. 312-315.

34. Hardy, H. and Heal, T., *Report on precipitation.* Progress in metal physics, 1954. **5**: p. 143-278.

35. Höno, K., Satoh, T., and Hirano, K.-I., *Evidence of multi-layer GP zones in Al-1·7at.%,Cu alloy.* Philosophical Magazine A, 1986. **53**(4): p. 495-504.

36. Zuiko, I. and Kaibyshev, R., *Aging behavior of an Al–Cu–Mg alloy.* Journal of Alloys and Compounds, 2018. **759**: p. 108-119.

37. Polmear, I.J., *2 - Physical metallurgy of aluminium alloys*, in *Light Alloys (Fourth Edition)*, I.J. Polmear, Editor. 2005, Butterworth-Heinemann: Oxford. p. 29-96.

38. Roy, S., Allard, L.F., Rodriguez, A., Porter, W.D., and Shyam, A., *Comparative Evaluation of Cast Aluminum Alloys for Automotive Cylinder Heads: Part II—Mechanical and Thermal Properties.* Metallurgical and Materials Transactions A, 2017. **48**(5): p. 2543-2562.

39. Silcock, J., Heal, T., and Hardy, H., *Structural ageing characteristics of binary aluminium-copper alloys.* J. Inst. Metals, 1954. **82**: 239-248.

40. Shen, Z., Ding, Q., Liu, C., Wang, J., Tian, H., Li, J., and Zhang, Z., *Atomic-scale mechanism of the $\theta''\rightarrow\theta'$ phase transformation in Al-Cu alloys.* Journal of Materials Science & Technology, 2017. **33**(10): p. 1159-1164.

41. *4 - Strengthening of metal alloys*, in *Introduction to Aerospace Materials*, A.P. Mouritz, Editor. 2012, Woodhead Publishing. p. 57-90.

42. Kaira, C.S., De Andrade, V., Singh, S.S., Kantzos, C., Kirubanandham, A., De Carlo, F., and Chawla, N., *Probing Novel Microstructural Evolution Mechanisms in Aluminum Alloys Using 4D Nanoscale Characterization.* Advanced Materials, 2017. **29**(41): 1703482.

43. Merle, P. and Fouquet, F., *Coarsening of θ′ plates in al-cu alloys—I. experimental determination of mechanisms.* Acta Metallurgica, 1981. **29**(12): p. 1919-1927.

44. Shower, P., Morris, J., Shin, D., Allard, L., Radhakrishnan, B., and Shyam, A., *Onset of Θ′ to Θ Phase Transformation in Al-Cu Alloys.* SSRN Electronic Journal, 2019.

45. Zhang, W.-w., Zhao, Y.-l., Zhang, D.-t., Luo, Z.-q., Yang, C., and Li, Y.-y., *Effect of Si addition and applied pressure on microstructure and tensile properties of as-cast Al-5.0Cu-0.6Mn-1.2Fe alloys.* Transactions of Nonferrous Metals Society of China, 2018. **28**(6): p. 1061-1072.

46. Liu, K., Cao, X., and Chen, X.G., *Effect of Mn, Si, and Cooling Rate on the Formation of Iron-Rich Intermetallics in 206 Al-Cu Cast Alloys.* Metallurgical and Materials Transactions B, 2012. **43**(5): p. 1231-1240.

47. Liu, K., Cao, X., and Chen, X.G., *Formation and Phase Selection of Iron-Rich Intermetallics in Al-4.6Cu-0.5Fe Cast Alloys.* Metallurgical and Materials Transactions A, 2013. **44**(2): p. 682-695.

48. Tseng, C.-J., Lee, S.-L., Tsai, S.-C., and Cheng, C.-J., *Effects of manganese on microstructure and mechanical properties of A206 alloys containing iron.* Journal of Materials Research, 2002. **17**(9): p. 2243-2250.

49. Liu, K., Cao, X., and Chen, X.G., *A New Iron-Rich Intermetallic-AlmFe Phase in Al-4.6Cu-0.5Fe Cast Alloy.* Metallurgical and Materials Transactions A, 2012. **43**(4): p. 1097-1101.

50. Kamguo Kamga, H., Larouche, D., Bournane, M., and Rahem, A., *Solidification of aluminum-copper B206 alloys with iron and silicon additions.* Metallurgical and Materials Transactions A, 2010. **41**(11): p. 2844-2855.

51. Liu, K., Cao, X., and Chen, X.G., *Solid-State Transformation of Iron-Rich Intermetallic Phases in Al-Cu 206 Cast Alloys During Solution Heat Treatment.* Metallurgical and Materials Transactions A, 2013. **44**(8): p. 3494-3503.

52. Mitlin, D., Morris, J.W., and Radmilovic, V., *Catalyzed precipitation in Al-Cu-Si.* Metallurgical and Materials Transactions A, 2000. **31**(11): p. 2697-2711.

53. Doherty, R.D., *CHAPTER 15 - DIFFUSIVE PHASE TRANSFORMATIONS IN THE SOLID STATE*, in *Physical Metallurgy (Fourth Edition)*, R.W. Cahn and P. Haasen†, Editors. 1996, North-Holland: Oxford. p. 1363-1505.

54. Hornbogen, E., *Hundred years of precipitation hardening.* Journal of Light Metals, 2001. **1**: p. 127-132.

55. Thomas, G. and Whelan, M.J., *Observations of precipitation in thin foils of aluminium +4% copper alloy.* The Philosophical Magazine: A Journal of Theoretical Experimental and Applied Physics, 1961. **6**(69): p. 1103-1114.

56. Bonfield, W. and Datta, P.K., *Zone formation during room temperature ageing of Al-4% Cu-0.8% Si-0.8% Mg.* Journal of Materials Science, 1977. **12**(5): p. 1050-1052.

57. Shower, P., Poplawsky, J., Bahl, S., and Shyam, A., *The role of Si in determining the stability of the θ' precipitate in Al-Cu-Mn-Zr alloys.* Journal of Alloys and Compounds, 2021. **862:** 15815.

58. Knipling, K., *Precipitation in Highly Supersaturated Al-Sc-V, Al-Sc-Nb, and Al-Sc-Ta Alloys During Isochronal Aging.* Microscopy and Microanalysis, 2015. **21**: p. 359-360.

59. Knipling, K.E., Dunand, D.C., and Seidman, D.N., *Criteria for developing castable, creep-resistant aluminum-based alloys – A review.* International Journal of Materials Research, 2006. **97**(3): p. 246-265.

60. Zhu, S., Yao, J.-Y., Sweet, L., Easton, M., Taylor, J., Robinson, P., and Parson, N., *Influences of Nickel and Vanadium Impurities on Microstructure of Aluminum Alloys.* JOM, 2013. **65**(5): p. 584-592.

61. Kazakova, E. and Rusnyak, Y.I., *A study of rapidly hardened aluminum alloys with iron and vanadium.* Metal Science and Heat Treatment, 2009. **51**(9): p. 436-439.

62. Lai, J., Shi, C., and Chen, X.G., *Effects of V addition on recrystallization resistance of 7150 aluminum alloy after simulative hot deformation.* Materials Characterization, 2014. **96**: p. 126-134.

63. Wang, X., Cong, F., Zhu, Q., and Cui, J., *Effect of trace element vanadium on superplasticity of 5083 aluminium alloy sheets.* Science China Technological Sciences, 2012. **55**(2): p. 510-514.

64. Camero, S., Puchi, E.S., and Gonzalez, G., *Effect of 0.1% vanadium addition on precipitation behavior and mechanical properties of Al-6063 commercial alloy.* Journal of Materials Science, 2006. **41**(22): p. 7361-7373.

65. Lech-Grega, M., Szymański, W., Boczkal, S., Gawlik, M., and Bigaj, M., *The effect of vanadium addition on structure and material properties of heat treated 6xxx series aluminium alloys*, in *Light Metals 2015*. 2015, Springer. p. 173-178.

66. Cui, Q., Itoh, G., Kanno, M., Tsuji, Y., and Kobayashi, K., *Effects of vanadium and chromium addition on S'-phase precipitation in a 2901 aluminium alloy.* Nippon Kinzoku Gakkaishi (1952), 1995. **59**(3): p. 251-257.

67. Fan, Y. and Makhlouf, M.M., *Precipitation strengthening in aluminum-zirconium-vanadium alloys.* Journal of Alloys and Compounds, 2017. **725**: p. 171-180.

68. Liu, K., Cao, X., and Chen, X.G., *Precipitation of iron-rich intermetallic phases in Al-4.6Cu-0.5Fe-0.5Mn cast alloy.* Journal of Materials Science, 2012. **47**(10): p. 4290-4298.

69. Liu, K., Cao, X., and Chen, X.G., *A new iron-rich intermetallic-Al mFe phase in Al-4.6Cu-0.5Fe cast alloy.* Metallurgical and Materials Transactions A, 2012. **43** p. 1097-1101.

70. Lin, B., Zhang, W., Zhao, Y., and Li, Y., *Solid-state transformation of Fe-rich intermetallic phases in Al–5.0Cu–0.6Mn squeeze cast alloy with variable Fe contents during solution heat treatment.* Materials Characterization, 2015. **104**: p. 124-131.

71. Zhang, W., Lin, B., Zhang, D., and Li, Y., *Microstructures and mechanical properties of squeeze cast Al–5.0Cu–0.6Mn alloys with different Fe content.* Materials & Design (1980-2015), 2013. **52**: p. 225-233.

72. Lin, B., Zhang, W., Lou, Z., Zhang, D., and Li, Y., *Comparative study on microstructures and mechanical properties of the heat-treated Al–5.0Cu–0.6Mn–xFe alloys prepared by gravity die casting and squeeze casting.* Materials & Design, 2014. **59**: p. 10-18.

73. Kamga, H.K., Larouche, D., Bournane, M., and Rahem, A., *Mechanical properties of aluminium–copper B206 alloys with iron and silicon additions.* International Journal of Cast Metals Research, 2012. **25**(1): p. 15-25.

74. Zhang, W.-w., Lin, B., Cheng, P., Zhang, D.-t., and Li, Y.-y., *Effects of Mn content on microstructures and mechanical properties of Al-5.0Cu-0.5Fe alloys prepared by squeeze casting.* Transactions of Nonferrous Metals Society of China, 2013. **23**(6): p. 1525-1531.

75. Muggerud, A.M.F., Li, Y.J., and Holmestad, R., *Orientation studies of á-Al(Fe,Mn)Si dispersoids in 3xxx Al alloys*, in *14th International Conference on Aluminium Alloys, ICAA 2014*. 2014, Trans Tech Publications Ltd: Trondheim. p. 39-44.

76. Zhang, W., Lin, B., Fan, J., Zhang, D., and Li, Y., *Microstructures and mechanical properties of heat-treated Al–5.0Cu–0.5Fe squeeze cast alloys with different Mn/Fe ratio.* Materials Science and Engineering: A, 2013. **588**: p. 366-375.

77. Hwang, J.Y., Doty, H., and Kaufman, M., *The effects of Mn additions on the microstructure and mechanical properties of Al–Si–Cu casting alloys.* Materials Science and Engineering: A, 2008. **488**: p. 496–504.

78. Li, Y.J. and Arnberg, L., *Quantitative study on the precipitation behavior of dispersoids in DC-cast AA3003 alloy during heating and homogenization.* Acta Materialia, 2003. **51**(12): p. 3415-3428.

79. Li, Z., Zhang, Z., and Chen, X.-G., *The Influence of Cu Addition on Dispersoid Formation and Mechanical Properties of Al-Mn-Mg 3004 Alloy.* Metals, 2018. **8**(3): 155.

80. Moon, K.I., Kim, S.C., and Lee, K.S., *A study on the microstructure of D023 Al3Zr and L12 (Al+12.5 at.% Cu)3Zr intermetallic compounds synthesized by PBM and SPS.* Intermetallics, 2002. **10**(2): p. 185-194.

81. Chang, W.-S. and Muddle, B.C., *Trialuminide intermetallic alloys for elevated temperature applications—overview.* Metals and Materials, 1997. **3**(1): p. 1-15.

82. Knipling, K.E., Dunand, D.C., and Seidman, D.N., *Nucleation and precipitation strengthening in dilute Al-Ti and Al-Zr alloys.* Metallurgical and Materials Transactions A, 2007. **38**(10): p. 2552-2563.

83. Knipling, K.E., Dunand, D.C., and Seidman, D.N., *Precipitation evolution in Al–Zr and Al–Zr–Ti alloys during isothermal aging at 375–425°C.* Acta Materialia, 2008. **56**(1): p. 114-127.

84. Nie, J.F. and Muddle, B.C., *Strengthening of an Al–Cu–Sn alloy by deformation-resistant precipitate plates.* Acta Materialia, 2008. **56**(14): p. 3490-3501.

85. Yang, C., Zhang, P., Shao, D., Wang, R.H., Cao, L.F., Zhang, J.Y., Liu, G., Chen, B.A., and Sun, J., *The influence of Sc solute partitioning on the microalloying effect and mechanical properties of Al-Cu alloys with minor Sc addition.* Acta Materialia, 2016. **119**: p. 68-79.

86. Li, Z., Zhang, Z., and Chen, X.G., *Improvement in the mechanical properties and creep resistance of Al-Mn-Mg 3004 alloy with Sc and Zr addition.* Materials Science and Engineering: A, 2018. **729**: p. 196-207.

87. Mondol, S., Makineni, S.K., Kumar, S., and Chattopadhyay, K., *Enhancement of High Temperature Strength of 2219 Alloys Through Small Additions of Nb and Zr and a Novel Heat Treatment.* Metallurgical and Materials Transactions A, 2018. **49**(7): p. 3047-3057.

88. Kanno, M. and Ou, B.-L., *Heterogeneous Precipitation of Intermediate Phases on Al3Zr Particles in Al–Cu–Zr and Al–Li–Cu–Zr Alloys.* Materials Transactions, JIM, 1991. **32**(5): p. 445-450.

89. Chen, B., Pan, L., Wang, R., Liu, G., Cheng, P., Xiao, L., and Sun, J., *Effect of solution treatment on precipitation behaviors and age hardening response of Al–Cu alloys with Sc addition.* Materials Science and Engineering: A, 2011. **530**: p. 607-617.

90. Kumar Makineni, S., Sugathan, S., Meher, S., Banerjee, R., Bhattacharya, S., Kumar, S., and Chattopadhyay, K., *Enhancing elevated temperature strength of copper containing aluminium alloys by forming L12 Al3Zr precipitates and nucleating θ" precipitates on them.* Scientific Reports, 2017. **7**(1): 11154.

91. Robson, J., *A new model for prediction of dispersoid precipitation in aluminium alloys containing zirconium and scandium.* Acta Materialia, 2004. **52**(6): p. 1409-1421.

92. Fuller, C.B., Seidman, D.N., and Dunand, D.C., *Mechanical properties of Al (Sc, Zr) alloys at ambient and elevated temperatures.* Acta materialia, 2003. **51**(16): p. 4803-4814.

93. Davydov, V.G., Elagin, V.I., Zakharov, V.V., and Rostoval, D., *Alloying aluminum alloys with scandium and zirconium additives.* Metal Science and Heat Treatment, 1996. **38**(8): p. 347-352.

94. Fuller, C.B., Murray, J.L., and Seidman, D.N., *Temporal evolution of the nanostructure of Al(Sc,Zr) alloys: Part I – Chemical compositions of Al3(Sc1−xZrx) precipitates.* Acta Materialia, 2005. **53**(20): p. 5401-5413.

95. Clouet, E., Laé, L., Épicier, T., Lefebvre, W., Nastar, M., and Deschamps, A., *Complex precipitation pathways in multicomponent alloys.* Nature Materials, 2006. **5**(6): p. 482-488.

96. Dorin, T., Ramajayam, M., Lamb, J., and Langan, T., *Effect of Sc and Zr additions on the microstructure/strength of Al-Cu binary alloys.* Materials Science and Engineering: A, 2017. **707**: p. 58-64.

97. Zhang, J., Zhao, H., Zhu, J., Wang, B., and Yi, D., *Relationship between electrical resistivity and Al3(Zr,Sc) core–shell dispersoids of Al–Zr–Sc electrical transmission cable: Modeling and experimental results.* Electric Power Systems Research, 2019. **168**: p. 1-7.

98. Ratke, L. and Voorhees, P.W., *Nucleation, Growth and Coarsening*, in *Growth and Coarsening: Ostwald Ripening in Material Processing*, L. Ratke and P.W. Voorhees, Editors. 2002, Springer Berlin Heidelberg: Berlin, Heidelberg. p. 205-224.

99. *Statistical Theories of Phase Transitions*, in *Phase Transformations in Materials*. 2001. **4**: p. 239-308.

100. Khan, I.N., Starink, M., and Yan, J., *A model for precipitation kinetics and hardening in Al-Cu-Mg alloys.* Materials Science and Engineering A, 2008. **472**: p.66-74.

101. Du, Q., Poole, W., and Wells, M., *A mathematical model coupled to CALPHAD to predict precipitation kinetics for multicomponent aluminum alloys.* Acta Materialia, 2012. **60**(9): p. 3830-3839.

102. Russell, K.C. and Aaronson, H.I., *Sequences of precipitate nucleation.* Journal of Materials Science, 1975. **10**(11): p. 1991-1999.

103. Cahn, J.W., *Nucleation on dislocations.* Acta Metallurgica, 1957. **5**(3): p. 169-172.

104. Dollins, C., *Nucleation on dislocations.* Acta Metallurgica, 1970. **18**(11): p. 1209-1215.

105. Hornbogen, E. and Roth, M., *Die verteilung kohärenter teilchen in nickellegierungen.* International Journal of Materials Research, 1967. **58**(12): p. 842-855.

106. Hornbogen, E., *INVESTIGATION BY MEANS OF THE ELECTRON MICROSCOPE OF PRECIPITATION IN AL-CU SOLID SOLUTIONS. PT. 4. PRECIPITATION IN DEFORMED AL PLUS 1. 3 AT. PER CENT--3 WT. PER CENT-- CU-SOLID SOLUTIONS.* ALUMINUM, 1967. **43**(3): p. 166-170.

107. Laird, C. and Aaronson, H., *Mechanisms of formation of θ and dissolution of θ' precipitates in an Al-4% Cu alloy.* Acta Metallurgica, 1966. **14**(2): p. 171-185.

108. Vaithyanathan, V., Wolverton, C., and Chen, L.Q., *Multiscale modeling of θ' precipitation in Al–Cu binary alloys.* Acta Materialia, 2004. **52**(10): p. 2973-2987.

109. Boyd, J.D. and Nicholson, R.B., *The coarsening behaviour of θ'' and θ' precipitates in two Al-Cu alloys.* Acta Metallurgica, 1971. **19**(12): p. 1379-1391.

110. Nembach, E., *Coarsening of precipitates during step-wise and continuous temperature sweeps.* Materials Science and Engineering: A, 2008. **496**(1): p. 530-532.

111. Wagner, C., *Theorie der Alterung von Niederschlägen durch Umlösen (Ostwald-Reifung).* Zeitschrift für Elektrochemie, Berichte der Bunsengesellschaft für physikalische Chemie, 1961. **65**(7-8): p. 581-591.

112. Lifshitz, I.M. and Slyozov, V.V., *The kinetics of precipitation from supersaturated solid solutions.* Journal of Physics and Chemistry of Solids, 1961. **19**(1): p. 35-50.

113. Ardell, A.J., *Trans-interface-diffusion-controlled coarsening of γ′ particles in Ni–Al alloys: commentaries and analyses of recent data.* Journal of Materials Science, 2020. **55**(29): p. 14588-14610.

114. Ardell, A.J., *Precipitation hardening.* Metallurgical Transactions A, 1985. **16**(12): p. 2131-2165.

115. Heat Treatment. 2012, IntechOpen: Rijeka.

116. Stefanescu, D.M., *Science and engineering of casting solidification*. 2015: Springer.

117. Nembach, E., *Precipitation hardening caused by a difference in shear modulus between particle and matrix.* Physica status solidi (a), 1983. **78**(2): p. 571-581.

118. Brown, L. and Ham, R., *Strengthening methods in crystals.* Applied Science, London, 1971. **9**.

119. Hirsch, P. and Humphreys, F., *Physics of strength and plasticity.* MIT Press, Cambridge, 1969.

120. Zhu, A.W., Csontos, A., and Starke, E.A., *Computer experiment on superposition of strengthening effects of different particles.* Acta Materialia, 1999. **47**(6): p. 1713-1721.

121. Cinkilic, E., Yan, X., and Luo, A.A., *Modeling Precipitation Hardening and Yield Strength in Cast Al-Si-Mg-Mn Alloys.* Metals, 2020. **10**(10): 1356.

122. Wang, Z., Qu, R.T., Scudino, S., Sun, B.A., Prashanth, K.G., Louzguine-Luzgin, D.V., Chen, M.W., Zhang, Z.F., and Eckert, J., *Hybrid nanostructured aluminum alloy with super-high strength.* NPG Asia Materials, 2015. **7**(12): e229.

123. Zhao, Y., Zhang, W., Yang, C., Zhang, D., and Wang, Z., *Effect of Si on Fe-rich intermetallic formation and mechanical properties of heat-treated Al–Cu–Mn–Fe alloys.* Journal of Materials Research, 2018. **33**(8): p. 898-911.

124. Christian, J.W., *CHAPTER 10 - The Classical Theory of Nucleation*, in *The Theory of Transformations in Metals and Alloys*, J.W. Christian, Editor. 2002, Pergamon: Oxford. p. 422-479.

125. Silcox, J., *Dislocation loops in quenched aluminium and gold*, in *Verhandlungen: Physikalisch-Technischer Teil*, W. Bargmann, et al., Editors. 1960, Springer Berlin Heidelberg: Berlin, Heidelberg. p. 548-552.

126. Stroev, A.Y., Gorbatov, O.I., Gornostyrev, Y.N., and Korzhavyi, P.A., *Solid solution decomposition and Guinier-Preston zone formation in Al-Cu alloys: A kinetic theory with anisotropic interactions.* Physical Review Materials, 2018. **2**(3): p. 033603.

127. Merle, P. and Merlin, J., *Coarsening of θ′ plates in Al-Cu alloys—II. influence of ledge mechanism.* Acta Metallurgica, 1981. **29**(12): p. 1929-1938.

128. Liu, K., Cao, X., and Chen, X.G., *Solidification of Iron-Rich Intermetallic Phases in Al-4.5Cu-0.3Fe Cast Alloy.* Metallurgical and Materials Transactions A, 2011. **42**(7): p. 2004-2016.

129. Li, Z., Zhang, Z., and Chen, X.G., *Effect of Metastable Mg2Si and Dislocations on α-Al(MnFe)Si Dispersoid Formation in Al-Mn-Mg 3xxx Alloys.* Metallurgical and Materials Transactions A, 2018. **49**(11): p. 5799-5814.

130. Bahl, S., Xiong, L., Allard, L.F., Michi, R.A., Poplawsky, J.D., Chuang, A.C., Singh, D., Watkins, T.R., Shin, D., Haynes, J.A., and Shyam, A., *Aging behavior and strengthening mechanisms of coarsening resistant metastable θ′ precipitates in an Al–Cu alloy.* Materials & Design, 2021. **198**: 109378

131. Gao, Y.H., Cao, L.F., Kuang, J., Zhang, J.Y., Liu, G., and Sun, J., *Assembling dual precipitates to improve high-temperature resistance of multi-microalloyed Al–Cu alloys.* Journal of Alloys and Compounds, 2020. **822**: 153629.

132. Philippe, T. and Voorhees, P.W., *Ostwald ripening in multicomponent alloys.* Acta Materialia, 2013. **61**(11): p. 4237-4244.

133. Chen, Y.H. and Doherty, R.D., *On the growth kinetics of plate-shaped precipitates in aluminium-copper and aluminium-gold alloys.* Scripta Metallurgica, 1977. **11**(9): p. 725-729.

134. Sankaran, R. and Laird, C., *Further comments on the kinetics of growth of plate precipitates in Al - Ag, Al - Au and Al - Cu alloys.* Scripta Metallurgica, 1978. **12**(10): p. 877-883.

135. Chen, Y., Gao, N., Sha, G., Ringer, S.P., and Starink, M.J., *Microstructural evolution, strengthening and thermal stability of an ultrafine-grained Al–Cu–Mg alloy.* Acta Materialia, 2016. **109**: p. 202-212.

136. Medrano, S., *Study of concurrent recovery and precipitation on the mechanical behaviour of Al-Mg alloys with small additions of Cu*. 2018.

137. Jiang, S. and Wang, R., *Grain size-dependent Mg/Si ratio effect on the microstructure and mechanical/electrical properties of Al-Mg-Si-Sc alloys.* Journal of Materials Science & Technology, 2019. **35**(7): p. 1354-1363.

138. Kelly, A. and Nicholson, R., *Strengthening methods in crystals*. 1971, Amsterdam; New York: Elsevier Pub. Co.

139. Kumar Makineni, S., Sugathan, S., Meher, S., Banerjee, R., Bhattacharya, S., Kumar, S., and Chattopadhyay, K., *Enhancing elevated temperature strength of copper containing aluminium alloys by forming L1(2) Al(3)Zr precipitates and nucleating θ" precipitates on them.* Scientific reports, 2017. **7**(1): 11154.

140. Sankaran, K.K. and Mishra, R.S., *Chapter 4 - Aluminum Alloys*, in *Metallurgy and Design of Alloys with Hierarchical Microstructures*, K.K. Sankaran and R.S. Mishra, Editors. 2017, Elsevier. p. 57-176.

141. Kreyca, J., Falahati, A., and Kozeschnik, E., *Microstructure and Flow Stress Modelling During Plastic Deformation of an Aluminum Alloy Type A6061.* Materials Today: Proceedings, 2015. **2**: p. S107-S112.

142. Yuan, S.P., Liu, G., Wang, R.H., Pu, X., Zhang, G.J., Sun, J., and Chen, K.H., *Coupling effect of multiple precipitates on the ductile fracture of aged Al–Mg–Si alloys.* Scripta Materialia, 2007. **57**(9): p. 865-868.

143. Li, R., Ren, Z., Wu, Y., He, Z., Liaw, P.K., Ren, J., and Zhang, Y., *Mechanical behaviors and precipitation transformation of the lightweight high-Zn-content Al–Zn–Li–Mg–Cu alloy.* Materials Science and Engineering: A, 2021. **802**: 140637.

144. Dowling, N.E., *Mechanical behavior of materials : engineering methods for deformation, fracture, and fatigue*. 1993: Englewood Cliffs, N.J. : Prentice Hall, [1993] ©1993.